Metal Isotope Fractionation Associated with Cu and Zn Attenuation by Zero-Valent Iron in Anaerobic Flow-Through Cell Experiments

by

Jeffrey Leon

A thesis
presented to the University of Waterloo
in fulfillment of the
thesis requirement for the degree of
Master of Science
in
Earth Sciences

Waterloo, Ontario, Canada, 2018

Author's Declaration

I hereby declare that I am the sole author of this thesis. This is a true copy of the thesis, including any required final revisions, as accepted by my examiners.

I understand that my thesis may be made electronically available to the public.

Abstract

Metal stable isotope fractionation is an emerging tool in the environmental sciences for studying biogeochemical pathways for cycling of metals in the environment. Copper and zinc are essential elements for many biological functions, but can accumulate in high concentrations toxic to living organisms through anthropogenic activities such as mining. Permeable reactive barrier (PRB) technologies have been implemented at many field sites to remove inorganic contaminants, such as Cu and Zn, from groundwater. A common reactive material used to construct PRBs is zero-valent iron (ZVI), which is useful for its propensity to create strongly reducing conditions that favour the reduction and co-precipitation of metals. Flow-through cells (FTCs) were used to examine the isotope composition of Cu and Zn while these metals were removed from solution by ZVI. Attenuation of dissolved Cu resulted in the enrichment of the heavy isotope (^{65}Cu) in solution, where δ^{65}Cu initially peaked at 1.30 ‰ and decreased towards the mean influent isotope value ($\delta^{65}Cu_{input}$ = 0.27 ‰). Copper isotope ratios in the FTC effluent displayed Rayleigh-type behavior (ε = -0.31 ‰). X-ray absorption near edge structure (XANES) spectroscopy was used to identify the solid phases present in the FTCs. In linear combination fitting (LCF), reduced Cu and ZnO were found to primarily contribute to the solid species in respective Cu and Zn FTCs. Reduced Cu^0 consistently contributed to the fit for Cu XANES sample spectra present at the central position of the Cu FTC. Similar portions of Cu^0 and Cu_2O were identified at bottom and top positions of the Cu FTC, indicating that Cu isotope fractionation could be attributed to reduction of Cu during immobilization by ZVI. As Zn breakthrough in the FTC effluent occurred, an increase in δ^{66}Zn values was observed, increasing initially from -0.59 ‰ towards the mean $\delta^{66}Zn_{input}$ value of -0.19 ‰ throughout the experiment. The fractionation values (ε) for the Zn FTC II was 0.32 ‰. Linear combination fitting indicated

contributions from ZnO and $Zn(OH)_2$ in the fitting of four Zn sample spectra. A standard for Zn adsorbed to ferrihydrite also contributed to the fit for the Zn XANES spectra from the bottom location of the FTC. These XAS measurements suggest a combination of adsorption and precipitation mechanisms contributed to the majority of the depletion of the heavy Zn isotope associated with Zn attenuation by ZVI. Characterizing the isotope fractionation linked to Cu and Zn removal by ZVI in PRB systems may contribute to an enhanced knowledge of how isotopes can be correlated to geochemical processes. This insight may be influential for understanding the controls on metal mobility at contaminated sites, and how to devise more efficient and economical groundwater monitoring programs.

Acknowledgements

Thank you to David Blowes and Carol Ptacek for accepting me into the GGR group, for your advice and revisions, for offering me external opportunities, for your patience throughout this whole process, and for sending me off into the world with a little more knowledge about the potential of geochemistry.

Funding for this research was provided by the Natural Sciences and Engineering Research Council of Canada (NSERC) Strategic Project Grant, NSERC Discovery Grant, and Ontario Research Fund (ORF), awarded to Dr. Blowes and Dr. Ptacek. Synchrotron-based techniques in this thesis were performed at Sector 20 PNC/XSD (CLS@APS) at the Advanced Photon Source (APS) operated at Argonne National Lab (Lemont IL), which is supported by the U.S. Department of Energy and the Canadian Light Source (CLS; supported by the Canada Foundation for Innovation, NSERC, the University of Saskatchewan, the Government of Saskatchewan, Western Economic Diversification Canada, the National Research Council Canada, and the Canadian Institutes of Health Research). I offer my sincerest thanks to Zou Finfrock, Mali Balasubramanian, Dale Brewe, and Mike Pape for their welcoming attitudes, expertise, and assistance with XAS data collection at Sector 20, APS.

I deeply appreciate the extensive work provided by Laura Groza and Joy Hu in the analytical aspects of the research, including timely analysis of cation and anion aqueous concentrations. An honourable mention must be extended to Julia Jamieson-Hanes for prepping me on most things I have learned related to flow-through cells and isotopes, two of the more important components to my thesis. I am very grateful for your constant advice and dedication to the mission of this thesis. Thank you to Lingyi Kong and Jane Eagling for your devotion to isotope methods in the clean lab which enabled a very significant component of this research.

Thank you to Emily Saurette for her continued encouragement and valuable assistance in the editing process. Thank you to Jeff Bain for your assistance and know-how in all aspects related to lab management and equipment. For his time, expertise, and input as this MSc project developed, I also thank Dogan Paktunc.

Many thanks to all grad students and post docs of the Groundwater Geochemistry and Remediation group for their support, optimism, and company over the past few years. I send my regards to past housemates, graduate students throughout the department, and intramural teammates who shared their time, smiles, stories, and enriched my experience at Waterloo.

Thank you to the Earth Sciences graduate coordinator, Sue Fisher, for always being on top of things, finding answers to issues, and moving things along as efficiently as possible whenever I needed assistance.

A tremendous thanks to all my immediate and extended family and friends I've been blessed with for their continued encouragement, immense support and belief that I may one day finish this program.

To all those in my community and abroad who fight for their own purpose and use their talents to light up the world; you provide more inspiration than you know. For those involved in future research in Canada and around the globe that actively see the results of this thesis advance to field applications to remediate contaminated groundwater, I acknowledge you for fulfilling the greater purpose of this work.

The combined efforts of all of these people are the reason this MSc has come to fruition, in spite of my ongoing mental barriers and wavering motivation. Should you happen to read this, please pat yourself on the back.

Dedication

This MSc thesis is dedicated to my parents for their endless love and support.

Table of Contents

List of Tables

List of Figures

List of Abbreviations

AMD	acid mine drainage
ANL	Argonne National Laboratory
APS	Advanced Photon Source
BM	bending magnet (beamline classification)
ERM	European Reference Materials
EPA	Environmental Protection Agency
HDPE	high-density polyethylene
HEPA	High-Efficiency Particulate Air
ICP-OES	inductively coupled plasma-optical emission spectrometer
ID	insertion device (beamline classification)
IRMM	Institute for Reference Materials and Measurements
FTC	flow-through cell
MC-ICP-MS	multicollector-inductively coupled plasma-mass spectrometer
PRB	permeable reactive barrier
PV	pore volume
XANES	x-ray absorption near-edge structure
XAS	x-ray absorption spectroscopy
ZVI	zero-valent iron

Chapter 1: Introduction

1.1 Background

1.1.1 Copper and Zinc in Groundwater

Copper (Cu) and zinc (Zn) are chalcophilic transition metal elements, abundant in the environment within sulfide phases. These metals are mined worldwide for their use in industrial and agricultural applications (Acosta et al., 2011). Copper is a micronutrient critical to the production of hemoglobin in humans, but can cause anemia, liver and kidney damage, and irritation to the stomach and intestines if ingested in excess levels (Wuana and Okieimen, 2011). Unlike many other toxic and heavy metals, Cu does not biomagnify through the food chain up to humans. Plant growth also depends on Cu uptake for seed production, disease resistance, and water regulation (Wuana and Okieimen, 2011). Zinc is necessary for the health of humans and organisms as a trace element utilized by regulatory proteins in an array of enzymatic functions (Cloquet, Carignan, Lehmann, and Vanhaecke, 2008). In elevated concentrations, Zn can become toxic and may accumulate in the bodies of various fish, allowing it to biomagnify (Wuana and Okieimen, 2011).

Human health is directly impacted by these metals through ingestion of contaminated soil, surface water or groundwater. Copper and Zn are grouped with Pb, Cr, As, Cd, Hg and Ni in a class of heavy metal inorganic chemical hazards. These metals all have the potential to persist in the environment long after release, as they cannot be degraded microbially or chemically, unlike organic contaminants (Wuana and Okieimen, 2011). Copper and Zn have both been named to the US EPA Toxic Pollutants and Priority Pollutants Lists in accordance with the Clean Water Act (EPA, 2014; 2015).

Copper is commonly released to groundwater sources through corrosion and leaching of copper pipes. Various consumer goods and fertilizers indirectly augment natural Cu and Zn cycling in the environment (Acosta et al., 2011). Extraction, processing, and refining of Cu and Zn ores in mining ultimately are the primary source of Cu and Zn release to the environment (Acosta et al., 2011). Large tracts of land are excavated to access Cu and Zn ore bodies in open-pit and underground mining operations. During mineral extraction, higher grade ore is separated from host rock and lower-grade ore for mineral separation. These different ore streams vary in overall composition, producing waste rock and mine tailings disposal areas with varying geochemical characteristics (Blowes et al., 2013). Acid mine drainage (AMD) accumulated from the storage and leaching of mine wastes may cause adverse impacts to the environment from mining. The oxidation of pyrite (FeS_2) and other Fe sulfide minerals in mine waste triggers acid-generating conditions, releasing aqueous Fe and sulfate. The influence of O_2, Fe, temperature, pH, redox potential (Eh), and the presence of microorganisms and neutralizing minerals all play a role in developing AMD conditions to create low quality surface and groundwater.

1.1.2 Permeable Reactive Barriers for Groundwater Remediation

To counteract the negative impacts of dissolved metals on water supplies and surrounding ecosystems, effective remediation technologies are required. Widely implemented physico-chemical approaches for restoring natural groundwater conditions includes the permeable reactive barrier (PRB) passive *in situ* remediation technology (Blowes et al., 2000; Blowes et al. 1997). A number of chemical and biological technologies also exist, such as injection of reductants, chemical flushing, anoxic limestone drains, tailings impoundment covers, *in situ* biological amendment, constructed wetlands, and enhanced biorestoration (Hashim et al., 2011). Biostimulation may also be incorporated into PRB design if the reactive material in the PRB

provides a source of organic carbon to assist in microbial reduction of sulfate (Benner et al., 1997; Lindsay et al., 2008; Waybrant et al., 2002). These groundwater technologies are preferable to traditional pump-and-treat methods which are unsustainable due to cost and intensive use of resources (Blowes et al., 1997; Mackay and Cherry, 1989; Starr and Cherry, 1994). Permeable reactive barriers have been implemented at hundreds of field sites and provide an effective approach to passively treating a variety of contaminants, ranging from heavy metals to chlorinated hydrocarbon compounds (Benner et al., 1997; Blowes et al., 2000; Ritter et al., 2002) .

Zero-valent iron is an effective PRB material for the reduction of multivalent metals (Blowes et al., 1997; Jamieson-Hanes et al., 2014) coupled with adsorption and precipitation of inorganic contaminants (Blowes et al., 2000; Cantrell et al., 1995; Herbert, 2003; Puls et al., 1999). Groundwater is quickly depleted of O_2 upon entering a ZVI barrier, potentially leading to the following reactions *in situ* if anaerobic conditions are maintained (Furukawa et al., 2002; Herbert, 2003; Odziemkowski et al., 1998).

$$Fe^0 + 2H_2O \rightarrow Fe^{2+} + H_2 + 2\ OH^- \quad (1.1)$$

$$2\ Fe(OH)_{2(s)} \rightarrow Fe_3O_{4(s)} + H_{2(g)} + 2H_2O \quad (1.2)$$

The formation of Fe (oxy)hydroxides on surface coatings of ZVI is typical within a PRB, and these surface products tend to raise the pH of aqueous solutions (Eq. 1.1), while providing a layer conducive to adsorption and precipitation reactions for metals in solution (Blowes et al., 2000; Morrison et al.,2002). This outer layer of Fe (oxy)hydroxides may range from ferrihydrite, goethite, green rust, maghemite, and lepidocrocite if groundwater is oxygenated, in contrast to ferrous hydroxide and magnetite which can have greater potential to form in anoxic systems

(Blowes et al., 1997; Furukawa et al., 2002; Jeen et al.2007; Morrison et al., 2002; Odziemkowski et al., 1998).

1.1.3 Copper and Zinc Isotope Fractionation

The advancement of multicollector inductively coupled mass spectrometry (MC-ICP-MS) has led to breakthroughs in isotope research over the past two decades. The application of metal stable isotopes in the Earth Sciences has been used to identify degrees of fractionation associated with metal mineralization in the environment, and differentiating natural sources from anthropogenic metal inputs (Bigalke et al., 2010; Bullen and Walczyk, 2009; Ellis, 2002; Kimball et al., 2009; Maréchal et al., 1999).

Copper has two stable isotopes, ^{65}Cu and ^{63}Cu, in abundances of 30.9% and 69.1% respectively (Hoefs, 2009). Copper isotope ratios are reported as δ^{65}Cu values, or the ratio between the heavy and light isotopes relative to an accepted international isotope standard. Equation 1.3 illustrates the calculation of Cu isotope ratios relative to the European reference material (ERM) for Cu isotopes, ERM-AE633. Copper isotope fractionation throughout the natural environment has been found to vary between -3 ‰ to 6 ‰ (Weiss et al., 2008).

$$\delta^{65}Cu = \left[\frac{\left({}^{65}Cu / {}^{63}Cu \right)_{sample}}{\left({}^{65}Cu / {}^{63}Cu \right)_{ERM-AE633}} - 1 \right] \times 1000 \qquad (1.3)$$

Five isotopes of Zn exist in nature: ^{64}Zn (49.2%), ^{66}Zn (27.7%), ^{67}Zn (4.0%), ^{68}Zn (18.4), and ^{70}Zn (0.6%) (Meija et al., 2016). Zinc isotope ratios are normally reported as $\delta^{66/64}$Zn, calculated in reference to the Institute for Reference Materials and Measurements (IRMM) Zn isotope standard IRMM-3702. With this standard as a reference, Zn isotope measurements reported in the literature for environmental samples range from approximately -1.5 ‰ to 1 ‰ (Weiss et al., 2008).

$$\delta^{66}Zn = \left[\frac{\left(\delta^{66}Zn/\delta^{64}Zn\right)_{sample}}{\left(\delta^{66}Zn/\delta^{64}Zn\right)_{IRMM-3702}} - 1 \right] \times 1000‰ \quad (1.4)$$

To evaluate Cu and Zn isotope fractionation, a separation factor is frequently used to delineate the difference between δ values measured in the aqueous and solid phases, i.e. $\Delta^{65}Cu_{soln\text{-}solid}$ (Balistrieri et al. 2008; Bigalke et al., 2010; Juillot et al., 2008; Kimball et al., 2009; Little et al. 2014; Pokrovsky et al., 2005; Wanty et al., 2013). For isotope ratios measured within the same reservoir, isotope models may be fit to a set of δ values to determine fractionation factors (α and ε) specific to a system. Two models widely used in environmental isotope studies include the Rayleigh distillation model and closed-equilibrium exchange model (Balistrieri et al., 2008; Jamieson-Hanes et al., 2012; Johnson et al., 2004; Pokrovsky et al., 2008; Veeramani et al., 2015; Weiss et al., 2013). While closed-equilibrium exchange isotope data follows a linear trendline (Balistrieri et al., 2008; Juillot et al., 2008), Rayleigh-type fractionation follows an exponential curve modelled by equation 1.5:

$$\frac{R}{R_0} = f^{(\alpha-1)} \quad (1.5)$$

where R is a sample-specific isotope ratio, R_0 pertains to the isotope ratio of the input, f is the fraction of metal in solution and α is the fractionation factor. The epsilon notation (ε) of the fractionation factor is related to α by equation (1.6), and is used to improve clarity when discussing isotope fractionation.

$$\varepsilon = (\alpha - 1) \times 1000 \text{ ‰} \quad (1.6)$$

The Rayleigh distillation model requires an ideally closed system in which reactants are isolated from the products, such that isotope exchange is irreversible following fractionation. It is also

necessary that isotopes in various reservoirs are perfectly mixed, to ensure representative isotopic composition upon sampling (Johnson et al., 2004; Weiss et al., 2008).

1.2 Objectives of Thesis: Characterizing Cu and Zn Attenuation

Removal of Cu from contaminated groundwater normally involves reduction and co-precipitation within oxides or sulfides, precipitation, or adsorption to ZVI surfaces (Balistrieri et al., 2008; Blowes et al., 2000; Ku and Chen, 1992; Pokrovsky et al., 2005). Zinc persists in the environment in its divalent form, and reduction is not thermodynamically favourable (Li and Zhang, 2007). Consequently, Zn is normally removed through a combination of precipitation and adsorption mechanisms (Herbert, 2003; Juillot et al., 2008; Rangsivek and Jekel, 2005). Specific removal pathways are highly dependent on the aqueous geochemistry of a site or laboratory experiment, including pH, Eh, the presence of O_2 and other chemical constituents in solution,

and the presence of microorganisms. Isotope fractionation in combination with measurements of traditional bulk geochemistry can improve monitoring of contaminant transport and behavior in the environment (Blowes, 2002; Ellis et al., 2002; Weiss et al., 2008).

The primary goal of this MSc research is to investigate how metal stable isotope ratios can be correlated to dissolved metal concentrations to characterize metal attenuation processes. This research may prove useful in evaluating the effectiveness of groundwater remediation approaches in the field going forward, specifically where ZVI is used in PRB systems. It has been demonstrated that isotope fractionation of metals in the environment is influenced substantially by redox reactions and biologically mediated reactions (Cloquet et al., 2008; Ehrlich et al., 2004; Jamieson-Hanes et al., 2017; Zhu et al., 2002). The contribution of isotope exchange induced during precipitation and adsorption should be accounted for, particularly in ZVI systems (Balistrieri et al., 2008; Borrok et al., 2009; Jamieson-Hanes et al., 2012).

Understanding the isotope fractionation associated with a variety of biogeochemical reactions, whether the degree of fractionation be large or small, is essential for pinpointing the cause of isotope variations in field samples. The chemical coordination and complexation of metals is subject to change as the contaminant partitions between phases, as expected during removal from groundwater. Characterizing the solid phase products formed in a remediation-based experiment is therefore valuable for interpreting what may lead to isotope fractionation.

To address the main objectives of this study, an anaerobic FTC experiment was operated in a glovebox to investigate the changes in effluent concentrations of Cu and Zn as these metals react with ZVI. Breakthrough curves were measured, along with Cu and Zn isotope ratios. X-ray adsorption near-edge structure (XANES) analyses were conducted on the solid phase FTC material after termination of each experiment to assess the *in situ* state of attenuated metals. Isotope data was fit with Rayleigh curves and interpreted in conjunction with aqueous geochemistry from the saturated flow experiments and XANES spectra to evaluate whether isotope fractionation may be a useful indicator of metal attenuation mechanisms (represented by Figure 1.1).

1.3 Organization of Thesis

The chapters of this thesis are structured as an introduction, two research articles, followed by a brief conclusion where overall findings are highlighted. Chapter 1 introduces Cu and Zn as groundwater contaminants, groundwater remediation techniques of importance to this study, and the goals of this thesis, including experimental procedures. Chapters 2 and 3 are specific to Cu and Zn experiments respectively. The results of anaerobic FTC experiments are presented and discussed in Chapters 2 and 3, and include bulk geochemistry of FTC effluent, XAS data for solid phase characterization, and isotope measurements of Cu and Zn measured.

Chapter 4 outlines key findings from the overall set of experiments, and provides recommendations for future metal isotope studies.

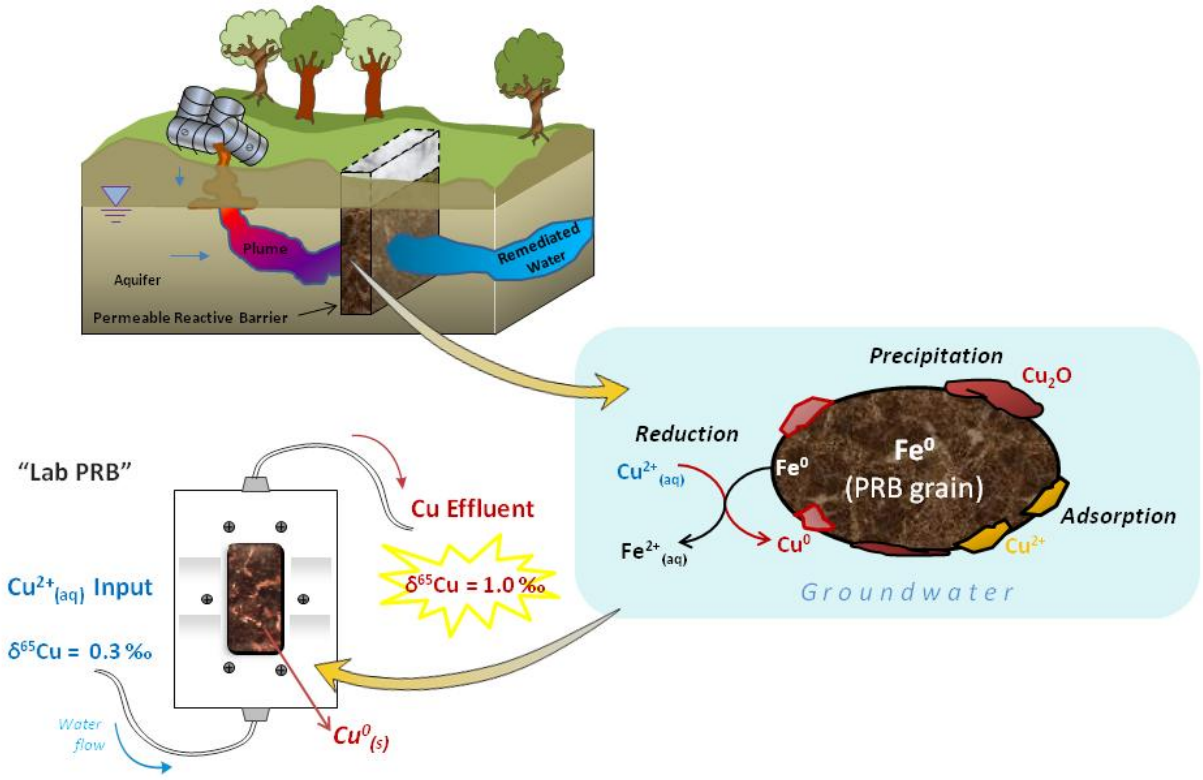

Figure 1.1 The scale and importance of this thesis project illustrated through implementation of a permeable reactive barrier in the field, reactions typically involved with metal attenuation by ZVI, and the expected isotope fractionation associated with these reactions in a Cu flow-through cell.

Chapter 2: Isotope fractionation and attenuation of Cu in a zero-valent iron flow-through cell experiment

2.1 Summary

Fractionation of metal stable isotopes has emerged in recent years as a potential geochemical tool for monitoring the mechanisms controlling the transport and attenuation of harmful metals in the environment. Zero-valent iron (ZVI) has been increasingly implemented over the past two decades in groundwater remediation applications as a permeable reactive barrier (PRB) material due to its usefulness in attenuating inorganic contaminants. In this study, Cu isotope fractionation was assessed to determine the utility of stable Cu isotope ratio measurements in characterizing Cu partitioning between the aqueous and solid phases in ZVI remediation systems. Laboratory anaerobic flow-through cell (FTC) I and FTC II experiments of similar design were carried out to measure aqueous geochemical parameters during Cu breakthrough in ZVI saturated flow systems. The effluent Cu concentration reached a maximum of 9.43 mg L^{-1} in FTC II, greater than in FTC I (6.52 mg L^{-1}), which allowed for enhanced $\delta^{65}Cu$ characterization. Increasing concentrations of Cu in the FTC effluent samples were accompanied by a gradual decrease in $\delta^{65}Cu$. A maximum $\delta^{65}Cu$ of 1.03 ± 0.07 ‰, was measured relative to the input solutions early in the FTC II experiment. Application of the Rayleigh distillation model generated an isotope fractionation value (ε) of -0.31 ‰, denoting a low to medium degree of within-fluid fractionation relative to that typically observed for Cu removal processes and other transition metal isotope fractionation values related to reduction. At the termination of the experiment, accumulations of $Cu^{0}_{(s)}$ were observed visually. X-ray absorption near edge spectroscopy (XANES) was conducted on bulk samples from the anaerobic FTCs to investigate Cu removal by ZVI. Linear combination fitting analysis of bulk ZVI indicated the predominant

presence of $Cu^0_{(s)}$, but also cuprite ($Cu_2O_{(s)}$). These results suggest that reduction of Cu^{2+} imparts a moderate degree of fractionation, enriching the aqueous phase in ^{65}Cu. Implementation of Cu isotope analysis into groundwater monitoring may potentially be a valuable indicator of Cu removal mechanisms in PRB systems.

2.2 Introduction

Groundwater contamination by dissolved metals is a high priority environmental issue because of the direct threat posed to human health through water supplies reliant on groundwater and the broader environmental concern when released to surface water bodies. Metal mines are a major source of Cu to the environment, causing soil and water contamination, destruction of habitat, and degradation of natural resources (Acosta et al., 2011; Forghani et al., 2015). Copper mining frequently requires excavation of up to 100 tonnes of ore per tonne of Cu yielded, generating immense quantities of Cu-bearing waste rock (Blowes et al., 2013). These wastes may oxidize, creating low pH surface water rich in dissolved iron, sulfates, Cu and other toxic metals (Wilkin and McNeil, 2003). Copper is also released to the environment through metallurgical processing waste streams, agricultural, industrial, and consumer applications (Blowes et al., 2013; Sigg, 2014). The agricultural industry utilizes Cu as a feed additive and Cu-salts are commonly used in biologic farming as a fungicide (Aldrich et al., 2002). Copper is used broadly for manufacturing circuitry, musical instruments, vehicle components, and construction tubing; disposal or corrosion of these materials can lead to elevated Cu levels in municipal wastewater (NRCAN, 2015). This transition metal is a nutrient element with many essential enzymatic functions, but release through anthropogenic sources to surface water, the atmosphere, and soils may eventually increase Cu concentrations in groundwater to harmful concentrations (Sigg, 2014).

Copper is most commonly in one of two oxidation states, Cu^{1+} or Cu^{2+}, and is rarely found in nature in its elemental form. The divalent state of this metal is more soluble, therefore persists as a mobile contaminant in groundwater. Under the Goldschmidt classification, Cu is a chalcophile, hosted ubiquitously in sulfide minerals throughout the environment and is naturally incorporated in oxides and carbonates under oxidizing conditions (Hoefs, 2009). Copper occurs as two isotopes, ^{63}Cu and ^{65}Cu, which respectively have average abundances of 69.1% and 30.9% in the environment (Hoefs, 2009). The occurrence of Cu in square planar, square pyramidal, trigonal bypyramidal and tetragonal chemical coordinations in solid and aqueous complexes has been recognized as a contributor to a wide range of isotope compositions (Pokrovsky et al., 2008). Understanding the Cu coordination environment, including bond strength with neighbouring elements, is an asset for interpreting isotope behaviour because reaction products are preferentially enriched in lighter isotopes (Schauble, 2004; Weiss et al., 2008).

A variety of active and passive methods are available for the treatment of Cu in groundwater. Permeable reactive barriers (PRBs) are a passive remediation approach for removing a range of contaminants from groundwater (Blowes and Ptacek, 1994; Gillham, 1996), including toxic metals near contaminated sites (Blowes et al., 2013). This technology involves installing zones of reactive material in the subsurface to intercept the migrating path of groundwater plumes and remove harmful chemical constituents from the aqueous phase. Geochemical attenuation processes such as precipitation, sorption and reduction are promoted using a variety of reactive materials. Zero-valent iron promotes reduction reactions and has been demonstrated to be an effective barrier material for the treatment of dissolved metals and other toxic substances (Blowes and Ptacek, 1994; Blowes et al., 1997; Cantrell et al., 1995; Puls et al.,

1999; Shokes and Möller, 1999). Reduction of Cu is implemented in hydrometallurgy for extraction of metallic Cu from parent minerals (Atwood, 1974; Ku and Chen, 1992). The redox sensitive nature of Cu allows ZVI to be utilized to promote Cu removal through the cementation reaction at field sites where elevated Cu concentrations persist in groundwater.

Following reduction of a contaminant, a wide variety of Fe (oxy)hydroxide oxidation products of ZVI may be produced that can facilitate adsorption, precipitation, or co-precipitation, making ZVI extremely versatile for *in situ* remediation (Johnson et al., 2000; Noubactep, 2007). Magnetite is a recurring product of formation resulting from amorphous $Fe(OH)_2$ in several studies which determined byproducts of anaerobic ZVI corrosion (Farrell et al., 2001; Furukawa et al., 2002; Morrison et al., 2002; Odziemkowski et al., 1998; Rangsivek, 2010). The formation of a ferrous hydroxide-magnetite outer core around ZVI grains enables electron transfer from the inner ZVI grain through surface films, permitting Cu reduction at the surface as the granular iron corrodes (Odziemkowski et al., 1998). A number of other iron oxide species have been detected in simulated groundwater systems where ZVI corrodes under anaerobic conditions, including maghemite and lepidocrocite. These two minerals are commonly derived from the oxidation of green rust. Green rusts form in groundwater with low redox potential rich in carbonate, chloride and sulfate (Jeen et al., 2007; Odziemkowski et al., 1998; Rangsivek, 2010; Wilkin and McNeil, 2003), and are not expected products in O_2 deficient, anaerobic systems.

Removal of Cu from aqueous solution by ZVI and its reaction products has been evaluated through a number of laboratory studies (Balistrieri et al., 2008; Komnitsas et al., 2007; Ku and Chen, 1992; Li and Zhang, 2007; Ludwig et al., 2002; Rangsivek and Jekel, 2005; Shokes and Möller, 1999; Statham et al., Mumford, Rayner, and Stevens, 2015; Wilkin and McNeil, 2003). Zero-valent iron has also been implemented successfully in field applications

(Powell et al., 1998; Puls et al., 1999). The dominant pathway for removal of Cu and other electroactive metals involves reduction by ZVI followed by coprecipitation within secondary precipitates (Blowes et al., 2000; Powell et al., 1998).

Non-traditional isotope analysis is gaining traction as a tool for monitoring metal treatment at contaminated field sites. Heavy metal fractionation may assist in distinguishing attenuation mechanism with unique changes in isotopic ratios. Isotope ratio measurements have the potential to provide information about reactions promoting Cu^{2+} removal from aqueous solution, offering insight on processes occurring at larger spatial scales, complementing conventional geochemical data offered by soil samples or discrete metal concentrations (Blowes, 2002). Isotope fractionation can also be used to identify the sources (*e.g*. natural deposits or industrial sites) from which the heavy metals originated (Bigalke et al., 2010). The reduction of Cu by ZVI in a PRB may also be inferred from metal isotope data, allowing for better informed decisions to maximize long-term efficiency of ZVI barriers.

Many Cu isotope studies place an emphasis on solution-solid fractionation, accounting for isotopic variations between aqueous Cu^{2+} and adsorbed or reduced Cu in the solid phase. The majority of Cu isotope fractionation reported in the literature pertains to natural geologic processes, such as the formation of primary and secondary Cu sulfides. Copper isotope values ($\delta^{65}Cu$) vary from approximately -3 to 6 ‰ in the natural environment, accounting for isotope measurements in sediments, biological material, and secondary ore minerals (Weiss et al., 2008). Elemental Cu is restricted to a $\delta^{65}Cu$ range of -0.5 to 0.4 ‰ (relative to NIST SRM 976) in the natural environment, where primary Cu^{1+} minerals are characterized by Cu isotope ratios of 0.6 ‰ or less (Markl et al., 2006).

Redox reactions have been identified as an important control on metal isotope fractionation for elements with multiple valence states, including Cu, Cr, Hg, Ni, Se, Te, U and Zn (Albarède, 2004; Ehrlich et al., 2004; Ellis et al., 2002; Fujii et al., 2013; Jamieson-Hanes et al., 2014; Mathur et al., 2014; Schauble, 2004; Wiederhold, 2015; Zhu et al., 2002). A change in oxidation state amongst redox-sensitive metals is a well-known cause of Cu isotope fractionation (Markl et al., 2006; Mathur et al., 2005) and laboratory studies indicate that Cu^{2+} reduction to Cu^{1+} tends to induce greater fractionation for reduction to Cu^{1+} than Cu^{0} (Ehrlich et al., 2004; Larson et al., 2003; Zhu et al., 2002).

Measurements of Cu isotope ratios in PRBs at sites undergoing remediation have potential to provide an additional tool to identify specific processes removing Cu from groundwater. These processes may include reduction and cementation, (co)precipitation, adsorption, or a combination of these mechanisms, all capable of altering the isotopic composition of Cu *in situ* to varying degrees. In this study, a flow-through cell procedure was used to characterize Cu breakthrough and provide insight into Cu removal under saturated conditions in a remediation system. Traditional aqueous geochemistry measurements were supplemented by XANES solid phase characterization and compared to measurements of Cu isotopes to improve our understanding of Cu attenuation mechanisms by ZVI. Differences in $\delta^{65}Cu$ effluent composition relative to the influent can assist in determining the magnitude of fractionation induced by Cu removal reactions. Deciphering site-specific geochemical processes influencing heavy metal transport has implications for optimizing remediation strategies to ensure maximal protection of groundwater. By combining measurements of isotope ratios with Cu concentrations after Cu immobilization by ZVI, the results may provide a geochemical tool

for identifying various metal removal mechanisms in PRBs and gauging overall remediation efficiency.

2.3 Methods

2.3.1 Experimental Design and Setup

A flow-through cell (FTC) experiment was conducted using a 7 cm × 5.5 cm × 2.5 cm (height × width × depth) high-density polyethylene (HDPE) cell. The FTC was custom-made with a central cavity measuring 3 cm × 5.5 cm × 2.5 cm (internal total volume of 2.25 cm^3) in which solid-phase reactive media, consisting of ZVI and silica sand, was packed. One face of the FTC (4.5 cm^2) had an opening which was covered with Kapton® film to contain the reactive media and enable x-ray penetration with minimal interference, optimizing the FTC for solid-phase synchrotron radiation analysis. A rubber O-ring encircled the central cavity of the FTC to ensure the system was gas-tight and leak-proof. The FTC was constructed with 2 mm ports centered at its bottom and top to allow metal-bearing solutions in and out of the cell. Pieces of Nitex® 210 µm mesh screen (approximately 1.0 cm × 0.5 cm) were positioned on the inside end of the influent and effluent ports to prevent clogging by the reactive media.

All experimental work was conducted in an anaerobic glovebox with a 3.5% H_2-balance N_2 atmosphere (Coy Laboratories Inc., Grass Lake, MI). The ZVI (Connelly GPM Inc., Chicago IL) was washed three times with 1.2 M HCl followed by six rinses with ultrapure water. The silica sand (U.S. Silica, Ottawa, IL) was rinsed several times with ultrapure water prior to use. Coning and quartering manual mixing (Gerlach and Nocerino, 2003) was used to homogenize these solid phases into a 10% v/v ZVI-silica sand mixture. This mixture was left to air-dry in the glovebox, then used to pack the FTC cell slightly in excess. The solid material was then covered with the

Kapton® film (80 µm thick) that was secured tightly by an HDPE exterior covering with a window of dimensions equal to the exposed FTC face.

The ZVI-silica sand media within the FTC was saturated and conditioned with Ar-purged ultrapure water (Milli-Q©) for 40 days. An Ismatec™ peristaltic pump (Cole-Parmer, Montreal, QC) fitted with Pharmed tubing was used to induce water flow through the FTC at an initial average velocity of 11 mL hr^{-1}. The pore volume (PV) of the FTC was determined as the difference between the masses of the FTC when the material was saturated versus dry. Over the ~40 days of conditioning, approximately 13,500 PVs of ultrapure water were pumped through the FTC. A conditioning period was used to increase the reactivity of the ZVI by washing off pre-existing Fe coatings on the surface of the granular iron grains which can potentially passivate the surface (Gui et al., 2009). Rinsing the ZVI in this manner develops an auto-reducing state in the system by removing surface films which inhibit electron transfer and catalytic hydrogenation (Ritter et al., 2002).

Input solutions for the FTC experiments were prepared by dissolving reagent grade $Cu(SO)_4 \bullet 5H_2O$ (Sigma-Aldrich Corp, Oakville, ON) in ultrapure water. A 1000 mg L^{-1} Cu stock solution was diluted in ultrapure water to 10 mg L^{-1} in 4 L batch volumes purged with Ar gas to replenish the Cu FTC input when necessary.

Two FTC experiments, FTC I and FTC II, were performed and samples were analyzed for Cu concentrations and isotope ratios. Both FTC cells were packed with the same 10% v/v ZVI-silica sand mixture. Following a stepped flow rate approach, the pump speed was adjusted on an incremental basis during each test to expedite Cu breakthrough. The speed of the peristaltic pump was increased 10 to 20 mL hr^{-1} after it was determined that the Cu concentrations of effluent samples at a given flow rate changed minimally. FTC I was conducted to identify

optimal flow rates to induce Cu breakthrough. These optimized flow rates were used to improve characterization of Cu breakthrough in FTC II.

2.3.2 Aqueous Sampling

Microelectrodes (Microelectrodes Inc., Bedford, NH, USA) were attached at the effluent (top) port of the FTC to monitor pH and oxidation-reduction potential (ORP), used to calculate Eh relative to the Standard Hydrogen Electrode. These flow-through microelectrodes operate relative to an external Ag-AgCl reference electrode to collect real-time geochemical readings at a regular time interval. Every few days during the experiment, the microelectrodes were disconnected from the FTC setup for calibration. Standard pH 4, 7 and 10 buffers were used to confirm the stability of the pH electrode. The performance of the Eh microelectrode was evaluated by measuring the response to Zobell's (Nordstrom and Wilde, 1977) and Light's (Light, 1972) solutions. A band pass filter was implemented in Microsoft Excel on raw pH and Eh data to filter outliers exceeding 2σ. Microelectrode readings were then subjected to a boxcar smoothing technique where measurements were compartmentalized in groups of five and averaged.

To monitor breakthrough of Cu from the FTC at early time, effluent was collected in 120 mL HDPE bottles once daily. These samples were acidified with concentrated HNO_3 to a pH < 2, and aliquots were set aside for cation and isotope analyses. The volume of the bulk fraction stored in HDPE bottles varied between 50 to 100 mL to ensure a sufficient volume was gathered for Cu isotope analysis.

Acidified samples were analyzed for major and trace element concentrations using an inductively coupled plasma-optical emission spectrometer (ICP-OES; iCAP 6500; Thermo Scientific).

2.3.3 X-ray Absorption Spectroscopy Data Collection and Processing

FTC II samples were prepared for XANES measurements by dividing the ZVI-silica sand contents of the FTC into top, middle, and bottom subsections in an anaerobic chamber. The ZVI samples were subsequently frozen in liquid nitrogen and stored in a deep freezer (-18 ºC). The frozen samples were freeze-dried for 40 hours at -50 ºC using a 2.5 L benchtop freeze dry system (Cole-Parmer Inc.). The freeze-dried samples were placed into small wells (10 mm internal diameter, 2.5 mm depth) of a custom-made acrylic holder. Kapton® tape was used to confine the samples within the plastic plate. This bulk sample holder was transported to Sector 20-BM-B at the APS for extended XANES data collection.

The XAS measurements on FTC II solids were conducted at a bending magnet (BM) beamline at the Advanced Photon Source (APS), Argonne National Lab, IL. Copper XANES spectra were collected at Sector 20-BM-B on the bulk ZVI FTC samples. The XANES spectra for FTC II samples were collected in fluorescence mode. The high intensity BM-B beamline uses a Si(111) double-crystal monochromator to induce a flux on the order of 1×10^{11} photons/sec at 10 keV for a 1000µm × 50µm focused beam. The Cu K-edge is at 8979 eV and triplicate scans were collected over an approximate range of 8800 to 9300 eV for each bulk sample from FTC II.

XANES data for pertinent reference materials were collected in transmission mode at previous visits to the APS. All XANES data processing was conducted with Athena, a part of the widely used IFEFFIT package developed by Ravel and Newville (2005) for XAS data analysis. The Artemis component of this software was also used to model the Extended X-ray Absorption Fine Structure (EXAFS) spectra for Cu FTC II samples. Cu standards for copper oxides, hydroxide, and sulfides were selected for the interpretation of Cu sample spectra based on the

anticipated reaction products in the FTC treatment system. The Cu foil (Cu^0) was used to calibrate the beam for the Cu XANES measurements of FTC samples.

2.3.4 Cu Isotope Measurements

Aqueous samples from the FTC experiments were selected for measurement of Cu isotope ratios based on an even distribution over the concentration range, where *f*, the fraction of Cu remaining in solution, is the ratio of Cu (mg L^{-1}) in an effluent sample to Cu in the input solution. Sample purification and isotope measurements were performed by Jane Eagling, a post-doctoral fellow, and research assistant Julia Jamieson-Hanes, in the clean metal laboratory of the Groundwater Geochemistry and Remediation Group at the University of Waterloo. The isotope purification method, modified from Maréchal et al.(1999), was conducted to prepare for analysis of the ^{65}Cu to ^{63}Cu ratio present in solution relative to the international Cu isotope standard ERM-AE633, described by the formula:

$$\delta^{65}Cu = \left[\frac{\left({}^{65}Cu / {}^{63}Cu \right)_{sample}}{\left({}^{65}Cu / {}^{63}Cu \right)_{ERM-AE633}} - 1 \right] \times 1000 \qquad (2.1)$$

Sample preparation was conducted in a clean laboratory inside a laminar flow hood with circulating HEPA filtered air. BioRad® AG-MP-1 anion-exchange resin pre-washed with HCl and HNO_3 was used to separate the aqueous Cu fraction from other elements in solution. The resin was pipetted into 3 mL polypropylene filtration tubes (Supelco Inc; Bellefonte, PA) to create a bed length of 4 cm. The column was sequentially washed with 2 mL aliquots of 7 M HCl, 2 M HCl, 0.5M HCl and ultrapure Milli-Q water 15 times each, then regenerated with 10 additional 2 mL aliquots of HCl. Copper isotope samples were prepared in Savillex Teflon vials in small volumes containing precisely 10 µg of Cu. These subsamples were evaporated on a hotplate. The remaining Cu-containing pellet was then redissolved in 7 M HCl and loaded onto

the resin. The Teflon vials were rinsed twice with 7 M HCl which was added to the separation columns to ensure all the Cu in each purification sample was loaded onto the anion-exchange resin for extraction. A 50 mL volume of 7 M HCl was passed through the resin by gravity filtration to recover the Cu from the isotope sample. This 50 mL was then evaporated on a hotplate overnight in Teflon vials until only a solid Cu pellet remained. The remaining solid Cu pellet was redissolved in 7 M HCl, evaporated again and dissolved once more in 0.5M HNO_3.

A diluted subsample of the purified Cu sample was rechecked on the ICP-OES to ensure a Cu yield of 95-105% recovery. The Cu was then diluted to roughly 200 μg L^{-1} in a 3% HNO_3 solution and the Cu concentration in the samples was confirmed to agree with the Cu concentration in a reference solution (prepared with international standard ERM-AE633) within 10%. This sample was analyzed for ^{63}Cu and ^{65}Cu using a multicollector inductively coupled plasma mass spectrometer (MC-ICP-MS; Neptune; Thermo Scientific) using a standard-sample bracketing technique.

Cu isotope data is presented using δ notation and also by fractionation factors calculated by:

$$\alpha = \mathrm{R}_{\mathrm{product}}/\mathrm{R}_{\mathrm{reactant}} \qquad (2.2)$$

where R is the isotope ratio of the product or reactant. For ease of interpretation, α values are converted to isotope fractionation values, ε, related by the formula, as outlined by Coplen (2011):

$$\varepsilon = (\alpha - 1) \times 1000‰ \qquad (2.3)$$

The Rayleigh distillation isotope model was used to characterize isotope fractionation in this experiment, based on the Eq. (2.4)

$$\frac{R}{R_0} = f^{(a-1)} \qquad (2.4)$$

where R is the isotope ratio of a sample, R_0 is the isotope ratio of the initial solution, f, is the fraction of Cu in solution, and α is the fractionation factor. Equation 2.4 was rearranged to solve for α by fitting a linear regression to a plot of natural log transformed f versus δ values. The coefficient of determination, or R^2 value, for this regression provides a statistical measure of how close the isotope data are fit by the linear regression defined by α.

2.4 Results

The results presented in this chapter are primarily based on bulk geochemistry and Cu XANES data from FTC II. Cu FTC I data is included in the Appendix A. The design of FTCs I and II was similar, except for lengths of flow rate steps. Data from FTC II was used in the calculation of the isotope fractionation factor.

2.4.1 Aqueous Geochemistry

The conditioning of ZVI with ultrapure water produced an initial effluent pH of 8.7 (Figure 2.1). With the addition of Cu to the system, the pH declined to 5.9 over the first 7,000 PV of flow and remained near this value (ranging from 5.3 to 6.2) for the remainder of the experiment (37,000 PVs of flow in total).

An Eh value of -435 mV was attained by the end of the conditioning period (Figure 2.1), consistent with the expected Eh range for ZVI-treated ultrapure water in column and batch laboratory experiments (Blowes et al., 2000; Gui et al., 2009). Negative Eh values indicate reducing conditions ideal for promoting electron transfer from aqueous Cu^{2+}. The Eh values measured in the FTC effluent increased to 0 mV after the Cu input solution was introduced, fluctuated substantially (± 200 mV), and then stabilized at 200 mV around 7,000 PVs for the remainder of the experiment. These trends in pH and Eh values mirror each other, where a rise or fall in pH corresponded with the opposite response in redox potential.

The average influent Cu concentration was 10.02 ± 0.28 mg L^{-1} over 37,000 PVs of flow. Copper was detected in the effluent solution shortly after 6,000 PVs, and rose to 6.8 mg L^{-1} by 8,500 PVs (Figure 2.2). After a brief decline between 8,500 and 10,500 PVs, Cu concentrations steadily increased to the end of the experiment, approaching the input concentration. The average S concentrations in input and effluent samples were 4.54 ± 0.15 mg L^{-1} and 4.51 ± 0.21 mg L^{-1} respectively, indicating no S was not removed from solution during the experiment. Total dissolved Fe in the effluent averaged 8.7 ± 0.31 mg L^{-1} through 6,400 PVs before sharply decreasing, in contrast to Cu, which exhibited the opposite trend. Fe concentrations then stabilized, reaching 1.1 mg L^{-1} at the end of the experiment. Throughout the experiment, effluent concentrations of Na, Ca and Mg remained below the analytical detection limit (<0.2 mg L^{-1}). Concentrations of K fluctuated between 3.6 and 0.5 mg L^{-1} over the first 6,200 PVs, and were undetectable in all effluent samples after this time. These results indicate that Cu and Fe are the primary cations of interest for the interpretation of Cu removal by ZVI in the FTC. The mass of Cu retained in the FTC is proportional to the effluent Fe, where the ratio of $Cu_{(s)}$:$Fe_{(aq)}$ is approximately 1:1 in regards to moles of each element (Table 2.1).

The differences in Cu concentrations in the influent and effluent samples were used to calculate the mass of Cu accumulated in the FTC. The mass of Cu retained on the ZVI in the FTC increased linearly from 0 to 6,300 PVs (Figure 2.3A), followed by a gradual decrease in the rate of Cu accumulation thereafter. A total of 863 mg Cu was accumulated over 37,000 PVs on the 1.60 g of ZVI, representing removal of 225.5 mg Cu per g ZVI, or an average of 5.4×10^{-3} mg Cu per g ZVI per PV (Figure 2.3). This rate of solid Cu formation produced a mass of Cu sufficient to form visible metallic red flakes (likely elemental Cu) non-uniformly throughout the FTC (Figure 2.3B).

2.4.2 Cu X-ray Absorption Spectroscopy

The location of the Cu *K* absorption edge is 8979 eV (Figure 2.4A, B) and serves as a reference for sample-standard comparisons. The normalized absorbance (μ(E)) spectra of Cu^0, Cu_2O, CuO, $Cu(OH)_2$, and Cu_2S standards are stacked above Cu sample spectra for bulk ZVI grains from bottom (FTC-Bot), middle (FTC-Mid), and top (FTC-Top) positions of the FTC (Figure 2.4A). Spectra for these standards and samples are also presented as a function of wave number (*k*-space) and the Fourier transformed *R*-space to illustrate similarities in higher frequency components beyond the main absorption peak (Figure 2.4 C, D).

The FTC-Mid spectra aligns well with the Cu^0 *K*-edge peak and its post-edge features (Figure 2.4), suggesting the presence of Cu^0 at a central location in the FTC. The FTC II-Bot and FTC II-Top sample spectra include characteristics similar to Cu^0, with contributions from the cuprite (Cu_2O) standard. The absorption edge for Cu_2O is at 8980.5 eV and the first derivative μ(E) spectra depict similar features between Cu_2O and FTC-Bot.

Linear combination fitting (LCF) calculations were conducted on sample spectra to assess the relative contributions of the Cu species that accumulated in the FTC (Figure 2.5). Contributions of Cu_2O and Cu^0 were determined by LCF for FTC-Bot, with slightly greater abundance of the oxide (Table 2.2). The Cu species in FTC-Mid was determined to consist principally of Cu^0. The FTC II-Top spectra exhibits the presence of both Cu_2O and Cu^0, but with greater contributions from Cu^0. The R-factors computed by Athena for the modelled LCF spectra are reported to indicate the goodness of fit for each sample. This parameter is a relative measure of variance between XANES sample spectra and their corresponding fits derived from a selection of standards, where a lowest possible value is desired. The R-factor for each of the three sample fits at top, middle, and bottom FTC positions demonstrate high quality goodness-

of-fits (0.005 to 0.017), suggesting that the solid Cu phase is very likely composed of Cu^0, or a mixture of Cu_2O and Cu^0. A visual examination of Cu sample spectra and the LCF calculations indicate the absence of contributions from CuO, $Cu(OH)_2$ and Cu_2S, suggesting the divalent form of oxidized Cu was not present at measurable quantities in any bulk samples and $SO_4^{2-}{}_{(aq)}$ in the input solution was not removed during treatment. Additional XANES results collected from the intact FTC II are in agreement.

Results of Cu FTC II modeling for EXAFS spectra (Table 2.4) indicate coordination numbers, CN, and bond lengths, R (Å), for Cu scattering paths based on Cu^0 and Cu_2O structures. The CN numbers of Cu—Cu bonds for first shell fittings of the FTC II-Bot sample were 2.4 and 7.8 for Cu^0 and Cu_2O respectively. The FTC II-Mid sample, comprised predominantly of Cu^0 based on the LCF results (Table 2.2) has a CN of 12 for Cu—Cu. Cu^0 and Cu_2O contributed to the LCF for FTC II-Top, and CNs of 12 were derived in EXAFS modeling for Cu—Cu bonding in both reduced Cu phases.

2.4.3 Copper Isotope Fractionation

Cu isotope ratios presented in this study are from aqueous samples. The $\delta^{65}Cu$ measurements of the unfractionated input solutions are contrasted with $\delta^{65}Cu$ values for the effluent to infer the extent of fractionation associated with Cu removal in the FTC.

Increasing Cu concentrations in FTC effluent samples over time correspond to a gradual decrease in the $\delta^{65}Cu$ isotope ratio in solution. All effluent samples were enriched relative to the 0.27 ± 0.05 ‰ $\delta^{65}Cu$ average of the Cu input solutions (normalized to 0.00 ± 0.05 ‰ $\delta^{65}Cu$; Figures 2.7, 2.8). The greatest fractionation occurred when Cu initially reacted with ZVI. The $\delta^{65}Cu$ for the effluent sample at C/C_0 0.095 (1,500 PVs) was 1.30 ± 0.03 ‰, and was the earliest

effluent sample for which $\delta^{65}Cu$ measurement was possible due to sufficient mass of recoverable Cu required for analytical measurement. Therefore, the maximum extent of fractionation relative to the input ($\delta^{65}Cu_{input}$ - $\delta^{65}Cu_{max\ effluent}$) observed in this study was 1.03 ‰. The magnitude of fractionation rapidly decreased as Cu effluent concentrations increased sharply from 6,300 to 11,000 PVs. The fraction of Cu in solution (*f*) was approximately 0.8 at 11,000 PVs. Throughout the remainder of the experiment, $\delta^{65}Cu$ values stabilized with minimal variation.

The trend in $\delta^{65}Cu$ values increased exponentially with less Cu in solution (Figure 2.7), consistent with Rayleigh distillation processes. Although FTCs are not closed systems, the well-maintained conditions of a consistent anaerobic setting and constant 10 mg L^{-1} Cu input resulted in isotope behaviour best described using this model. Other researchers have also successfully extended Rayleigh distillation theory to metal isotope fractionation under saturated flow conditions (Jamieson-Hanes et al., 2012; Jamieson-Hanes et al., 2014). An isotope fractionation factor, (α) of 0.99972, or -0.31 ‰ in ε notation, was determined by fitting a Rayleigh curve to all FTC II data (Figure 2.7). This approach produced an R^2 value of 0.85.

2.5 Discussion

2.5.1 Aqueous Geochemistry and Cu Removal

The pH and Eh trends observed during the experiment are a function of the evolution of ZVI corrosion and Cu removal within the FTC. Before Cu entered the system, the values measured in the FTC effluent during the ZVI conditioning period (Figure 2.1A) were strongly reduced, as expected due to ZVI corrosion in an anoxic, anaerobic environment, according to the following reaction (Furukawa et al., 2002; Reardon, 2005):

$$Fe^{0}_{(s)} + 2H_2O_{(aq)} \rightarrow Fe^{2+} + H_{2(g)} + 2OH^{-}_{(aq)} \quad (2.5)$$

The standard electrode potential (SEP) for the half reaction involving the addition of electrons to water molecules is -0.83V in a ZVI barrier (Rangsivek, 2010), where hydroxide is favoured as a product, resulting in the increase in effluent pH to 8.7 prior to Cu treatment. Elevated concentrations of Fe^{2+} are released through Eq. 2.5 during anaerobic corrosion, promoting the formation of ferrous hydroxide, ferrous hydroxycarbonate and magnetite (Odziemkowski et al., 1998; Rangsivek, 2010; Jeen et al., 2009). Ferrous hydroxide is metastable, often transforming to magnetite through:

$$Fe^{2+} + 2OH^- \rightarrow Fe(OH)_{2(s)} \quad (2.6)$$

$$3\ Fe(OH)_2 \rightarrow Fe_3O_4 + H_2 + 2H_2O \quad (2.7)$$

After the addition of 10 mg L^{-1} Cu input solution, large fluctuations in pH and Eh can be attributed to imbalances caused by reaction of Cu with ZVI as the FTC system approached steady-state. An overall decrease in pH was associated with Cu reduction by ZVI in Cu FTC II. This pH trends indicates a net production of $H^+_{(aq),}$ which resulted in a weakly acidic pH after 6,800 PVs (Figure 2.1). This trend is likely due to the oxidation of Fe^0 to Fe^{2+} resulting in precipitation of $Fe(OH)_2$ and uptake of OH^- during the formation of iron oxide corrosion products. This decrease in pH contrasts with other FTC experiments. For example, a sharp pH increase coupled to a decrease in Eh during Cr(VI) reduction by ZVI was observed by Jamieson-Hanes et al. (2014). It is widely reported that Cu cementation under anaerobic conditions occurs at acidic pH where Fe is relatively soluble (Ku and Chen, 1992; Rangsivek, 2010). A consistent pH of 5.9 recorded after the addition of Cu to the FTC was observed in this experiment (Figure 2.1). The stable pH and Eh after 6,800 PVs indicates consistency in the geochemical processes involved in the removal of Cu throughout the experiment.

The net reaction for electron transfer between Fe^0 and aqueous Cu^{2+} is (Ku and Chen, 1992; Rangsivek, 2010):

$$Fe^0_{(s)} + Cu^{2+} \rightarrow Fe^{2+} + Cu^0_{(s)} \qquad (2.8)$$

Comparing the standard electrode potential (SEP) values for Fe^0/Fe^{2+} and Cu^0/Cu^{2+}, Cu reduction is expected. The SEP values for the two half reactions comprising Eq. 2.8 are as follows:

$$Cu^{2+} + 2e^- \leftrightarrow Cu^0 \qquad SEP = +0.34\ V \qquad (2.9)$$

$$Fe^0 \leftrightarrow Fe^{2+} + 2e^- \qquad SEP = -0.44\ V \qquad (2.10)$$

The formation of elemental Cu through these reactions is consistent with the accumulation of Cu observed in this study (Figure 2.3B). Zero-valent iron has a large capacity for Cu reduction over an extended period, as indicated by Cu^{2+} immobilization for the duration of the experiment (Figure 2.3A).

The contrasting trends of Cu^{2+} and Fe_T in solution (Figure 2.2) are primary indicators that electron transfer from Fe^0 to Cu^{2+} resulted in less Fe entering solution than expected based on the stoichiometry of Eq. 2.8. As Cu concentrations increase in effluent samples over time, the rate of Cu loading onto ZVI gradually declines (Figure 2.3A), thus reducing the quantity of free Fe ions in solution. The trend in dissolved Fe_T concentrations mirrors aqueous Cu^{2+} (Figure 2.2), indicating a well-correlated geochemical link between Cu and Fe in the FTC, likely controlled by Eq. 2.8, where increasing Cu in the solid phase is balanced by increasing Fe in the aqueous phase due to the phase transitions associated with electron transfer between Fe and Cu.

The relationship between the Cu input solution flow rate and rate of ZVI corrosion is important for consistent, long-term removal of Cu. Copper effluent concentrations in FTC I stabilized at each flow rate (Figure S2.1), and reached a maximum C/C_0 of 0.65, therefore a

stepped-flow rate approach was adopted to promote Cu breakthrough. This technique was employed at the onset of the FTC II test to increase the mass of Cu in solution over time. The stepped-flow rate approach produced a sample array with a maximum C/C_0 (Cu in solution relative to the input) of 0.94 (Figure 2.2). A decline in ZVI reactivity over time likely caused an increase in effluent Cu concentrations. Continual loading of Cu onto ZVI resulted in the formation of visible Cu-bearing solids within the FTC (Figure 2.3), suggesting the accumulation of Cu reduction products is likely one factor contributing to the passivation of ZVI.

2.5.2 X-ray Absorption Spectroscopy and Cu Removal Mechanisms

The XANES sample spectra are consistent with the features of $Cu^0_{(s)}$ and $Cu_2O_{(s)}$ standard spectra. Equation 2.11 outlines a plausible reaction pathway for Cu_2O co-precipitation following reduction of Cu^{2+} by ZVI using Fe^{3+}, a potential intermediate product on ZVI surfaces under acidic pH in a non-aerated solution (Rangsivek and Jekel, 2005).

$$2\ Cu^0_{(s)} + Fe^{3+}_{(s)} + 3\ H_2O \rightarrow Cu_2O_{(s)} + Fe(OH)_{2(s)} + H_2 \qquad (2.11)$$

The similar masses of Cu^0 at each location and favourable thermodynamics of Eq. 8 suggest that reduction to Cu^0 is the dominant removal mechanism during the majority of the FTC II experiment. As the surface sites of ZVI were increasingly covered by Cu^0, the system reached a point where Cu_2O production was in effect at the FTC top and bottom. As demonstrated in Eq. 2.11, Fe^{3+} is a potential oxidant, leading to the formation of Cu_2O. Ferric Fe is more likely to be found near the influent and effluent ports of the FTC where intrusion of trace amounts of O_2 was more likely. The greater potential for Fe^{3+} to be present near the ports may have influenced the observation of Cu_2O at top and bottom locations in the FTC, shown by the LCF results in Table 2.2.

2.5.3 Cu Isotope Fractionation

The high uptake capacity of freshly conditioned ZVI led to near-complete removal of dissolved Cu in the first 6,300 PVs, therefore Cu isotope measurements could not be made during this stage of the experiment. Raising the flow rate to increase Cu concentrations over time yielded a change in C/C_0 of 0.85 (0.09 to 0.94 C/C_0) for FTC II. The most rapid increase in Cu concentrations occurred from 6,300 to 8,500 PVs, where dissolved Cu increased 7 mg L^{-1} in the FTC II effluent (Figure 2.2). In FTC II, a broader range in *f* values was obtained compared to FTC I. The $\delta^{65}Cu$ isotope values show that the Rayleigh model is in agreement with the experimental data (Figure 2.7, $R^2 = 0.77$). When dissolved Cu^{2+} becomes enriched in ^{65}Cu at early time, the rate of Cu reduction is greatest (Figure 2.3).

A single Rayleigh curve can be used to describe the full isotope dataset, suggesting that ε is correlated to a dominant geochemical process (Veeramani et al., 2015). All $\delta^{65}Cu$ sample points in this study are enriched with respect to the input (Figure 2.7), and become increasingly enriched in ^{65}Cu as aqueous Cu concentrations decrease (Figure 2.8).As previously described, reduction to Cu^0 was likely the dominant form of attenuation. Therefore, the maximum measured $\delta^{65}Cu_{effluent}$ value of 1.03 ‰ relative to the input value is attributable to Cu^{2+} reduction by pathways inclusive of both solid phases. Following the formation of Cu^0 evenly throughout FTC II, the production of Cu_2O was potentially derived from reoxidation of Cu^0 on the surface of ZVI grains. This would not affect the aqueous pool of Cu species, supporting the attribution of Cu^0 formation as the primary influence on isotope fractionation in FTC II.

An assessment of aqueous and solid Cu coordination is consistent with the isotope enrichment observed in aqueous effluent samples following ZVI reduction. With greater Cu immobilization (lower *f* range), $\delta^{65}Cu$ values were enriched in effluent samples (Figure 2.7),

coinciding with greatest fractionation at peak rates of Cu^0 formation. This finding agrees with the common observation that redox reactions impart greater enrichment of ^{65}Cu in more oxidized states of Cu (Balistrieri et al., 2008; Ehrlich et al., 2004; Markl et al., 2006; Schauble, 2004; Zhu et al., 2002).

The coordination of Cu in various oxidation states and phases is fundamental to understanding Cu isotope partitioning. XAFS spectroscopy performed by Fulton et al. (2000) built on the traditional understanding that Cu^{2+} (derived from $CuBr_2$ and $Cu(NO)_3$) existed in octahedral formation with four equatorial 1.97 Å Cu—O bonds and two axial bonds ~2.38 Å in length. Musinu et al. (1983) determined Cu^{2+} coordination at 20ºC with a 1.37 M Cu input derived from $CuSO_4$, the same initial salt used in this study. Four water molecules were observed with Cu in square-planar configuration with two equatorial Cu—O bonds of 1.97-1.98 Å and two at axial positions of 2.34-2.39 Å bond lengths (Musinu et al., 1983), similar to the bond lengths measured by Fulton et al. (2000).

Neutron diffraction and first-principles molecular dynamics used to interpret a hydrated Cu(II) structure indicated fivefold coordination rather than the previously accepted Jahn-Teller distorted octahedral configuration (Pasquarello et al., 2001). Pasquarello et al. (2001) proposed that the solvated Cu complex undergoes transitions between pyramidal and trigonal bipyramidal formations, a theory consistent with experimental data obtained from other visible near-infrared, XANES, and nuclear magnetic resonance methods. The proponents of the fivefold coordination complexes infer Cu—O nearest neighbour bond lengths ranging from 1.94 to 2.00 Å on the equatorial plane, while the bond lengths of axial bonds were less accurately determined to range from 2.12 to 2.60 Å (Pasquarello et al., 2001). This structure is cited as the more recently developed theory for aqueous Cu coordination (Chaboy et al., 2006; Ehrlich et al., 2004). A

square pyramidal fivefold geometry with four oxygen atoms in equatorial coordination with a fifth slightly longer Cu—O on the apical axis was also proposed (Benfatto et al., 2002).

There is a general consensus that the traditionally preferred octahedral structure established by Jahn-Teller effects is a dynamical effect of a metal aquaion capable of a diverse set of geometries ranging between four-, five-, and six-fold coordination (Chaboy et al., 2006). Structural modelling performed on Cu^{2+} in a Cl-free solution with a pH less than 7 (similar to this study) yielded a five-fold Cu coordination which was composed of a dynamical average between the square-planar $Cu(H_2O)_4^{2+}$ and Jahn-Teller distorted $Cu(H_2O)_4(H_2O)_2$ complexes (Sherman, 2013). The optimized geometry of this five-fold complex resulted in four water molecules at bonds of 1.99 Å equatorial distances and the fifth axial molecule at 2.20 Å (Sherman, 2013). A summary of EXAFS studies concludes that Cu can be expected to complex with three to four equatorial oxygen atoms averaging 1.96 Å and one to two axial bonds of 2.35-2.36 Å in a transiently coordinated state (Chaboy et al., 2006). Estimated bond lengths based on Fourier transform spectra from this study are compared with previously reported coordination and crystal structure parameters (Table 2.3). The majority of Cu atoms from the input solution formed elemental Cu upon reduction by ZVI, revealed by the high abundance of Cu^0 in the solid phase.

The crystal structure of Cu^0, and Cu coordination in cuprite are also of interest for contrasting isotope behaviour with different geometric configurations between the aqueous phase and two solid phases determined through XANES. The coordination number for Cu atoms in elemental form is 12, with a lattice constant of 3.61 Å and a face-centered cubic (fcc) crystal structure (Straumanis and Yu, 1969). The EXAFS results from FTC II-Mid and FTC II-Top are consistent with this CN (Table 2.4). Elements with lower coordination numbers and shorter bond

lengths tend to concentrate heavier isotopes (Balistrieri et al., 2008; Schauble, 2004; Wiederhold, 2015). Copper in the solid phase of this study has a higher coordination number (CN = 12) compared to Cu—Cu bonds in the aqueous phase, where CN is approximately 5 ± 1 based on widely accepted values in the literature on Cu coordination. The coordination number for Cu—O in cuprite is four, while adjacent Cu atoms are linearly coordinated (CN for Cu—Cu = 2) (Korzhavyi and Johansson, 2011). However, Cu_2O is likely a secondary reaction product that formed following elemental Cu production, and less likely to influence aqueous to solid Cu partitioning, which is inherent to the isotope fractionation of aqueous samples. Cuprite was only observed at the margins of the FTC, whereas Cu^0 was found throughout the FTC (inferred by XAS fitting). The greater contribution of Cu^0 in the linear combination fitting suggests it is of primary importance as a reservoir for Cu, and had the greatest effect on Cu isotope fractionation during the removal of Cu^{2+}. The bulk of the solid phase (Cu^0) therefore has a higher coordination number than the aqueous phase (12 versus five), favouring enrichment of $\delta^{65}Cu$ in effluent samples.

Most Cu isotope studies present isotope ratios relative to the NIST SRM 976 standard. In 2012, this international standard was replaced by ERM-AE633, the Cu isotope standard employed in this study for analytical measurement. To compare older Cu isotope literature with new studies, NIST SRM 976 was calibrated against ERM AE633 to determine the $\delta^{65/63}Cu$ offset to provide a conversion adjustment (Moeller et al, 2012). NIST SRM 976 produced a $\delta^{65/63}Cu_{AE633}$ value of -0.01 ± 0.05 ‰, allowing for comparison between Cu isotope studies employing different reference materials.

Copper fractionation measured in this study is unique as the observed isotope fractionation followed a Rayleigh trend (Figure 2.7). The isotope fractionation value here of -

0.31 ‰ for Cu reduction by ZVI under saturated flow is less than the fractionation observed for Cu^{2+} reduction to Cu^{1+} by Zhu et al., (2002) who report a mean ε of 4.03 ‰ in batch experiments employing a $Cu(NO)_3)_2$/KI mixture to precipitate CuI (Table 2.5). Balistrieri et al. (2008) report fractionation for Cu^{2+} adsorption (ε = -0.73 ‰) onto amorphous Fe(III) (oxy)hydroxides in the same direction, that was two and a half times larger in magnitude than in this study.

The $\Delta_{soln\text{-}solid}$ separation factor is a widely used parameter to describe aqueous to solid phase partitioning of Cu in geochemical remediation or mineralization reactions. Isotope measurements on the solid phase were not measured in this saturated flow experiment, therefore $\Delta_{soln\text{-}solid}$ values were not determined here. Ehrlich et al. (2004) measured a $\Delta^{65}Cu_{soln\text{-}solid}$ of 3.06 ‰ for Cu^{2+}/Cu^{1+} reduction during covellite precipitation from an initial $CuCl_2$ salt, which exceeds $\Delta^{65}Cu_{soln\text{-}solid}$ for studies involving immobilization of Cu through other geochemical processes (Table 2.5). Secondary precipitation of cuprite was predicted to yield a $\Delta^{65}Cu$ enrichment of 1.2 ‰ in solution relative to the solid phase at 25ºC (Sherman, 2013). Other studies report larger $\Delta^{65}Cu$ values (up to ~3 ‰) and ε values for the reduction of $Cu^{2+}_{(aq)}$ to Cu^{1+} solids (Ehrlich et al., 2004; Markl et al., 2006; Zhu et al., 2002). The ε value (-0.31) and maximum enrichment relative to the input ($\delta^{65}Cu$ = 1.03 ‰) measured here for Cu^{2+} reduction is in the low to moderate range of magnitudes reported for fractionation during Cu attenuation in the literature (Table 2.5).

The low to moderate degree of fractionation observed here is likely influenced by the system operating under constant flow as opposed to a perfectly closed reservoir. Three factors may contribute to the relatively small fractionation factor determined in this study: (1) metal isotope fractionation in laboratory studies tends to produce larger α values under closed-system

conditions, as in batch experiments, versus saturated flow conditions where the system is inherently open; (2) the rapid rate of Cu reduction by ZVI is limiting the exchange of ^{63}Cu from solution; (3) to maintain consistent Cu removal and achieve increasingly greater breakthrough, the flow rate was increased stepwise throughout the experiment, leading to lower residence times as the experiment progressed.

Stable isotope fractionation can involve kinetic or equilibrium processes, either of which may occur during Rayleigh distillation if isotope exchange is irreversible between the product and reactant phases (Weiss et al., 2008). Isotope enrichment in one reservoir must be balanced by depletion in another reservoir (Wiederhold, 2015), which is the case for enriched Cu^0 and depleted aqueous Cu^{2+}. The rates of Cu^{2+} reduction and formation of solid Cu^0 can be approximated with first-order kinetics (Ku and Chen, 1992). Copper removal was > 98.2% (with the exception of two outlier samples) over the first ~6000 PVs for Cu FTC II (Figure 2.2), because of continuous high efficiency Cu^{2+} reduction and Cu^0 formation.

2.5.4 Implications for Groundwater Management

Knowledge of Cu isotope fractionation associated with specific removal mechanisms, such as reduction, can provide a tool for geochemical characterization of contaminated field sites. In groundwater monitoring programs that rely on aqueous geochemistry, the isotope composition of samples within a PRB can be compared to the isotope ratio of samples from the contaminated plume upgradient of the PRB. As the effectiveness of ZVI deteriorates with long-term copper uptake, the samples from within the barrier will likely exhibit isotope composition similar to the incoming contaminated groundwater. The ε reported here offers an indication of the magnitude of fractionation associated with Cu reduction by ZVI. Monitoring the

effectiveness of a remediation strategy often relies on collection of groundwater samples and subsurface cores for thorough characterization of geochemical conditions at a site. Clarifying reaction mechanisms by aqueous isotope measurements may decrease dependence on costly sampling programs, and lead to more efficient use of resources. These measurements can offer novel insight into geochemical reaction mechanisms occurring on a broad scale to assist in the design of more efficient remediation systems.

2.6 Conclusions

A FTC experiment was performed to assess Cu isotope fractionation during Cu^{2+} reduction by ZVI under saturated flow conditions. A moderate degree of isotope fractionation (a difference of 1.03 ‰ between the $\delta^{65}Cu$ values for the input and lowest measurable *f* range sample) was associated with the Cu immobilization process. X-ray absorption near-edge spectroscopy confirmed the presence of Cu^0 at each measured location in the FTC. Cuprite, a basic Cu^{1+} oxide, was also identified, in abundances approximately equal to Cu^0, in samples collected from the top and bottom of the FTC. EXAFS modeling confirmed the CN = 12 for elemental Cu at middle and top locations of FTC II; this finding is helpful for attributing a change in CN to the shift in isotopes.

The Rayleigh model fit for $\delta^{65}Cu$ values between 0.27 ‰ ($\delta^{65}Cu_{input}$) and 1.30 ‰ over the complete C/C_0 range was acceptable, suggesting that reduction to Cu^0 (revealed by XANES) was the primary reaction influencing fractionation of dissolved Cu isotopes. An isotope fractionation value (ε) of -0.31 ‰ was determined by fitting the Rayleigh model, which revealed consistent depletion in the ^{65}Cu isotope in solution with increasing Cu breakthrough. The CN of $Cu^{2+}_{(aq)}$ is reported as 5 in recent EXAFS literature, indicating an increase in CN from approximately 5 to 12 as ^{65}Cu is enriched in the aqueous phase during reduction of $Cu^{2+}_{(aq)}$ to $Cu^0_{(s)}$. The degree of

isotope fractionation (ε = -0.31 ‰) from FTC II provides a benchmark for identifying geochemical processes controlling Cu immobilization in remediation systems employing ZVI as a PRB material.

Table 2.1 Attenuation and breakthrough of Cu and Fe with differing periods of flow rate

Flow Rate ($mL\ hr^{-1}$)	**Pore Volumes**	**Cu in Influent** ($mg\ L^{-1}$)	**Cu Mass in Input** (mol)	**Cu in Effluent** (mol)	**Rate of Cu Removal** ($mol\ hr^{-1}$)	**Cu Retained in FTC** (mol)	**Fe in Effluent** (mol)
11	1090	9.93	4.00×10^{-4}	1.18×10^{-7}	2.01×10^{-9}	3.99×10^{-4}	3.81×10^{-4}
22	1470	10.08	5.48×10^{-4}	3.59×10^{-7}	3.03×10^{-9}	5.37×10^{-4}	5.35×10^{-4}
33	1090	9.92	4.00×10^{-4}	8.76×10^{-7}	1.59×10^{-9}	3.96×10^{-4}	4.08×10^{-4}
44	3565	10.18	1.34×10^{-3}	5.05×10^{-7}	1.12×10^{-8}	1.25×10^{-3}	1.08×10^{-3}
66	7915	10.06	2.94×10^{-3}	3.01×10^{-7}	9.82×10^{-8}	1.12×10^{-3}	9.29×10^{-4}
76	4760	10.20	1.79×10^{-3}	2.66×10^{-7}	1.09×10^{-7}	5.79×10^{-4}	4.47×10^{-4}
87	11460	9.99	4.23×10^{-3}	2.63×10^{-7}	1.27×10^{-7}	8.72×10^{-4}	7.89×10^{-4}
96	5685	10.01	2.10×10^{-3}	1.05×10^{-5}	1.30×10^{-7}	3.68×10^{-4}	2.96×10^{-4}
TOTAL	**37035**	**-**	1.38×10^{-2}	8.24×10^{-3}	**-**	$\mathbf{5.51\times10^{-3}}$	$\mathbf{5.35\times10^{-3}}$

Table 2.2 Weights given to standards fit to Cu FTC II samples in Linear combination fitting of μ(E) spectra

Sample	Cu^0	Cu_2O	CuO	$Cu(OH)_2$	Cu_2S	R-factor
Cu FTC II – Bot	40.3	63.9	-	-	-	0.017
Cu FTC II – Mid	100.0	0.03	-	-	-	0.005
Cu FTC II – Top	58.8	43.3	-	-	-	0.013

Weights of standards were not forced to sum to 1 during LCF. A fitting region of -20 eV to 30 eV was employed. The R-factor is a measure of variance between the raw XANES spectra and the LCF fits reported by Athena.

Table 2.3 Structural coordination properties for Cu—Cu and Cu—O bonds in the attenuated Cu phases in FTC II

Phase	Distribution of Cu in FTC	Scatterer	Crystal Structure	CN	R (Å)	Source
$\mathbf{Cu_2O_{(s)}}$	Bottom > Top	Cu—O	Tetrahedral	4	1.84	*1*
		Cu—Cu	Linear	2	3.02	*1*
$\mathbf{Cu^0_{(s)}}$	Middle > Top > Bottom	Cu—Cu	Face-centered cubic	12	2.55	*2, 3*
$\mathbf{Cu^{2+}_{(aq)}}$	N/A	$Cu—O_{eq}$ $Cu—O_{ax}$	Square-planar/ pyramidal/trigonal bipyramidal/octahedral	4	1.96-1.98	*4, 5*

Subscripts designated to scatterers refer to equatorial (eq.) and axial (ax.) positioned atoms in the same coordination structure.

References: 1. Korzhavyi and Johansson (2011), 2. Straumanis and Yu (1969), 3. Murphy (1993), 4. Chaboy et al. (2006), 5. Pasquarello et al. (2001). Reference 1 indicates the shortest distances between a pair the stated pair of atoms in Cu_2O.

Table 2.4 EXAFS summary of first shell fits around a central Cu atom for Cu FTC II samples

Sample ID	Scatterer	CN	R (Å)	σ^2 (Å^2)	R-factor
FTC II-Bot	Cu—Cu1 [Cu_2O]	7.8	3.03	0.0183	0.0199
	Cu—O1 [Cu_2O]	1.3	1.86	0.0002	
	Cu—O2 [Cu_2O]	3.9	3.56	0.0056	
	Cu—Cu1 [Cu^0]	2.4	2.57	0.0086	
FTC II-Mid	Cu—Cu1 [Cu^0]	12	2.55	0.0098	0.0039
FTC II-Top	Cu—O1 [Cu_2O]	2	1.85	0.002	0.0069
	Cu—Cu1 [Cu_2O]	12	3.02	0.016	
	Cu—Cu1 [Cu^0]	12	2.55	0.006	

Bond lengths and coordination numbers in this study were estimated from basic XAFS fitting in Artemis, a component of the IFEFFIT software package for processing XAS data.

Scatterer indicates the path being analyzed between absorbing and scattering atoms, where the number on the scatterer denotes the shell this atom exists in. The Cu species in square brackets denotes the standard from which a given scattering path was referenced to model the sample spectra.

CN = coordination number. R = modeled bond length. σ^2 = the mean-square displacement of bond length. *R* factor = goodness of fit statistic.

Table 2.5 Overview of published isotope fractionation for reduction, precipitation and adsorption mechanisms attributed to the removal of copper in low temperature geochemical environments

Reaction Type	Solid Phase Product	δ^{65}Cu Ratios (‰)		Associated Fractionation		Reference
		Initial/ Input	Solid/ Effluent	$\Delta_{soln\text{-}solid}$ (‰)	ε (‰)	
Adsorption (Fe oxides)	$Cu^{2+}_{(s)}$	-	-	-0.73 ± 0.08	-0.73	*1*
Ads. (soils)	$Cu^{2+}_{(s)}$	0.32 to 0.64	-	0.26 ± 0.11	-	*2*
Ads. (gibbsite)	$Cu^{2+}_{(s)}$	0.07	-	1.0 ± 0.25	-	*3*
Ads. (goethite)	$Cu^{2+}_{(s)}$	0.07	-	0.78 ± 0.2	-	*3*
Precipitation	Cu_3AsS_4	1.22 to 1.35	0.30	1.6 ± 0.14	~1.4	*4*
	$CuFeS_2$	1.09 to 1.65	0.00	1.43 ± 0.14	~1.0	*4*
Precipitation/ Reduction	$Cu^{(1+)}S$	-	-	3.06 ± 0.14	-	*5*
	$Cu(OH)_2$	-	-	0.28 ± 0.02	-	*5*
Precipitation	Cu^{2+} sulfides	-	-	3.02 ± 0.14	-	*6*
Precipitation	Cu^{1+} minerals	-	0.41 to 1.66	-	-1.6 to 3.7	*7*
Precipitation	$CuFeS_{2(s)}$	-0.49	1.15	-1.64	0.2 to 1.0	*8*
Precipitation/ Reduction	Cu_2O	-	-	1.2	-	*9*
Reduction	Cu^{1+}	-	-	-	0.40	*10*
Reduction	Cu^0	-	-0.03	-	-	*11*
(natural)	Cu^0 with Cu_2O	-	1.27			*11*
Reduction	Cu^0	0.27	0.29 to 1.30	-	-0.231	This study

For studies assessing the $\Delta_{soln\text{-}solid}$ in the literature, this is also known as the separation factor.

All δ^{65}Cu from other studies employ NIST SRM 976 for their isotope measurements. This reference material yields a $\delta^{65}Cu_{\ ERM\ AE633}$ value of -0.01 ± 0.05 (Moeller et al., 2012), allowing for comparison among studies.

References: *1*. Balistrieri et al. (2008), *2*. Bigalke et al. (2010), *3*. Pokrovsky et al. (2008), *4*. Kimball et al. (2009), *5*. Ehrlich et al. (2004), *6*. Asael et al. (2006), *7*. Markl et al. (2006), 8. Mathur et al. (2012), *9*. Sherman et al. (2013), *10*. Zhu et al. (2002), *11*. Larson et al. (2003).

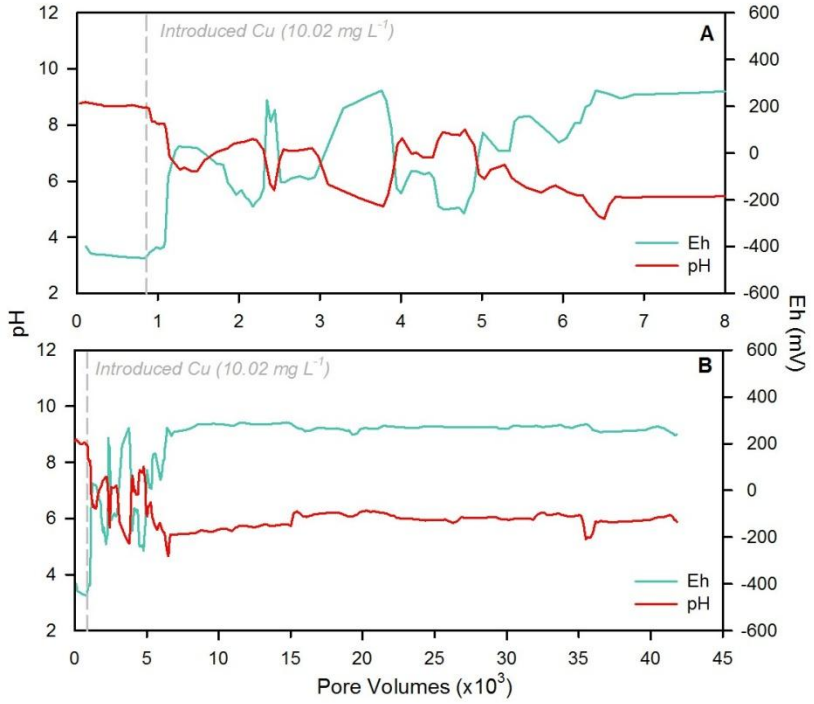

Figure 2.1 (A) Changes in microelectrode pH and Eh at early time clarifying the variation between conditioning and experimental geochemistry, and **(B)** pH and Eh data logged hourly over the full experiment. Data was filtered of 2σ outliers and smoothed with a five-point boxcar technique.

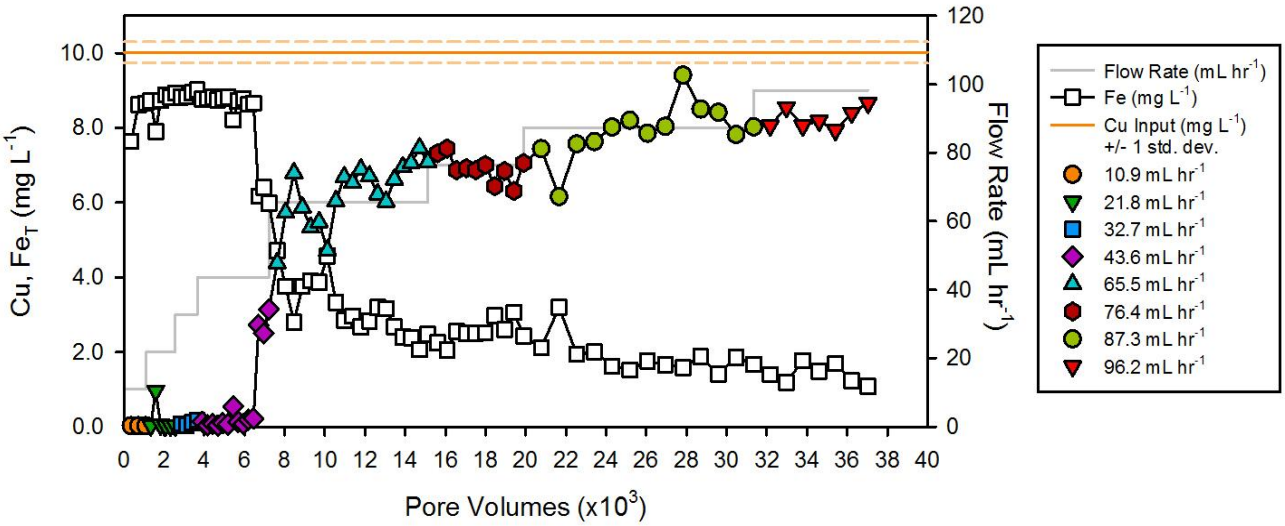

Figure 2.2 Summary of Cu and Fe_T concentrations (mg L^{-1}) in effluent samples and flow rate as a function of reaction time (PVs) in Cu FTC II containing a 10 vol. % ZVI-silica sand mixture. The flow rate of a 10 mg L^{-1} Cu input solution (light gray background line) was incremented progressively with a peristaltic pump to maintain Cu breakthrough.

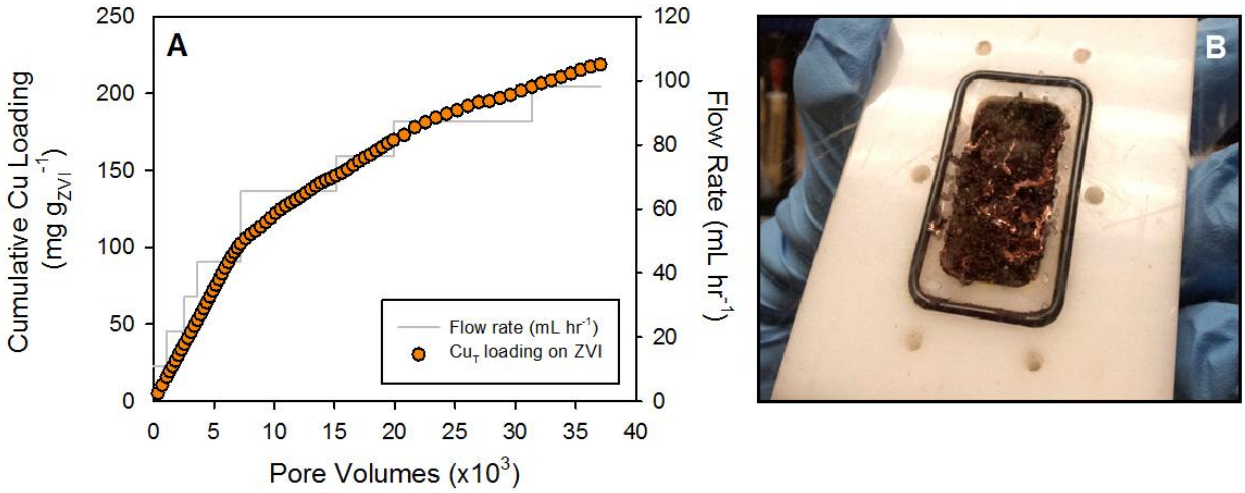

Figure 2.3 **(A)** The cumulative mass of Cu loaded onto ZVI grains, calculated by estimating the amount of Cu removed from solution based on effluent concentrations. Copper removal facilitated by ZVI was maintained over the course of the experiment by steadily increasing the Cu input solution flow rate (gray line). **(B)** Clusters of Cu^0 observed throughout the FTC at the termination of the experiment upon disassembly for sample preservation.

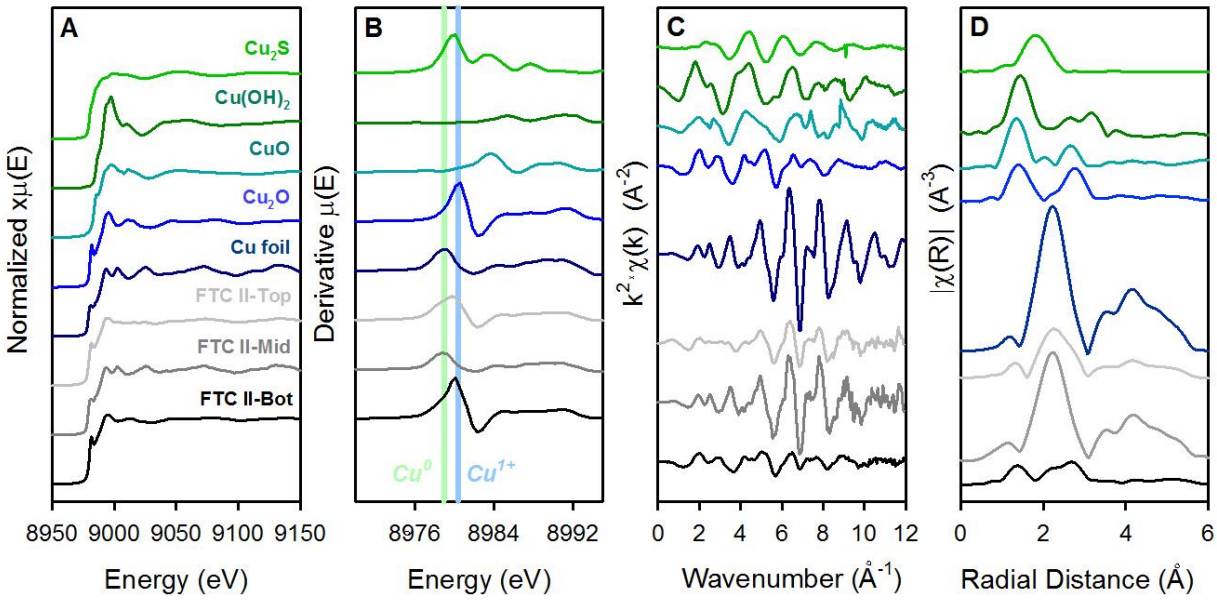

Figure 2.4 Normalized Cu XANES K-edge spectra from APS beamline 20-BM for five Cu standards and bulk samples from three Cu FTC II locations (top, middle, and bottom). (**A**) Adsorption edge μ(E) spectra. **(B)** First derivative μ(E) Cu spectra. Light green and blue vertical bars indicate K-edge energies for Cu^0 (left) and Cu^{1+} (right). **(C)** Cu spectra in k-space ($k^2 \bullet \chi(k)$). **(D)** Cu spectra in R-space $|\chi(R)|$.

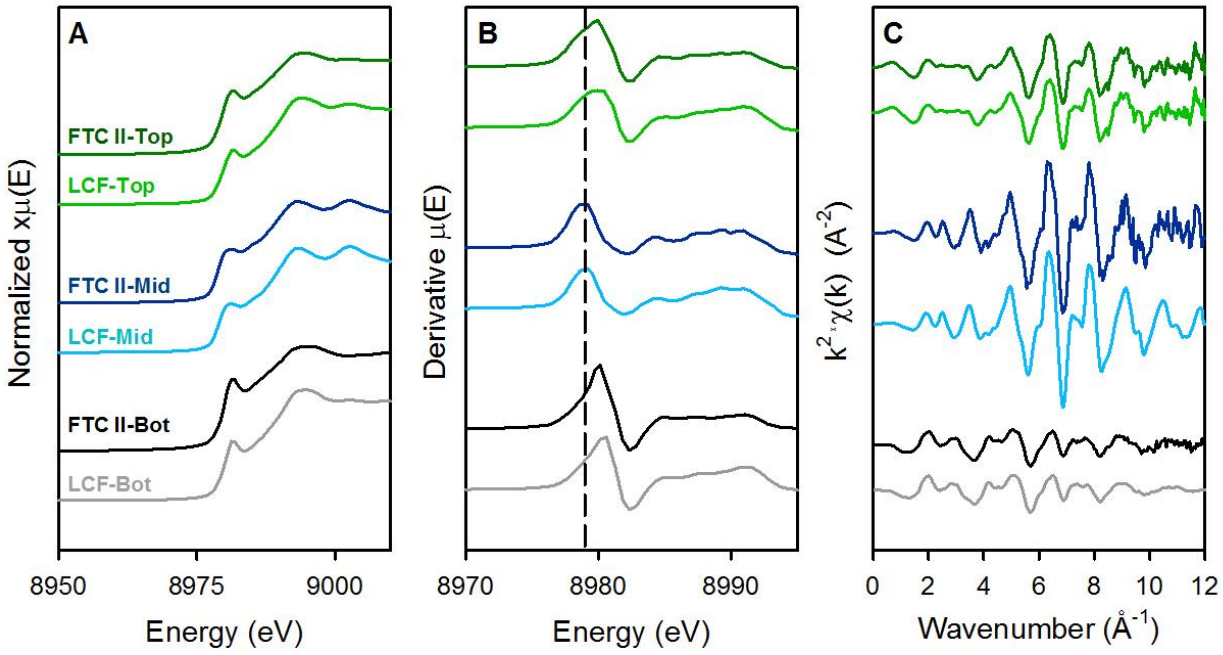

Figure 2.5 Normalized Cu XANES K-edge spectra from APS beamline 20-BM for five Cu standards and Cu FTC II samples at three different locations (top, middle, and bottom). (**A**) Adsorption edge μ(E) spectra. **(B)** First derivative μ(E) spectra. Light green and blue vertical bars indicate K-edge energies for Cu^0 (left) and Cu^{1+} (right). **(C)** Cu spectra in k-space ($k^2 \bullet \chi(k)$). **(D)** Cu spectra in R-space $|\chi(R)|$.

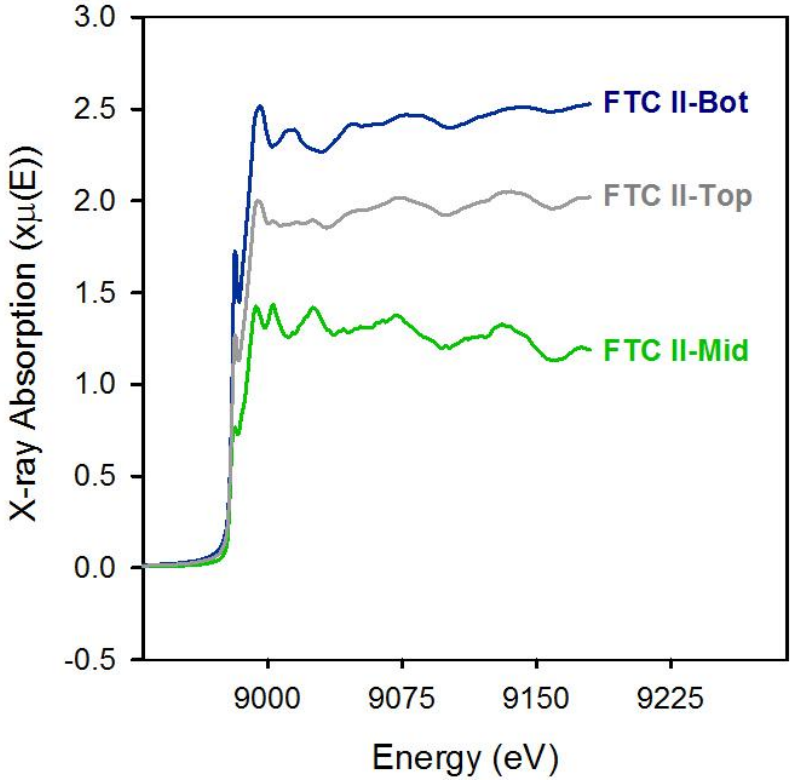

Figure 2.6 X-ray absorption (μ(E)) Cu XANES spectra (not normalized) collected at bottom, middle, and top positions of FTC II after termination of the laboratory flow-through experiment.

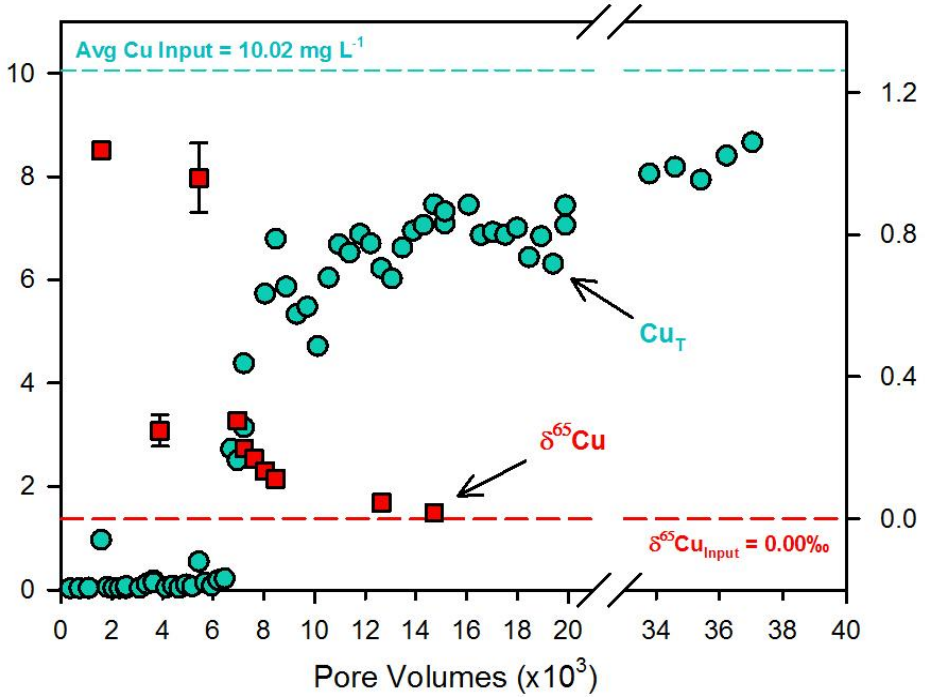

Figure 2.7 Cu concentrations (mg L^{-1}) and Cu isotope fractionation ($\delta^{65}Cu$ normalized to input values; $\delta^{65}Cu_{input}$ = 0.00 ‰) as they change with PVs in two stepped flow rate Cu FTC experiments for which isotope data was collected on FTC effluent samples. Horizontal dashed lines indicate the Cu concentration and $\delta^{65}Cu$ isotope values for input solutions.

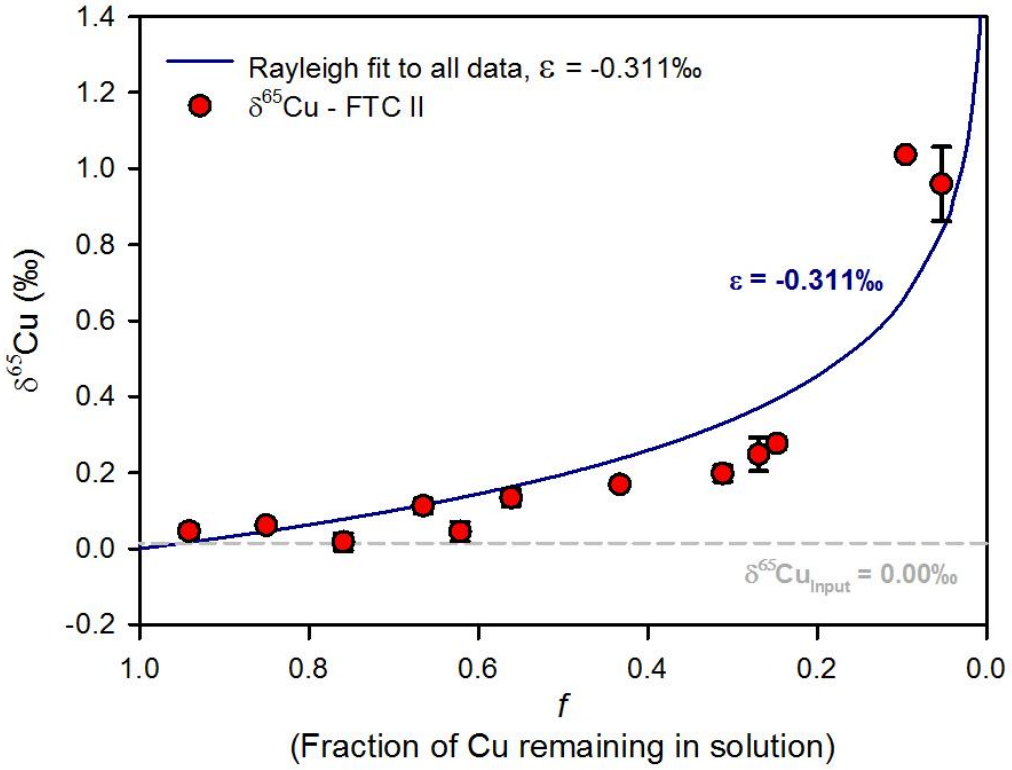

Figure 2.8 δ^{65}Cu versus *f* curve for Cu FTC II data. Data were normalized by recalculating δ^{65}Cu values relative to the isotope value of the input for respective experiments ($\delta^{65}Cu_{input}$ = 0.00 ‰) to enable straightforward comparison between input and effluent values. A Rayleigh curve fit to this data produced an ε = -0.31 ‰.

Chapter 3: Zinc immobilization and isotope fractionation during zero-valent iron flow-through cell experiments

3.1 Summary

Metal isotope measurements have emerged as a novel geochemical tool for tracing metal contamination in the environment in the past two decades. The use of permeable reactive barriers (PRBs) for removal of inorganic (*e.g.* Zn) and organic contaminants from groundwater has been extensively studied. Zinc behaviour in PRBs may be better understood by measuring isotope fractionation associated with immobilization in these remediation systems. The goal of this study is to quantify isotope fractionation occurring during Zn partitioning from the aqueous to solid phase during reactions with zero-valent iron (ZVI), a commonly used material in PRBs. Flow-through cell (FTC) laboratory experiments were carried out until Zn breakthrough occurred, enabling measurements of isotope fractionation over a broad range of relative Zn concentrations. The first measured effluent $\delta^{66/64}$Zn value shifted -0.40 ‰ relative to the Zn input solution. Zn isotope values spanned an *f* range (the fraction of Zn in solution) of 0.71 and revealed greatest depletion in the heavy isotope, ^{66}Zn, at early time when Zn removal was greatest. The δ^{66}Zn isotope dataset was best characterized by a Rayleigh curve with a fractionation factor (reported as ε) of 0.32 ‰. Bulk geochemistry and X-ray absorption near-edge structure (XANES) spectroscopic analyses indicate removal of Zn occurred through adsorption onto ZVI and precipitation of Zn (hydr)oxides. Specific periods of adsorption and precipitation controlling Zn removal could not be resolved; however, the total change in Δ^{66}Zn isotope ratios of 0.40 ‰ from early to late time is likely influenced simultaneously by effects of these two immobilization processes. Employing aqueous isotope analyses at sites with Zn-contaminated groundwater may

be beneficial to understanding Zn immobilization in remediation systems and Zn attenuation throughout the environment.

3.2 Introduction

Zinc is a transition metal element primarily occurring in the natural environment in the minerals sphalerite (ZnS) and smithsonite $Zn(CO)_3$) (Cloquet et al., 2008). The requirement for Zn in many regulatory proteins and participation of Zn in a wide array of enzymatic functions makes it an essential micronutrient vital for most living organisms (Cloquet et al., 2008). Industrial uses for Zn include electroplating, metal alloys, paint pigments, fertilizers and pesticides, and galvanizing roofing materials (Bullen, 2014). Mining, smelting and processing of Zn ore concentrates, and disposal of waste rock and mill tailings associated with Zn mining can result in the release of Zn, which can impact the surrounding environment through atmospheric pollution, surface runoff, and acid mine drainage (Bigalke et al., 2010; Matthies et al., 2014; Moncur et al., 2005; Pugh et al., 2002). Acid mine drainage produced from mining activities can adversely alter the geochemistry of surface and groundwater, causing additional impacts to the surrounding environment (Benner et al., 1997; Blowes et al., 2013; Forghani et al., 2015). Although Zn is ubiquitous in soil, sediments, and aquatic environments (Pokrovsky et al., 2005), release to the environment through industrial processes or mining may elevate Zn to concentrations detrimental to human and ecosystem health.

Permeable reactive barriers (PRBs) have been installed in aquifers to immobilize metals, such as Zn, and prevent the transport of dissolved contaminants in groundwater flow systems (Benner et al., 1997; Blowes et al., 1997; Ludwig et al., 2002; Puls et al., 1999). Zero-valent iron (ZVI), a commercially-available byproduct of steel processing, can effectively stabilize metals in PRBs through reduction, sorption, and precipitation reactions (Blowes et al., 1997; Jamieson-

Hanes et al., 2014; Lindsay et al., Ptacek, Blowes, and Gould, 2008; Rangsivek, 2010). Zinc exists in one oxidation state (Zn^{2+}) in the environment, therefore immobilization of Zn by ZVI is constrained to mechanisms involving adsorption of Zn to Fe (oxy)hydroxides at the ZVI surface, or precipitation of Zn (hydr)oxides, sulfides and carbonates, depending on site geochemistry (Blowes et al., 2000; Furukawa et al., 2002; Herbert, 2003; Li and Zhang, 2007; Rangsivek, 2010).

Stable metal isotope ratios are being used increasingly as a tracer of biogeochemical reactions influencing Zn transport in the environment (Aranda et al., 2012; Bigalke et al., 2010; Chen et al., 2008; Matthies et al., 2014; Pokrovsky et al., 2005; Shiel et al., 2010; Veeramani et al., 2015). Five stable isotopes of Zn are present naturally in the environment; ^{64}Zn, ^{66}Zn, ^{67}Zn, ^{68}Zn, and ^{70}Zn. The most common Zn isotopes are ^{64}Zn and ^{66}Zn, with abundances of 49.1% and 27.7% respectively (Meija et al., 2016). The ratio of $^{66/64}Zn$ is commonly reported for Zn isotope fractionation. Zn isotopes may be indicators of environmental processes as reactions partitioning Zn preferentially incorporate heavy or light isotopes. The majority of research on Zn isotope fractionation during Zn attenuation focuses on Zn removal under static conditions (Aranda et al., 2012; Balistrieri et al., 2008; Borrok et al., 2009; Borrok et al., 2008; Juillot et al., 2008; Pokrovsky et al., 2005; Veeramani et al., 2015), and has recently been extended to controlled saturated flow experiments (Jamieson-Hanes et al., 2017). Changes in the chemical coordination of Zn in the aqueous versus solid phase are important factors affecting Zn fractionation, as heavy isotopes tend to accumulate in the solid phase (Albarède, 2004; Balistrieri et al., 2008; Juillot et al., 2008; Veeramani et al., 2015).

In this study, Zn fractionation was assessed with a flow-through cell (FTC), conducted in an anaerobic glovebox, to assess Zn removal processes that could be expected in a ZVI PRB.

Aqueous bulk geochemical measurements were supplemented with synchrotron-based X-ray absorption near-edge structure (XANES) spectroscopy to determine the solid Zn phases in the FTC. Zinc isotope measurements were conducted to evaluate the extent of fractionation associated with Zn removal under saturated flow conditions. Determining the degree of fractionation may enhance the application of Zn isotopes as a diagnostic geochemical tool for tracing Zn attenuation mechanisms and transport in the environment. The results of this experiment may also be useful for distinguishing abiotic Zn removal mechanisms from microbially-mediated causes of Zn fractionation in field applications.

3.3 Methods

3.3.1 Zn Flow-through Cell Experiment

A series of FTC experiments were performed to assess Zn breakthrough upon interaction with ZVI. The second rendition of the experiment (FTC II) was sampled longer and more frequently than FTC I. For better characterization of isotope and aqueous geochemistry trends, this chapter presents the results of FTC II. The experiment was conducted in an anaerobic glovebox (Coy Laboratories Products Inc., Grass Lake, MI) with an atmosphere of 3.5% H_2-balance N_2. The FTC was fabricated from high-density polyethylene (HDPE) with a 2.25 cm^3 central cavity (3 cm × 1.5 cm × 0.5 cm) to contain porous media. Influent and effluent ports (2 mm diameter) were installed at the bottom and top, and screened with 0.5 cm^2 pieces of Nitex® 210 µm mesh. The FTC was designed with an open face, which was covered with a transparent Kapton® film, and secured by an HDPE frame bolted to the main body of the FTC over an O-ring, sealing the contents from the glovebox atmosphere.

The FTC was packed with a 50% v/v ZVI-silica sand mixture weighing 8.4 g. The ZVI (Connelly-GPM Inc.; Chicago, IL) was washed three times with 1M HCl and rinsed with

ultrapure water (Milli-Q©) using a vacuum-filtration setup inside the glovebox. After air-drying, the ZVI was mixed with dry silica sand (U.S. Silica, Ottawa, IL) and manually packed into the FTC. A 500 mg L^{-1} stock solution made using $ZnSO_4 \cdot 7H_2O$ (Sigma-Aldrich Corp, Oakville, ON) in ultrapure water was used to prepare 4 L batch volumes of Zn input solution for the FTC.

Ten thousand pore volumes (PV) of Ar-purged ultrapure water were pumped through the FTC using an ISMATEC™ peristaltic pump over several weeks to condition the washed ZVI and remove superficial ferric oxide coatings (*e.g.*, Gui et al., 2009).

The FTC experiment was conducted by pumping the 5 mg L^{-1} Zn input solution through the FTC at a flow rate of 22 mL hr^{-1} for the duration of the experiment. The effluent valve at the top of the Zn FTC was connected to a Retreiver® 500 Teledyne ISCO fraction collector using 0.89 mm PharmMed tubing (ID Cole Parmer tubing). The fraction collector was used to automatically subdivide the effluent into 15 mL vials to produce a continuous sample array throughout the experiment.

3.3.2 Aqueous Sampling

The 15 mL samples collected in centrifuge tubes were acidified to pH <2 for preservation with high-purity concentrated HNO_3 for analysis of major and trace element concentrations, and Zn isotope ratio analysis. Every sixth vial of effluent from the fraction collector was left unacidified for anion analysis.

Apart from samples collected in the first 100 PVs (where the effluent concentration of Zn increased rapidly), sets of five acidified samples were combined to provide 75 mL volumes, which were divided for cation analysis and Zn isotope measurements. Dissolved constituents, including Zn and Fe, were determined using an inductively coupled plasma-optical emission spectrometer (ICP-OES; iCAP 6000; Thermo Scientific). Redox and pH microelectrodes (Flow

Thru Microelectrodes, Microelectrodes Inc., Bedford, NH, USA) were connected in series at the effluent end of the FTC to provide continuous measurements of the pH and Eh. A band-pass filter was applied to the microelectrode dataset to filter out 2σ outliers followed by a five-point boxcar smoothing technique.

3.3.3 Zn Isotope Measurements

Aqueous FTC samples for δ^{66}Zn measurement were selected to provide an evenly distributed range of Zn concentrations. These samples were purified in a clean laboratory by graduate students of the Groundwater Geochemistry and Remediation Group, Jeffrey Leon (author of this thesis) and Lingyi Kong (University of Waterloo), within a HEPA-filtered fume hood in preparation for isotope ratio measurement by multicollector-inductively coupled plasma-mass spectrometer (MC-ICP-MS; Thermo Scientific Neptune). The Zn purification method is based on the approach developed by Maréchal et al. (1999). Sample volumes containing precisely 10.08 µg of Zn were transferred to clean Savillex Teflon vials. Uniform volumes of Zn double-spike standards were added to each Teflon vial for normalization of sample isotope measurements and the IRMM-3702 Zn standard (measured separately). The Zn isotope ratios are reported as δ^{66}Zn, where

$$\delta^{66}Zn = \left[\frac{\left(\delta^{66}Zn/\delta^{64}Zn\right)_{sample}}{\left(\delta^{66}Zn/\delta^{64}Zn\right)_{IRMM-3702}} - 1 \right] \times 1000‰ \quad (3.1)$$

The Teflon vials were placed on a hot plate overnight to evaporate the sample to dryness. The remaining solid fraction was dissolved in 7 M HCl and evaporated twice, then dissolved once more in 7 M HCl and pipetted into 3 mL columns containing ~1.6 mL of AG-MP-1M anion exchange resin (100-200 mesh; BioRad®) enclosed by two 0.2 µm polyethylene frits. The 3 mL columns were placed on a glass manifold in a fume hood to enable diluted acids to be drawn

through the pre-washed resin by vacuum suction and into 50 mL centrifuge tubes. The resin was flushed by suction with 6 mL of 7M HCl, 12 mL of 2M HCl, 12 mL of 0.5M HNO_3, 10 mL of ultrapure water, and lastly 6 mL of 7M HCl to remove any impurities.

Samples were loaded individually onto the resin and extraneous cations and anions within the matrix were first eluted with 1 mL of 7M HCl. Copper was eluted with 30 mL of 7M HCl, followed by Fe removal from the matrix with 32 mL of 2M HCl. The Zn fraction was then eluted into new centrifuge tubes using 18 mL of 0.5 M HNO_3. This Zn volume was transferred to 30 mL Savillex Teflon vials, evaporated to dryness, and dissolved in 1 mL of 5 M HNO_3. These purified Zn samples were brought up to 10 mL with ultrapure Milli-Q water before isotope ratio determination on the MC-ICP-MS, performed by Julia Jamieson-Hanes, a research hydrogeochemist of the Groundwater Geochemistry and Remediation Group at the University of Waterloo.

A double-spike technique was employed for Zn isotope measurement because the element has five isotopes. The double-spike method accounts for instrumental mass-dependent isotope fractionation. This data reduction method includes a double-nested iterative routine to correct for mass bias. The mode for uncertainty of all Zn isotope measurements was ± 0.04 ‰, based on a 2σ outlier test from isotope fractionation values measured in triplicate.

3.3.4 XAS Data Collection and Processing

The Zn FTC II was disconnected from the pump, left intact, and transported to the Advanced Photon Source within two months of the end of the experiment (APS; Argonne National Lab, IL) for *in situ* solid phase characterization. The incident X-ray beam was directed through the Kapton® film window of the FTC. Zn K-edge XANES data was collected at the Sector 20-ID-C (insertion device) beamline at the APS. The Zn K-edge occurs at 9659 eV and

scans were collected over an energy range of 9500 to 9950 eV. Three XANES scans were collected at the top, middle, and bottom of the FTC, maintaining high Zn:Fe ratios to minimize interference of Fe with the Zn spectra. Athena, a component of the IFEFFIT XAS analysis software package (Ravel and Newville, 2005) was used to process XANES data. The scans at each position were merged in Athena prior to data processing to increase the signal-to-noise ratio. Spectra for Zn reference materials used in the XANES analysis included ZnO, $Zn(OH)_2$, Zn sorbed to ferrihydrite (Zn on Fh), and $ZnSO_4$.

The Zn XANES dataset was supplemented with more data from bulk samples in a subsequent APS trip to Sector 20-BM-B, which utilizes bending magnet (BM) technology. This trip occurred five months after the data analysis on the *in situ* FTC II at Sector 20-ID-C. In preparation for this beamtime, the FTC II was disassembled and solids were divided into top, middle, and bottom sections (~1 g each) in duplicate. These samples were prepared in an anaerobic chamber, flash-frozen in liquid nitrogen, and dried overnight on a benchtop freeze-drier to remove any moisture, thus minimizing risk of geochemical product alteration. The solids were transferred into an acrylic holder and contained by Kapton® tape. This holder was mounted on a sample stage at the APS to perform X-ray absorption fine structure (XAFS) measurements. The beamline at Sector 20-BM-B utilizes a Si(111) double-crystal monochromator, similar to the ID-C setup. This beamline propagates a beam with lower intensity over a larger greater area, which improves the data quality for the samples in this study. The Artemis and Athena programs of the IFEFFIT software package were employed for XANES data analysis of Zn spectra from both the ID and BM Sector 20 beamlines.

The PHREEQC geochemical modeling program and WATEQ4 database (Parkhurst, 1999) were used to determine if XANES data agreed with predictions of Zn precipitate formation

based on aqueous FTC geochemical data. Effluent pH, Eh, and cation measurements were used in the model calculations to determine the change in saturation indices (SI) of relevant minerals, including ZnO and $Zn(OH)_2$, throughout the FTC II experiment.

3.4 Results and Discussion

3.4.1 Aqueous Geochemistry and Zn Removal

Attenuation of Zn in the FTC II was evaluated through measurement of Zn concentrations over time (Figure 3.1). In the 50% v/v ZVI-silica sand FTC operated at ~22 mL hr^{-1}, Zn^{2+} was detected in the effluent shortly after introduction of the input solution (5.07 ± 0.21 mg L^{-1}; Figure 3.1A). Effluent Zn concentrations increased steadily from 0.01 to 4.48 mg L^{-1} through 1,500 PVs, before levelling off at 4.55 mg L^{-1} (0.91 ± 0.03 C/C_0) for the remainder of the experiment. The change in the rate of Zn loading onto ZVI at ~1,500 PVs signals the stabilization of the Zn effluent concentration (Figure 3.1B). The average cumulative Zn loading rate over the entire FTC II experiment (4,500 PV) was 1.15 mg_{Zn} g^{-1}_{ZVI}. A total mass of 6.80 mg of Zn was removed from solution during the experiment, corresponding to an average removal rate of 2.91×10^{-4} mg_{Zn} g_{ZVI}^{-1} PV^{-1}. Zn concentrations, pH, and Eh measurements for FTC I are reported in Appendix B for reference.

In addition to Zn, dissolved Fe and S were detected in the FTC effluent. Dissolved Fe in the input solution was below the analytical detection limit (<0.2 mg L^{-1}), indicating that dissolved Fe in the effluent was derived from oxidation of ZVI following the introduction of Zn to the FTC. In the FTC effluent, aqueous Fe was initially 4.45 mg L^{-1} and decreased to 1.06 ± 0.10 mg L^{-1} after 1000 PVs, mirroring the Zn^{2+} trend (Figure 3.1A). The input and effluent S concentrations were not significantly different, with average values of 2.30 ± 0.21 mg L^{-1} and

2.23 ± 0.18 mg L^{-1} respectively. The S concentrations decreased slightly at 1065 PVs, but were stable throughout the full FTC II experiment.

Prior to the addition of the Zn input solution to the FTC II, the pH of the effluent was 9.5 and the Eh was -400 mV (Figure S3.1). Basic pH values and reducing Eh conditions are expected for ultrapure water that has interacted with ZVI (Blowes et al., 2000; Furukawa et al., 2002; Gui et al., 2009; Powell et al., 1998). The pH and Eh of contaminated water in contact with ZVI is subject to change depending on the removal reactions involved for various contaminants. After Zn was introduced to the FTC, the pH declined to ~8 (Figure 3.1C). The FTC II Eh conditions began at -400 mV and remained reducing throughout the experiment, rising to -200 mV around 1,500 PVs, and stabilizing at -275 mV by the end of the sampling period. The largest Eh shift occurred at ~1,500 PVs, coinciding with the stabilization of the cumulative Zn loading rate.

The FTC II experiment was conducted in a glovebox where an anoxic environment was maintained and Zn input solutions were Ar-purged to reduce the influence of O_2 on Zn attenuation reactions in the FTC. In ZVI PRB systems, O_2 is rapidly consumed at the upgradient face of ZVI barriers as in equations 3.2 and 3.3 (Furukawa et al., 2002; Herbert, 2003), where goethite, α-$FeOOH_{(s)}$, one of the most stable Fe (oxy)hydroxides at low temperatures (Blowes et al., 2013), represents one of many Fe (oxy)hydroxide phases which can form on the ZVI surface.

$$Fe^0_{(s)} + 0.5O_2 + 2H^+ \rightarrow Fe^{2+} + H_2O \quad (3.2)$$

$$Fe^0_{(s)} + 0.75O_2 + 0.5H_2O \rightarrow \alpha\text{-}FeOOH_{(s)} \quad (3.3)$$

Under anoxic conditions, H_2O is reduced at the ZVI surface in the process of Fe corrosion:

$$Fe^0(s) + 2H_2O \rightarrow Fe^{2+} + H_2(g) + 2OH^- \quad (3.4)$$

This reaction (Eq. 3.4) is the primary driver of basic pH values, reducing Eh conditions, and high $Fe^{2+}_{(aq)}$ observed in the initial Zn effluent samples. Ferrous iron and hydroxide ions

have the potential to form $Fe(OH)_2$ (Eq. 3.5), a metastable Fe oxide which transforms to magnetite under conditions which are thermodynamically favourable (Odziemkowski et al., 1998) as per Eq. 3.6.

$$Fe^{2+} + 2OH^- \rightarrow Fe(OH)_{2(s)} \quad (3.5)$$

$$3Fe(OH)_2 \rightarrow Fe_3O_4 + H_2 + 2H_2O \quad (3.6)$$

The effluent was consistently within the basic pH range commonly reported for precipitation of Zn (hydr)oxides (pH 7.5-10; Herbert, 2003; Rangsivek, 2010; Roberts et al., 2003) and Zn adsorption to Fe (oxy)hydroxides (pH 6-8; Herbert, 2003; Juillot et al., 2011; Li and Zhang, 2007; Rangsivek and Jekel, 2005; Roberts et al., 2003).

The standard electrode potentials (E^0) of aqueous metal ions can be compared to E^0 for ZVI to infer geochemical removal mechanisms facilitated by ZVI (Li and Zhang, 2007). For reduction of metal ions in solution by ZVI, the energy gradient of electrons from the ZVI core to the target element must decrease. Electron transfer from ZVI to Zn is thermodynamically improbable because E^0 for Zn^{2+} at room temperature (-0.76V for Zn^{2+}/Zn^0; pH 7) is lower than the energy of electrons in the Fe^{2+}/Fe^0 couple (-0.44 V; Rangsivek, 2010), thus the thermodynamic conditions do not favour Zn^{2+} reduction. This condition suggests that the reduction of H_2O (Eq. 3.4), and formation of Fe (oxy)hydroxides on the surface of ZVI was sustained by the interaction between the input solution and ZVI throughout the experiment. In high pH-low Eh systems, hematite and maghemite are not thermodynamically stable, indicating that magnetite derived from ferrous hydroxide release is an important solid-phase product on ZVI (Herbert, 2003; Odziemkowski et al., 1998) during corrosion in this anaerobic system. The continual corrosion process of commercially-produced ZVI is well suited for metal adsorption (Blowes et al., 1997; Rangsivek and Jekel, 2005; Wilkin and McNeil, 2003). Steady pH and Eh

values suggest a dominant geochemical attenuation mechanism, likely a combination of adsorption and precipitation reactions.

Less Zn was removed from the aqueous phase over time with progressive breakthrough. The trend in dissolved Fe measurements proceeded inversely to the trend in Zn concentrations, suggesting that the geochemical reactions controlling concentrations of these two transition metals are linked. Effluent concentrations of Fe level off around 1 mg L^{-1} after 1,000 PVs because of a declining rate of ZVI corrosion. Unchanging concentrations of S over time indicate that it was conserved throughout the FTC experiment and did not affect the removal of Zn. The decreasing availability of surface sites for Zn adsorption and precipitation and exhaustion of unreacted ZVI surface sites due to ZVI corrosion and Fe (oxy)hydroxide formation are important contributors to the trends in dissolved Zn and Fe concentrations (Blowes et al., 1997; Furukawa et al., 2002; Li and Zhang, 2007). The accumulation of surface coatings and the formation of Zn (hydr)oxides reduces the amount of surface sites on the ZVI, leading to an increase in dissolved Zn^{2+} concentrations. The mass balance of Fe and Zn concentrations (Table S3.1) shows they are of the same magnitude (1.61×10^{-4} mol Fe and 1.04×10^{-4} mol Zn). There are a variety of individual pathways that may retain $Fe^{2+/3+}$ in ZVI surface coatings and Zn within (hydr)oxides, which may account for the discrepancy between the mass of Fe and Zn in the effluent.

3.4.2 Zn XANES and Potential Attenuation Mechanisms

The solid Zn phases present in FTC II were characterized through collection of XANES spectra (at a Sector 20 insertion device beamline) on the intact FTC II samples (FTC II-Top, -Mid, and -Bot; spectra from top, middle, and bottom locations of the FTC II respectively) and subsequent linear combination fitting (LCF) analysis. FTC II was later disassembled and bulk samples were preserved for collection of additional XANES spectra. Zinc precipitates and

adsorbed phases expected in a ZVI system with Zn-spiked ultrapure water include Zn on Fh, ZnO, and $Zn(OH)_2$ (Figure 3.2). Elemental Zn is also displayed to illustrate the location of the Zn *K*-edge at 9659 eV, and is important because this spectra was used to calibrate standards and samples collected at different times by applying an energy shift. The main absorption edges in Zn samples and standards align closely when plotted in normalized μ(E) space (Figure 3.2A). The pre-edge shoulder unique to the Zn^0 spectra distinguish it from the other spectra. The differences in absorption peak energies are discernible in the plots of the first derivative of μ(E) (Figure 3.2B). Spectra plotted in *k*-space and *R*-space (Figure 3.2C and 2D respectively) present the XANES spectra using mathematical transforms that illustrate waveforms as a function of wavenumber (*k*-space) and radial distance (*R*-space). These spectra also illustrate the variation between Zn^0 from the Zn^{2+} standards. The adsorption edge of all sample spectra peaks lies between 9666 - 9668 eV, consistent with the three Zn^{2+} reference materials.

The FTC II-Bot_BM, FTC II-Mid, and FTC II-Top normalized spectra all have similar features around the main adsorption peak, whereas the FTC II-Bot spectra lacks the small post-edge hump around 9680 eV observed in the other three sample spectra (Figure 3.2A). Qualitative differences between these sample spectra also appear in *k*-space, where FTC II-Bot spectra fluctuates least at the lower range in wavenumber and the main middle peak is closer to 4 $Å^{-1}$ relative to the other samples (Figure 3.5C). The FTC II-Bot observations are consistent with the smooth spectra at lower wavenumbers and right-skewed central peak of the Zn on Fh standard spectra in *k*-space. The FTC II-Bot_BM, FTC II-Mid, and FTC II-Top spectra all have individual features that can visually be traced to peaks of varying magnitudes seen for ZnO and $Zn(OH)_2$ reference materials in each space plotted (Figure 3.2).

Results of LCF suggest the following standards contributed most to the modelled spectra for each sample; Zn on Fh to FTC II-Bot, $Zn(OH)_2$ and ZnO for FTC II-Mid, ZnO for FTC II-Top, and ZnO for FTC II-Bot_BM. In all four fitting procedures, $Zn(OH)_2$ was important for modelling the sample composition (Table 3.1). The R-factors computed by Athena (Table S1) indicate the relative variance between samples and a fit composed of select standards, where a lowest possible value is optimal. The R-factors for LCF spectra are relatively low at 0.007, 0.010, and 0.022 for FTC II-Bot spectra, FTC II-Mid, and FTC-Top respectively, providing confidence in the interpretation of suggested species present. The XANES spectra plotted without normalization indicate similar amounts of Zn species at the top and bottom locations of FTC II (Figure 3.4). In comparison, the more prominent signal of the FTC II-Mid spectra suggests that Zn (hydr)oxide likely concentrated in the center of the FTC.

PHREEQC modeling indicated the potential for saturation of ZnO and $Zn(OH)_2$ in the FTC effluent. Saturation indices from the PHREEQC report were plotted (Figure 3.7) for ϵ-$Zn(OH)_2$, the most stable polymorphic compound of $Zn(OH)_2$, and zincite (ZnO) which is slightly more stable than the Zn hydroxides at 25^{o}C (Oswald and Asper, 1977). The formation of these solid phases became thermodynamically favourable after 250 PV, when dissolved Zn reached 1.27 mg L^{-1}. After 250 PV, the modeling results showed supersaturaton of ZnO for the remainder of the experiment (mean SI_{ZnO} = 0.28), excluding two periods of brief, unexpected pH decreases at approximately 800 PV and 2000 PV. The simulated effluent remained near saturation with respect to $Zn(OH)_2$, which was consistently less than the SI of ZnO by 0.36 units. The saturation index of ZnO exceeds $Zn(OH)_2$. The LCF results (Table 3.1) indicate greater contributions of ZnO versus $Zn(OH)_2$ in the three sample spectra where LCF fits were only

influenced by precipitated phases (*e.g.* FTC II-Mid, FTC II-Top, and FTC II-Bot_BM LCF results).

Examination of the structural coordination of aqueous Zn versus precipitated Zn and sorbed Zn associated with Fe (oxy)hydroxides is useful to build upon the XANES observations and LCF results of this study. Aqueous-to-solid partitioning in this study is likely accompanied by a moderate decrease in Zn—O bond lengths and coordination number (CN) as Zn is removed by ZVI. With few exceptions, aqueous Zn^{2+} is reported consistently in the literature to form octahedral complexes in aqueous solution (Balistrieri et al., 2008; Juillot et al., 2008; Kuzmin et al., 1997; Trivedi et al., 2001; Waychunas et al., 2002). An EXAFS study found the Zn—O interatomic distance in a $ZnSO_4 \cdot 7\ H_2O$ solution to be 2.06 Å. This bond length is slightly less than the distance of 2.08 to 2.11 Å for Zn—O in dilute chloride solutions (Waychunas et al., 2002), where the coordination number (CN) = 6-7 for $Zn^{2+}_{(aq)}$ at near-neutral pH. Trivedi et al. (2001) determined the Zn—O bond distance in a $Zn(NO_3)_2$ solution is ~2.18 Å. Zinc oxide was a necessary component in most LCF sample spectra in abundances greater than 50%. First shell coordination XAS studies have measured Zn—O bond lengths of 1.96-1.99 Å, where CN = 4 (Elzinga and Reeder, 2002; O'Day et al., 1998). Waychunas et al.(2002) indicate the Zn—O bond length = 1.96 Å for ϵ-$Zn(OH)_2$, which is equal to the average of the four Zn—OH bond lengths (ranging from 1.89-2.03 Å) reported by O'Day et al. (1998). The Zn—O bonding in γ-$Zn(OH)_2$ is comparable, confined to a smaller range of 1.94-1.98 Å (O'Day et al., 1998). These values all suggest that both the interatomic bond distance and the CN decreased during Zn removal by precipitates induced by interactions with ZVI in FTC II.

The FTC II-Bot spectra was also strongly influenced by Zn adsorbed to Fh in the LCF procedure (Table 3.1), indicating a potential Zn removal process that would also likely cause a

reduction in Zn bond lengths. Ferrihydrite is a poorly crystalline iron oxyhydroxide considered to be a mixture of compounds as it can come in many structural varieties, such as the two-line and six-line forms (Blowes et al., 2013). Although the presence of ferrihydrite was not specifically confirmed, the LCF results suggest Zn existed in a chemical coordination consistent with Zn sorbed on Fe (oxy)hydroxides which have been previously observed to form around the core of ZVI grains in numerous laboratory studies (Furukawa et al., 2002; Herbert, 2003; Jamieson-Hanes et al., 2014; Lindsay et al., 2008). In a study of Zn adsorption to goethite and corundum, Zn^{2+} underwent a change in CN of six as $Zn(H_2O)^{2+}_{(aq)}$ to four on the mineral surface, in the form of $Zn(O, H_2O)_4^{2+}{}_{(s)}$ (Pokrovsky et al., 2005). Two studies determined Zn—O bond distances of 1.96 to 1.97 Å for Zn adsorbed to two-line ferrihydrite in tetrahedral coordination (Juillot et al., 2008; Waychunas et al., 2002). At pH 7.5, Zn is found to be tetrahedrally coordinated with amorphous $Zn(OH)_2$ (Roberts et al., 2003). These sources suggest a potential change in coordination number of Zn in this study as it partitioned via sorption to the solid phase.

3.4.3 Zn Isotope Fractionation

The $\delta^{66}Zn$ for the influent solution for FTC II was -0.18 ± 0.04 ‰ relative to IRMM 3702. For ease of interpretation, the FTC II data was normalized relative to the input solution, which acquires a value of $\delta^{66}Zn$ = 0.00 ± 0.04 ‰ (Figure 3.6). In FTC II, sufficient mass of Zn was available for $\delta^{66}Zn$ measurements at 250 PVs, when $\delta^{66}Zn$ was -0.40 ± 0.03 ‰, and increased to -0.12 ± 0.04 ‰ by 1750 PVs. Most of the isotope analyses were made on samples from the first 1,000 PVs, when the greatest changes in C/C_0 and *f* occurred. The fluctuations in $\delta^{66}Zn$ values after 1,000 PVs were within the range of analytical error in the FTC II experiment (Figure 3.5).

Isotope measurements were interpreted based on Rayleigh distillation isotope theory, where the δ^{66}Zn of a sample (R) divided by δ^{66}Zn of the initial solution (R_0) is equal to the fraction of Zn in solution (f) raised to the fractionation factor (α) minus one, as per the equation:

$$\frac{R}{R_0} = f^{(a-1)} \tag{3.7}$$

A Rayleigh curve was fit to all δ^{66}Zn measurements from FTC II to determine a fractionation value (Eq. 3.9) characteristic of the geochemical reactions involved in removing Zn under saturated flow conditions (Figure 3.6A). A value of $\varepsilon = 0.32$ ‰ was obtained for this fit with a corresponding $R^2 = 0.76$.

$$\alpha = \mathrm{R}_{\mathrm{product}}/\mathrm{R}_{\mathrm{reactant}} \tag{3.8}$$

$$\varepsilon = (\alpha - 1) \times 1000‰ \tag{3.9}$$

After Zn reached a C/C_0 of approximately 0.8, the extent of Zn removal slowed, followed by a shift in the degree of isotope fractionation, likely representing a change in the relative contributions of adsorption and precipitation to the immobilization of Zn (Figure 3.6B). The primary cause for this change in ε values is most likely the lack of available surface sites and ZVI corrosion products which limited uptake of dissolved Zn^{2+} later in the experiment. Zinc may also retain its hydration shell during sorption to hydrous ferrous oxide (Trivedi et al., 2001). In this instance, Zn does not change coordination number, and attenuation by this pathway is less likely to induce fractionation. Veeramani et al. (2015) suggest the absence of a change in coordination as a potential influence on the lack of fractionation observed during Zn sorption onto ferrihydrite. As ZVI corrosion products become less effective at removing Zn in this study, the dominant process of Zn removal shifts to precipitation of ZnO and $Zn(OH)_2$, which causes a change in the coordination of Zn, resulting in greater fractionation. The greater contribution of

Zn (hydr)oxides to the LCF process (compared to adsorbed Zn standards) is also consistent with the hypothesis that Zn fractionation was largely influenced by precipitation processes.

Heavier Zn isotopes tend to accumulate in the solid phase where sorption and precipitation favour stronger Zn bonding (Balistrieri et al., 2008; Juillot et al., 2008; Little et al., 2014; Schauble, 2004), reflected by predominantly negative aqueous δ^{66}Zn values in the literature (Table 3.2). In this study, the maximum δ^{66}Zn offset in the FTC II effluent, -0.4 ‰ relative to the input solution, is in agreement with the accumulation of heavy isotopes in the solid phase. PHREEQC calculations indicated that the effluent water was undersaturated with respect to $Zn(OH)_2$ and ZnO at the beginning of the experiment from 0 to 250 PV suggesting the formation of $Zn(OH)_2$ and ZnO during this time was not thermodynamically favoured and it is unlikely that these phases accumulated in the FTC. Over this initial interval the removal of Zn likely occurred through adsorption onto Fe (oxy)hydroxides accumulated on the ZVI. At this time, the Rayleigh curve exponentially decreases below the range of δ^{66}Zn measurements (Figure 3.6). The effluent water became oversaturated with respect to both $Zn(OH)_2$ and ZnO after the first 375 PVs (Figure 3.7) suggesting the Zn isotope fractionation in this interval is likely influenced by the precipitation of Zn (hydr)oxides. The LCF analysis of the XANES spectra of material in the FTC II is consistent with the occurrence of these phases. The geochemical simulations assume thermodynamic equilibrium, and provide no indication of the reaction rates at which saturated species form. The calculated SI of the Zn (hydr)oxides rise with increasing dissolved Zn concentrations up to ~750 PVs, which coincides with the period extending up to f = 0.6, when Zn uptake is most rapid (Figure 3.6B), and δ^{66}Zn increased 0.23 ‰ (from 250-750 PVs). For most of the experiment thereafter, the PHREEQC calculations indicate supersaturation with respect to ZnO. Zinc oxide is the least soluble Zn precipitate expected in the FTC, which

aligns with the LCF results showing it formed in greater abundances relative to $Zn(OH)_2$ (Table 3.1). The effluent remained near saturation (SI = 0) in regards to ϵ-$Zn(OH)_2$. As Zn concentrations stabilized at higher *f* values and the Rayleigh curve overestimated the isotope data, SI of the solid species did not significantly fluctuate. These SI trends suggest consistency in the Zn removal mechanism for the full experiment, inclusive of both low and high *f* regions of isotope characterization. Adsorption of Zn, shown by XANES fitting results to have a minor impact in Zn removal (Table 3.1; Figures 3.3, 3.4), which is consistent with the brief period of Zn removal while the water remained undersaturated with respect to $Zn(OH)_2$.

The isotope analysis of this study demonstrated the magnitude of the δ^{66}Zn shift (-0.4 ‰) associated with Zn removal in a ZVI system under flowing conditions. The solid phase data accumulated from XANES and PHREEQC modeling were crucial for interpreting Zn phases, which provide insight on expected changes in aqueous and solid Zn bonding environments. The results suggest as the Zn concentration increased, the effluent water became supersaturated with respect to $Zn(OH)_2$, and precipitation of Zn (hydr)oxides predominated over adsorption after 250 PVs when the geochemical conditions for precipitates became thermodynamically favourable. Solid phase characterization indicates significant contributions of Zn (hydr)oxide formation throughout the FTC. Both processes are important in Zn remediation, and their combined effect produces a significant degree of fractionation in ZVI treatment systems.

3.4.4 Implications for Groundwater Management

The use of Zn isotope ratios in groundwater monitoring programs requires an understanding of how Zn fractionates under a variety of environmental conditions. Zinc isotope ratio measurements can best be applied to PRBs where ZVI is used for Zn remediation in an anaerobic setting with reducing Eh and basic pH of ~8. One can expect a contaminated field site

to be more geochemically complex, potentially involving a variety of additional mineral phases and microbial activity that may influence the groundwater flowing into a PRB. This study provides a benchmark for the inorganic removal of Zn through precipitation of Zn (hydr)oxides and adsorption onto ZVI corrosion products. The overall fractionation values calculated for the combination of these attenuation processes, particularly for the lower *f* region, can be used in conjunction with other Zn isotope studies.

The results of this investigation suggest that Zn isotope measurements have potential application in distinguishing mechanisms of Zn removal reactions from other pathways. A variation between this study and the one by Jamieson-Hanes et al. (2017) assessing ZnS precipitation in a FTC was the direction of fractionation (enrichment versus depletion). The removal mechanism in effect here caused the heavier ^{66}Zn isotope to be enriched in the solid phase upon anaerobic precipitation of Zn (hydr)oxides and adsorption, whereas ZnS precipitation led to an enrichment of the heavy isotope in the aqueous phase. Despite only having one redox state, Zn may undergo varying degrees of fractionation depending on its complexation with including sulfur and organic matter, due to their redox-sensitivity (Jamieson-Hanes et al., 2017; Albarède, 2004; Bullen, 2014). Consequently, Zn isotopes may have applications as an indicator of the predominant reactions. This application offers context for the fractionation observed in this study, which provides the expected δ^{66}Zn shift under consistently reducing conditions.

In addition to being an indicator of potential geochemical mechanisms and conditions, the knowledge gained from this study may help in estimate the long-term capacity for Zn uptake in a PRB. If isotope measurements in a ZVI PRB are more negative than the influent source entering the barrier, this observation could indicate that Zn precipitation and adsorption are effectively facilitating Zn removal. If aqueous δ^{66}Zn measurements approach the initial value of

contaminated groundwater prior to treatment, Zn and Fe (oxy)hydroxides may be diminishing the effectiveness of the ZVI treatment system. Metal isotope ratios may assist in differentiating natural Zn processes from anthropogenic sources, as Zn fractionates during weathering and transport throughout the environment (Bigalke et al., 2010). Determining the fractionation derived from geochemical reactions within a ZVI barrier is essential for understanding how Zn fractionates in various environmental reservoirs during transport from its original source.

The majority of Zn isotope studies assess fractionation on the basis of $\Delta^{66}Zn_{soln\text{-}solid}$, which is useful for determining the actual difference in $\delta^{66}Zn$ values between phases, but may be less practical in PRB field studies assessing contaminated groundwater. Attenuation in a ZVI barrier depends on reducing conditions; therefore, the *in situ* Zn isotope composition in the solid phase may be difficult to preserve because oxidation states may be compromised during the extraction and handling of cores. Aqueous isotope measurements may be more reliable and less costly within a geochemical sampling program, and add the advantage of revealing the geochemical nature of a system on a broader scale than solid-phase samples from discrete locations (Blowes, 2002). Isotope measurements coupled with traditional aqueous bulk geochemistry can provide valuable insight into the complex geochemical conditions controlling dissolved Zn concentrations in field investigations. If mineralogy data is also available, solid phase characterization such as XAS data can provide further support to explain isotope fractionation at a contaminated site.

Table 3.1 Weights given to standards during Linear combination fitting analysis of FTC II sample spectra in normalized u(E) space. In the Athena LCF exercise, weights of standards were not forced to sum to 1 during LCF. The fitting region of sample spectra included was -20 eV to 30 eV.

Sample	$Zn(OH)_2$	ZnO	Zn on Fh	R-factor
FTC II–Bot	0.36	-	0.62	0.007
FTC II-Mid	0.45	0.51	-	0.010
FTC II-Top	0.22	0.76	-	0.022
FTC II-Bot_BM	0.37	0.60	-	0.007

Table 3.2 Isotope fractionation in terms of $\delta^{66}Zn$ and ε attributed to Zn attenuation mechanisms

Reaction Type	**Solid phase surface/products**	**$\delta^{66}Zn$ Ratios** (‰) Aqueous range	**Associated Fractionation** $\Delta^{66}Zn_{soln\text{-}solid}$ (‰)	**ε** (‰)	**Reference**
Adsorption/ Precipitation	ZVI surface coatings	-0.59 to -0.19	-	0.31	This Study
Adsorption	Amorphous Fe(III) oxyhydroxides	-0.76 to -0.42	-0.52	-0.52	*1*
Adsorption	Goethite	-0.25 to -0.33	0.18 to 0.28	-	*2*
Adsorption, pH 8	Goethite Ferrihydrite	-0.55 -0.71	-0.29 -0.53	-	*3*
Adsorption	Fe-Mn crusts	-	-0.5	-	*4*
Adsorption	Biofilm sorption Biofilm uptake	-0.39 -0.76	-	-1.4 -0.4	*5*
Precipitation	Sphalerite Hydrozincite Hopeite	0.07 to 0.76 -0.45 to 0.0 -0.44 to 0.09	- - -	-0.30 0.18 0.25	*6*
Precipitation	Hydrozincite	-0.84 to -0.61	-0.35	-	*7*
Precipitation	Sphalerite	0.05 to 0.48	-	-0.27	*8*
Dissolution and desorption	Sulfidic mine waste; sphalerite dissolution	0.09 to 0.52	0.32 (pH <5) 0.23 (pH 6.1)	-	*9*
Oxidative weathering	Sulfide-rich rocks	-0.43 to 0.12	-	-	*10*

All $\delta^{66}Zn$ values reported relative to the IRMM-3702 international Zn isotope standard. Isotope fractionation between phases is reported throughout the literature as $\Delta^{66}Zn_{soln\text{-}solid}$, indicating the difference between aqueous versus solid $\delta^{66}Zn$ ratios. If necessary, $\Delta^{66}Zn_{soln\text{-}solid}$ ratios were corrected by subtracting the solid phase $\delta^{66}Zn$ isotope value from the aqueous isotope ratio for consistency.

References: *1*. Balistrieri et al. (2008), *2*. Pokrovsky et al. (2005), *3*. Juillot et al. (2008), *4*. Little et al. (2014), *5*. Coutaud et al. (2014), *6.* Veeramani et al. (2015), *7*. Wanty et al. (2013), *8*. Jamieson-Hanes et al. (Submitted 2016), *9*. Matthies et al. (2014), *10.* Borrok et al. (2009).

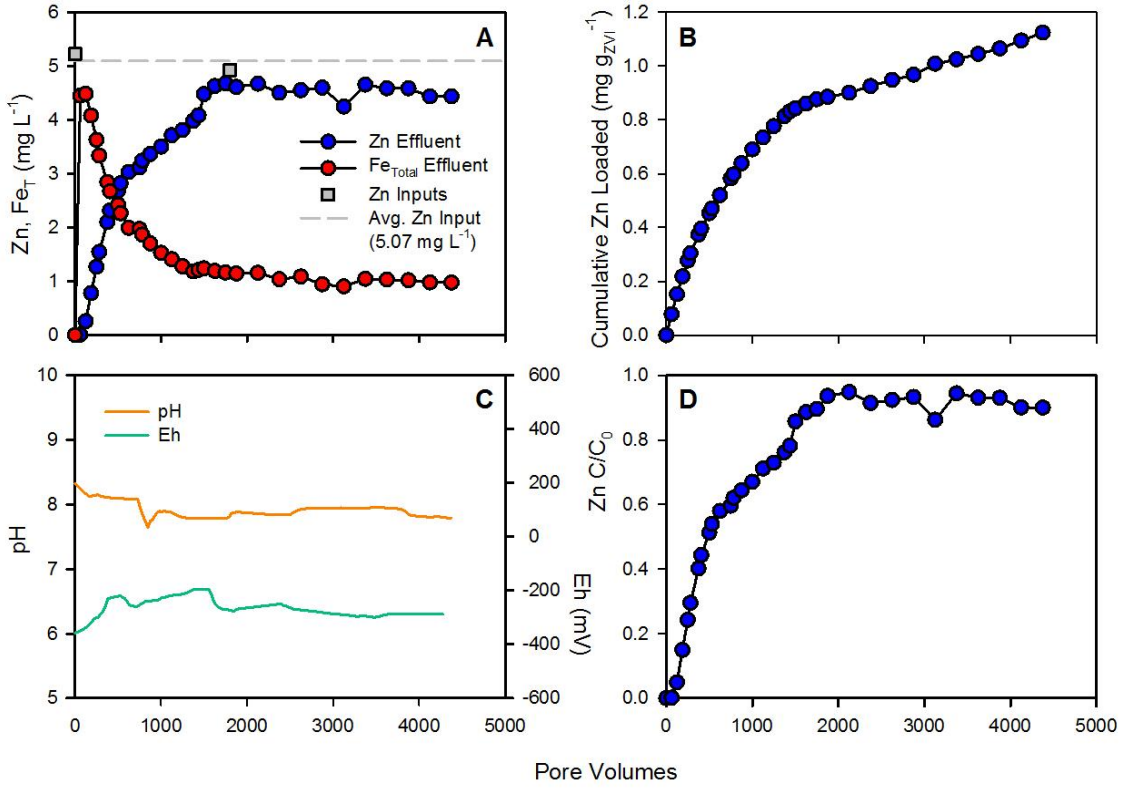

Figure 3.1 Bulk geochemistry for Zn breakthrough in the 50% v/v ZVI-silica sand FTC II. **(A)** Breakthrough curves for Zn (blue circles) and Fe_T (red circles) in effluent samples. **(B)** Mass of Zn cumulatively loaded onto ZVI (mg Zn per g ZVI) over the duration of the experiment. **(C)** Microelectrode pH and Eh trends based on measurements recorded hourly. Microelectrode data has been filtered to remove outliers and smoothed with a moving average technique. **(D)** Zinc breakthrough reported as effluent concentrations relative to the input concentration (C/C_0).

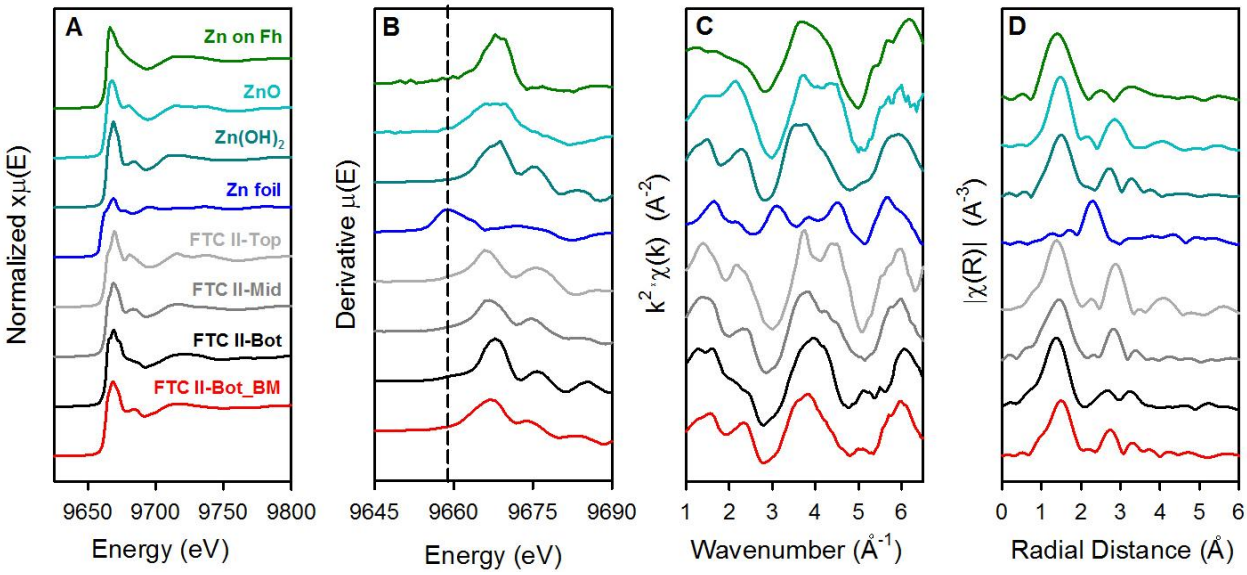

Figure 3.2 Zinc XANES K-edge spectra plotted in **(A)** normalized μ(E), **(B)** the first derivative of μ(E), where the absorption edge at 9659 eV is indicated with a dashed line, **(C)** k-space as k^2 χ(k), and **(D)** R-space as χ(R) space. The lower four spectra are scans from bottom, middle, and top positions of FTC II, including two locations near the bottom port collected at different APS Sector 20 beamlines (BM and ID). The four upper spectra are standard spectra of interest including Zn foil (Zn^0), Zn oxide (ZnO) and hydroxide [$Zn(OH)_2$] precipitates, and Zn sorbed to ferrihydrite (Zn on Fh).

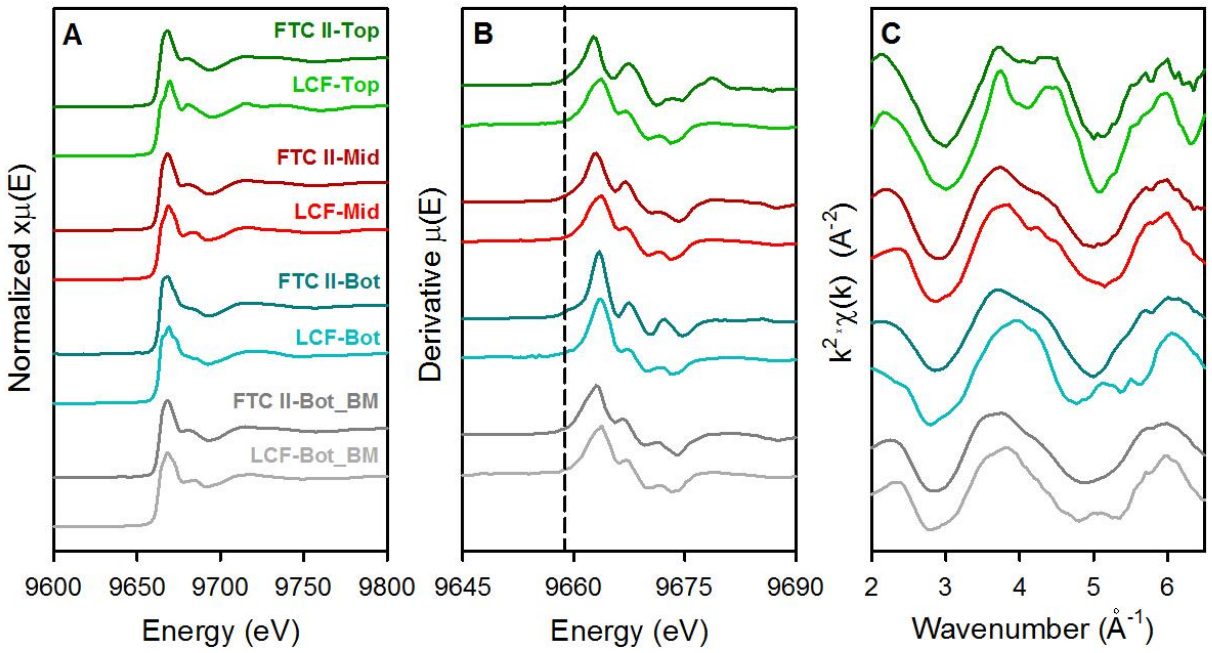

Figure 3.3 Results of linear combination fitting (LCF) analysis developed from combinations of $Zn(OH)_2$, ZnO, and Zn on Fh standard spectra. LCF spectra are plotted below respective FTC II sample spectra for ease of comparison. LCF results are displayed as **(A)** normalized μ(E), **(B)** the first derivative of μ(E), and **(C)** k^2 χ(k), revealing the qualitative accuracy for models of each sample spectra in different XAS spaces.

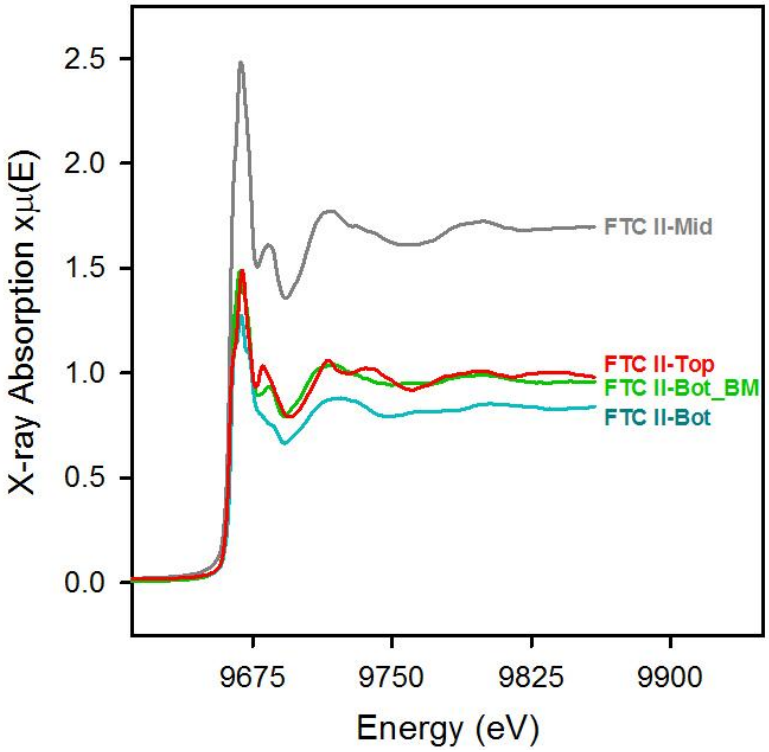

Figure 3.4 X-ray absorption (xμ(E)) plotted versus energy for Zn XANES spectra collected after termination of the FTC II experiment. FTC II-Bot, -Mid, and -Top spectra were collected on the intact FTC II at the Sector 10-ID (insertion device) beamline. The FTC II-Bot_BM spectra was gathered on bulk solids preserved from FTC II after disassembly at a later date for comparison.

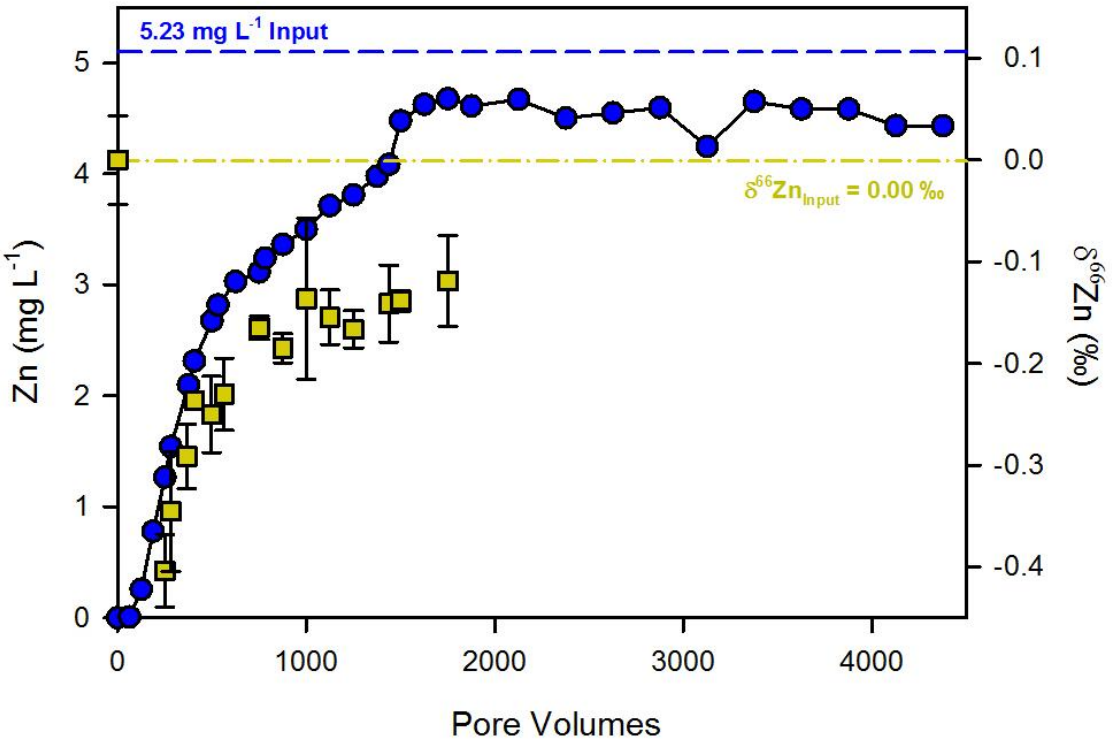

Figure 3.5 Zinc effluent concentrations (blue circles) and δ^{66}Zn values (gold squares) reported for Zn FTC II. The average Zn influent concentrations is marked with a medium dashed blue line and average δ^{66}Zn influent values are indicated by the gold dotted-dashed line. Zinc effluent concentrations are normalized to the input value, therefore the input is at 0.00 ‰, and the difference between δ^{66}Zn sample measurements relative to the input can be interpreted directly from the right y-axis.

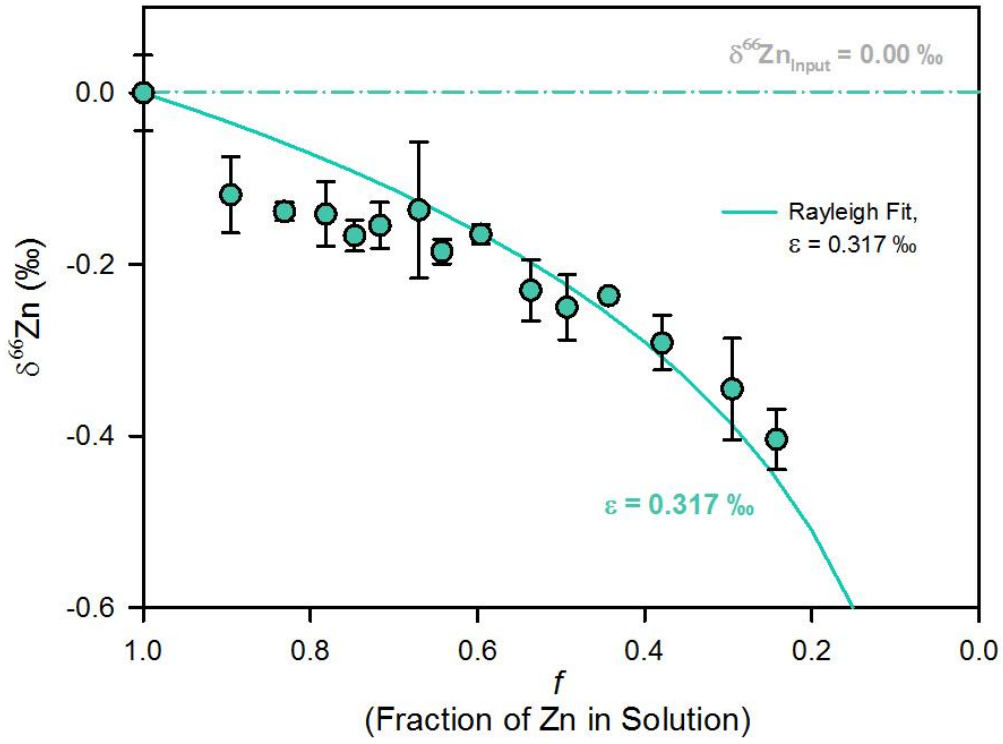

Figure 3.6 Zinc isotope fractionation ($\delta^{66}Zn$) as a function of aqeous Zn (*f*) in effluent samples, with a Rayleigh curve fit to all FTC II data, where ε = 0.32 ‰. Isotope values are reported with 2σ error bars based on three distinct analytical measurements.

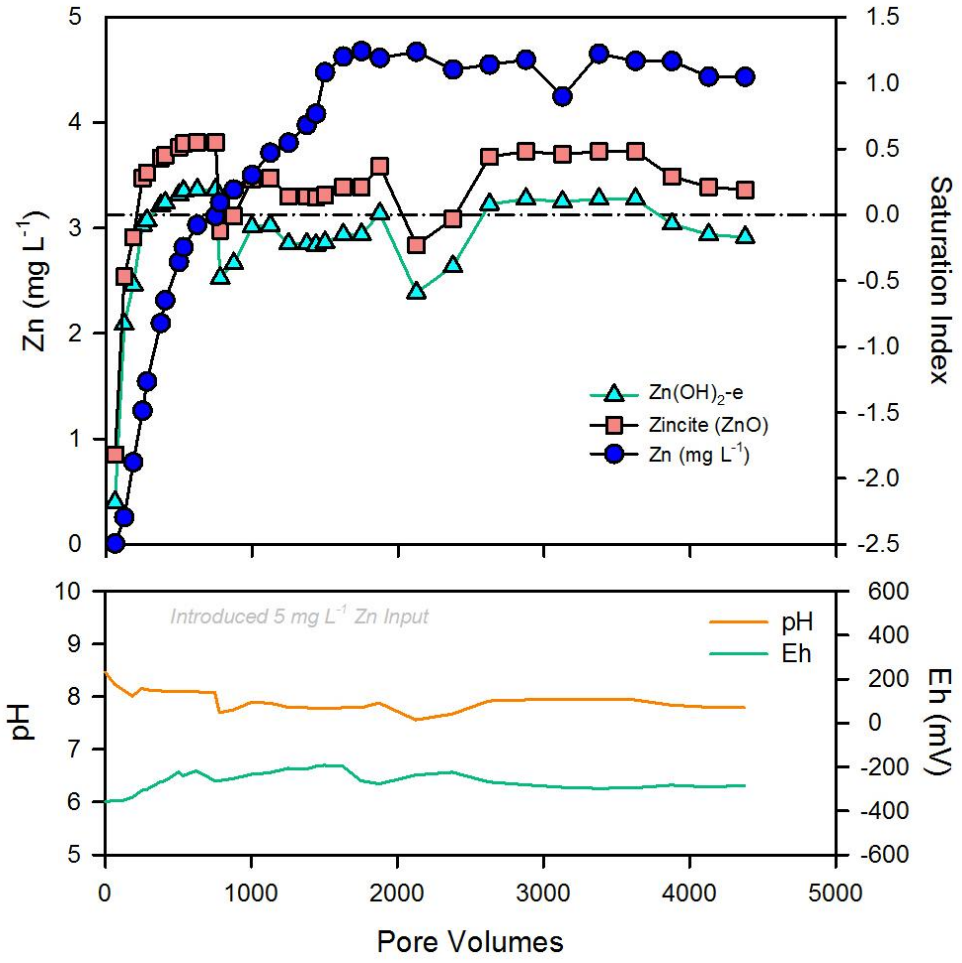

Figure 3.7 Saturation indices for $Zn(OH)_2$ and ZnO computed in PHREEQC Interactive based on pH and pe microelectrode data (bottom) and Zn, Fe, and S concentration data (mg L^{-1}). The dashed line indicates mineral phases are saturated at chemical equilibrium in solution.

Chapter 4: Conclusions

4.1 Summary of Key Findings

Metal isotope fractionation has been used as a valuable tool for tracing metals as they partition between different phases and reservoirs in the environment due to geochemical and biological reactions (Weiss et al., 2008; Bigalke et al., 2010; Blowes et al., 2002). Isotope ratio measurements and associated fractionation factors offer a unique method of characterizing these reactions under specific laboratory and field conditions.

The utility of Cu and Zn in many industrial and commercial products and applications has led to global mining operations worldwide to extract these transition metals. The release of Cu and Zn to the environment from mine tailings and ore refining processes has caused widespread contamination of groundwater and surface water, posing toxic effects to ecosystems and inhabitants in proximity of mining districts. To address the issue of groundwater contamination induced by extraction, processing and industrial uses of metals, PRBs have become a popular remediation strategy for passive *in situ* attenuation of organic and inorganic contaminants, including metals such as Cu and Zn (Naftz et al., 2002). To promote reductive dissolution of redox sensitive elements, as well as adsorption and precipitation pathways, ZVI has been implemented as a highly effective PRB material for facilitating metal immobilization. This investigation aims to enhance the understanding of isotopes as a tool to characterize geochemical processes controlling aqueous concentrations of Cu and Zn in a saturated flow ZVI system.

A series of FTC experiments were performed in an anoxic glovebox, where Cu and Zn breakthrough were measured, along with the associated trends in metal isotopes. In effluent samples on which $\delta^{65}Cu$ measurements were performed, $Cu^{2+}_{(aq)}$ varied from 0.09 to 0.94 mg L^{-1}. The $\delta^{65}Cu$ values reached 1.30 ‰ in the effluent sample at the lowest end of the *f* range, and

decreased towards the input isotope composition (0.27 ‰) as the experiment progressed.

Concentrations of $Zn^{2+}_{(aq)}$ in effluent samples analyzed for $\delta^{66}Zn$ spanned an *f* range of 0.71, and isotope values varied from -0.59 ‰ to -0.19 ‰ for the sample at *f* = 0.24 and the mean $\delta^{66}Zn_{input}$ respectively. The isotope trends for Cu and Zn FTC II experiments proceeded according to Rayleigh-type fractionation. The isotope fractionation factor (ε) for the Cu system was -0.31 ‰ in accordance with the aqueous depletion in ^{65}Cu as $Cu^{2+}_{(aq)}$ breakthrough occurred. The Zn isotope dataset was best fit by a Rayleigh curves where ε = 0.32 ‰.

Characterization of FTC solids using XANES confirmed the presence of Cu^0 at bottom, middle, and top positions in the intact FTC II. Reduced Cu in the form of Cu_2O also contributed in similar abundances as Cu^0 to the LCF analysis of sample spectra at the top and bottom locations. Linear combination fitting of Zn XANES suggested the presence of ZnO and $Zn(OH)_2$ precipitates at the three scanned positions. A standard of Zn sorbed to ferrihydrite also contributed meaningfully to the spectra obtained for the bottom position (influent end) of the intact Zn FTC II. Collectively, these results show that enrichment of the heavy Cu isotope in solution is linked to Cu reduction by ZVI, while aqueous Zn became depleted during adsorption and precipitation of Zn (hydr)oxides during attenuation by ZVI.

4.2 Future Recommendations

This study enhances the knowledge base on isotope fractionation as it relates to metal mobility at contaminated mine sites, specifically in regards to PRB systems for metal-contaminated groundwater. The results of this thesis can be used to better understand the reactions controlling metal concentrations in ZVI remediation systems. The advantage of isotopes that may lead to an improved understanding of metal attenuation processes is the fact that they represent mechanisms in effect on a greater spatial scale than conventional aqueous

geochemical measurements (Blowes et al., 2002). Metal isotopes can also be used to delinate the source metals derived from industrial sites versus natural ore deposits (Bigalke et al., 2010; Borrok et al., 2008), an application which this research may be extended to depending on location. Improvements to monitoring of contaminated groundwater treated at PRB locations may have substantial economic benefits if they can be utilized to improve PRB efficiency and decrease the cost associated with rehabilitating contaminated sites in the future.

This work may be an asset as isotope research is increasingly extended to fieldwork programs. Comparison of the extent of fractionation observed here to the isotope changes in $\delta^{65}Cu$ and $\delta^{66}Zn$ in aqueous field samples (*e.g*. upgradient of a PRB, within the PRB, and in the treated effluent) can assist in the interpretation of geochemical pathways which cause fractionation. Results of this thesis show significant variations in the magnitude and direction of fractionation depending on the metal and reaction pathways involved in remediation. In similar FTC experiments, $Cu^{2+}_{(aq)}$ was enriched in the heavy isotope by over 1 ‰, while $Zn^{2+}_{(aq)}$ was depleted in the heavy isotope by ~0.4 ‰ upon initial uptake by ZVI.

It would be valuable to incorporate more comprehensive solid phase characterization methods in similar studies going forward. Specific methods can include extended x-ray absorption fine structure (EXAFS) analysis of Cu and Zn phases. Multiple XAS techniques at the Fe K-edge, Moss-Bauer analysis, or Raman spectroscopy can be implemented to identify solid phase Fe minerals on the ZVI surfaces. These additional methods would be advantageous for clarifying the Fe (oxy)hydroxide phases present on ZVI which have an important role for adsorption of metal contaminants.

References

Acosta, J., Faz, A., Martinez-Martinez, S., Zornoza, R., Carmona, D. M., & Kabas, S. (2011). Multivariate statistical and GIS-based approach to evaluate heavy metals behavior in mine sites for future reclamation. *J. Geochem. Explor. 109*(1-3), 8–17.

Albarède, F. (2004). The stable isotope geochemistry of copper and zinc. *Rev.Mineral. Geochem. 55*, 409–427.

Aranda, S., Borrok, D. M., Wanty, R. B., & Balistrieri, L. S. (2012). Zinc isotope investigation of surface and pore waters in a mountain watershed impacted by acid rock drainage. *Sci. Tot. Environ. 420*, 202–213.

Aldrich, A. P., Kistler, D., & Sigg, L. (2002). Speciation of Cu and Zn in drainage water from agricultural soils. *Environ. Sci. Technol. 36*(22), 4824–4830.

Asael, D., Matthews, A., Bar-Matthews, M., & Halicz, L. (2007). Copper isotope fractionation in sedimentary copper mineralization (Timna Valley, Israel). *Chem. Geol., 243*, 238–254.

Asael, D., Butler, I., Rickard, A. D., Bar-Matthews, M., & Halicz, L. (2006). $^{65}Cu/^{63}Cu$ fractionation during copper sulphide formation from iron sulphides in aqueous solution. *Geochim. Cosmochim. Acta 70*(18), A23.

Atwood, G. E., & Curtis, C. H. (1974). Hydrometallurgical process for the production of copper. U.S. Patent 3,785,944. 15 Jan. 1974.

Balistrieri, L. S., Borrok, D. M., Wanty, R. B., & Ridley, W. I. (2008). Fractionation of Cu and Zn isotopes during adsorption onto amorphous Fe(III) oxyhydroxide: Experimental mixing of acid rock drainage and ambient river water. *Geochim. Cosmochi. Acta 72*, 311–328.

Benfatto, M., D'Angelo, P., Della Longa, S., & Pavel, N. V. (2002). Evidence of distorted fivefold coordination of the Cu^{2+} aqua ion from an x-ray-absorption spectroscopy quantitative analysis. *Phys. Rev. B 65*, 174205.

Benner, S. G., Blowes, D. W., & Ptacek, C. J. (1997). A full-scale porous reactive wall for prevention of acid mine drainage. *Ground Water Monit. Rem. 17*(4), 99-107.

Berna, E. C., Johnson, T. M., Makdisi, R. S., & Basu, A. (2010). Cr stable isotopes as indicators of Cr(VI) reduction in groundwater: A detailed time-series study of a point-source plume. *Environ. Sci. Technol. 44*(3), 1043–1048.

Bigalke, M., Weyer, S., & Wilcke, W. (2010). Copper isotope fractionation during complexation with insolubilized humic acid. *Environ. Sci. Technol. 44*(3), 5496–5502.

Black, J. R., Kavner, A., & Schauble, E. A. (2011). Calculation of equilibrium stable isotope partition function ratios for aqueous zinc complexes and metallic zinc. *Geochim. Cosmochim. Acta 75*(3), 769–783.

Blowes, D. W., Ptacek, C. J., Jambor, J. L., Weisener, C. G., Paktunc, D., Gould, W. D., & Johnson, D. B. (2013). *The Geochemistry of Acid Mine Drainage*. *Treatise on Geochemistry: Second Edition, 9,* 149-204.

Blowes, D. (2002). Environmental chemistry. Tracking hexavalent Cr in groundwater. *Science, 295*(5562), 2024–2025.

Blowes, D. W., Ptacek, C. J., Benner, S. G., McRae, C. W. T., Bennett, T. A., & Puls, R. W. (2000). Treatment of inorganic contaminants using permeable reactive barriers. *J. Contam. Hydrol. 45*, 123–137.

Blowes, D. W., Ptacek, C. J., & Jambor, J. L. (1997). *In situ* remediation of Cr(VI)-contaminated groundwater using permeable reactive walls: Laboratory studies. *Environ. Sci. Technol. 31*(12), 3348–3357.

Blowes, D. W. and Ptacek, C. J. (1994). "System for treating contaminated groundwater." U.S. Patent 5,362,394. 8 Nov. 1994.

Borrok, D. M., Nimick, D. A., Wanty, R. B., & Ridley, W. I. (2008). Isotopic variations of dissolved copper and zinc in stream waters affected by historical mining. *Geochim. Cosmochim. Acta 72*, 329–344.

Borrok, D. M., Wanty, R. B., Ridley, W. I., Lamothe, P. J., Kimball, B. A., Verplanck, P. L., & Runkel, R. L. (2009). Application of iron and zinc isotopes to track the sources and mechanisms of metal loading in a mountain watershed. *Appl. Geochem. 24*(7), 1270–1277.

Bullen, T. D. (2014). *Natural Weathering Rates of Silicate Minerals*. *Treatise on Geochemistry 2*(7). Elsevier Ltd.

Cantrell, K. J., Kaplan, D. I., & Wietsma, T. W. (1995). Zero-valent iron for the in situ remediation of selected metals in groundwater. *J. Hazard. Mater. 42*, 201–212.

Chaboy, J., Muñoz-Páez, A., Merkling, P. J., & Marcos, E. S. (2006). The hydration of Cu2+: Can the Jahn-Teller effect be detected in liquid solution? *J. Chem. Phys. 124*(6).

Chen, J., Gaillardet, J., & Louvat, P., 2008. Zinc isotopes in the Seine River waters, France: A probe of anthropogenic contamination. *Environ. Sci. Technol. 42*(17), 6494–6501.

Cloquet, C., Carignan, J., Lehmann, M. F., & Vanhaecke, F. (2008). Variation in the isotopic composition of zinc in the natural environment and the use of zinc isotopes in biogeosciences: a review. *Anal. Bioanal. Chem. 390*(2), 451–463.

Coplen, T. B. (2011). Guidelines and recommended terms for expression of stable-isotope-ratio and gas-ratio measurement results. *Rapid Communications in Mass Spectrometry: RCM*, *25*, 2538–2560.

Coutaud, A., Meheut, M., Viers, J., Rols, J. L., & Pokrovsky, O. S. (2014). Zn isotope fractionation during interaction with phototrophic biofilm. *Chem. Geol. 390*, 46–60.

Ehrlich, S., Butler, I., Halicz, L., Rickard, D., Oldroyd, a., & Matthews, A. (2004). Experimental study of the copper isotope fractionation between aqueous Cu(II) and covellite, CuS. *Chem. Geol. 209*, 259–269.

Ellis, A. S., Johnson, T. M., & Bullen, T. D. (2002). Chromium isotopes and the fate of hexavalent chromium in the environment. *Science, 295*, 2060–2062.

Farrell, J., Wang, J., O'Day, P., & Conklin, M. (2001). Electrochemical and spectroscopic study of arsenate removal from water using zero-valent iron media. *Environ. Sci. Technol. 35*(10), 2026–2032.

Forghani, G., Mokhtari, A. R., Kazemi, G. A., & Davoodi Fard, M. (2015). Total concentration, speciation and mobility of potentially toxic elements in soils around a mining area in central Iran. *Chemie Der Erde – Geochem*, 1–12.

Fu, F., Dionysiou, D. D., & Liu, H. (2014). The use of zero-valent iron for groundwater remediation and wastewater treatment: A review. *J. Hazard. Mater. 267*, 194–205.

Fujii, T., Moynier, F., Abe, M., Nemoto, K., & Albarède, F. (2013). Copper isotope fractionation between aqueous compounds relevant to low temperature geochemistry and biology. *Geochim. Cosmochim. Acta*, *110*, 29–44.

Fujii, T., Moynier, F., Pons, M. L., & Albarède, F. (2011). The origin of Zn isotope fractionation in sulfides. *Geochim. Cosmochim. Acta*, *75*(23), 7632–7643.

Fulton, J. L., Hoffmann, M. M., Darab, J. G., Palmer, B. J., & Stern, E. A. (2000). Copper(I) and Copper(II) Coordination Structure under Hydrothermal Conditions at 325 °C: An X-ray Absorption Fine Structure and Molecular Dynamics Study. *J. Phys. Chem. A, 104*(49), 11651–11663.

Furukawa, Y., Kim, J. W., Watkins, J., & Wilkin, R. T. (2002). Formation of Ferrihydrite and Associated Iron Corrosion Products in Permeable Reactive Barriers of Zero Valent Iron. *Environ. Sci. Technol. 36/24*(24), 5469-5475.

Gerlach, R. W. and Nocerino, J. M. (2003). Guidance for Obtaining Representative Laboratory Analytical Subsamples from Particulate Laboratory Samples. U.S. EPA, 600/R-03/027

Gillham, R. W. (1996). "System for cleaning contaminated soil." U.S. Patent 5,534,154. 9 July 1996.

Gui, L., Yang, Y., Jeen, S., Gillham, R. W., & Blowes, D. W. (2009). Reduction of chromate by granular iron in the presence of dissolved $CaCO_3$. *Appl. Geochem. 24*(4), 677–686.

Guo, Q., & Blowes, D. W. (2009). Biogeochemistry of two types of permeable reactive barriers, organic carbon and iron-bearing organic carbon for mine drainage treatment: Column experiments. *J. Contam. Hydrol. 107*(3-4), 128–139.

Hashim, M. A., Mukhopadhyay, S., Sahu, J. N., & Sengupta, B. (2011). Remediation technologies for heavy metal contaminated groundwater. *J. Environ. Manage. 92*(10), 2355–2388.

Herbert, R. B. (2003). Zinc immobilization by zerovalent Fe: surface chemistry and mineralogy of reaction products. *Mineral. Magazine, 67*, 1285–1298.

Hoefs, J. (2009). Isotope Fractionation Processes of Selected Elements. *Stable Isotope Geochemistry*, 35–92.

Jamieson-Hanes, J. H., Shrimpton, H. K., Veeramani, H., Ptacek, C. J., Lanzirotti, A., Newville, M., & Blowes, D. W. (2017). Evaluating zinc isotope fractionation under sulfate reducing conditions using a flow-through cell and in situ XAS analysis. *Geochim. Cosmochim. Acta*, *203*, 1–14.

Jamieson-Hanes, J. H., Lentz, A. M., Amos, R. T., Ptacek, C. J., & Blowes, D. W. (2014). Examination of Cr(VI) treatment by zero-valent iron using in situ, real-time X-ray absorption spectroscopy and Cr isotope measurements. *Geochim. Cosmochim. Acta*, *142*, 299–313.

Jamieson-Hanes, J. H., Gibson, B. D., Lindsay, M. B. J., Kim, Y., Ptacek, C. J., & Blowes, D. W. (2012). Chromium isotope fractionation during reduction of Cr(VI) under saturated flow conditions. *Environ. Sci. Technol. 46*, 6783–6789.

Jeen, S. W., Jambor, J. L., Blowes, D. W., & Gillhamt, R. W. (2007). Precipitates on granular iron in solutions containing calcium carbonate with trichloroethene and hexavalent chromium. *Environ. Sci. Technol. 41*, 1989–1994.

Johnson, C. M., Beard, B. L., & Albarede, F. (2004). Overview and General Concepts. *Rev. Mineral. Geochem. 55*(1), 1–24.

Juillot, F., Maréchal, C., Ponthieu, M., Cacaly, S., Morin, G., Benedetti, M., Guyot, F. (2008). Zn isotopic fractionation caused by sorption on goethite and 2-Lines ferrihydrite. *Geochem. Cosmochim. Acta, 72*, 4886–4900.

Kimball, B. E., Mathur, R., Dohnalkova, a. C., Wall, a. J., Runkel, R. L., & Brantley, S. L. (2009). Copper isotope fractionation in acid mine drainage. *Geochim. Cosmochim. Acta*, *73*(5), 1247–1263.

Kitchen, J. W., Johnson, T. M., Bullen, T. D., Zhu, J., & Raddatz, A. (2012). Chromium isotope fractionation factors for reduction of Cr(VI) by aqueous Fe(II) and organic molecules. *Geochim. Cosmochim. Acta*, *89*, 190–201.

Korzhavyi, P. A, & Johansson, B. (2011). Literature review on the properties of cuprous oxide Cu_2O and the process of copper oxidation. *Swedish Nuclear Fuel and Waste Management Co, Technical*, SKB TR-11-08

Ku, Y., & Chen, C. H. (1992). Kinetic Study of Copper Deposition on Iron by Cementation Reaction. *Separation Sci. Technol. 27*(10), 1259–1275.

Larson, P. B., Maher, K., Ramos, F. C., Chang, Z., Gaspar, M., & Meinert, L. D. (2003). Copper isotope ratios in magmatic and hydrothermal ore-forming environments. *Chem. Geol. 201*(3-4), 337–350.

Li, X., & Zhang, W. (2007). Sequestration of metal cations with zerovalent iron nanoparticles - A study with high resolution X-ray photoelectron spectroscopy (HR-XPS), *J. Phys. Chem. C 111*, 6939–6946.

Light, T. S. (1972). Standard solution for redox potential measurements. *Anal. Chem.*, 44 (6), 1038−1039.

Lindsay, M. B. J., Ptacek, C. J., Blowes, D. W., & Gould, W. D. (2008). Zero-valent iron and organic carbon mixtures for remediation of acid mine drainage: Batch experiments. *Appl. Geochem. 23*, 2214–2225.

Little, S. H., Sherman, D. M., Vance, D., & Hein, J. R. (2014). Molecular controls on Cu and Zn isotopic fractionation in Fe-Mn crusts. *Earth Planet. Sci. Let. 396*, 213–222.

Ludwig, R. D., McGregor, R. G., Blowes, D. W., Benner, S. G., & Mountjoy, K. (2002). A permeable reactive barrier for treatment of heavy metals. *Ground Water*.

Mackay, D.M. and Cherry, J.A. (1989). Groundwater contamination: pump-and-treat remediation. *Environ. Sci. Technol., 23*(6), pp. 630-636

Maréchal, C. N., Télouk, P., & Albarède, F. (1999). Precise analysis of copper and zinc isotopic compositions by plasma-source mass spectrometry. *Chem. Geol. 156*, 251–273.

Maréchal, C., & Albarède, F. (2002). Ion-exchange fractionation of copper and zinc isotopes. *Geochim. Cosmochim. Acta*, *66*(9), 1499–1509.

Markl, G., Lahaye, Y., & Schwinn, G. (2006). Copper isotopes as monitors of redox processes in hydrothermal mineralization. *Geochim. Cosmochim. Acta*, *70*, 4215–4228.

Mathur, R., Munk, L. A., Townley, B., Gou, K. Y., Gómez Miguélez, N., Titley, S., Ruiz, J. (2014). Tracing low-temperature aqueous metal migration in mineralized watersheds with Cu isotope fractionation. *Appl. Geochem. 51*, 109–115.

Mathur, R., Jin, L., Prush, V., Paul, J., Ebersole, C., Fornadel, A., Brantley, S. (2012). Cu isotopes and concentrations during weathering of black shale of the Marcellus Formation, Huntingdon County, Pennsylvania (USA). *Chem. Geol. 304-305*, 175–184.

Matthies, R., Krahé, L., & Blowes, D. W. (2014). Zinc stable isotope fractionation upon accelerated oxidative weathering of sulfidic mine waste. *Sci. Tot. Environ. 487*(1), 97–101.

Moeller, K., Schoenberg, R., & Weiss, D. (2012). Calibration of the New Certified Reference Materials ERM-AE633 and ERM-AE647 for Copper and IRMM-3702 for Zinc Isotope Amount Ratio Determinations. *Geostand.Geoanal. Res. 36*, 177–199.

Moncur, M. C., Ptacek, C. J., Blowes, D. W., Jambor, J. L. (2005). Release, transport and attenuation of metals from an old tailings impoundment. *Appl. Geochem*. *10*, 639–659.

Morrison, S. J., Metzler, D. R., & Dwyer, B. P. (2002). Removal of As, Mn, Mo, Se, U, V and Zn from groundwater by zero-valent iron in a passive treatment cell: Reaction progress modeling. *J. Contam. Hydrol. 56*, 99–116.

Musinu, A, Paschina, G., Piccaluga, G., & Magini, M. (1983). Coordination of copper (II) in aqueous $CuSO_4$ solution. *Inorg. Chem. 22*, 1184–1187.

Naftz, D. L., Morrison, S. J., Davis, J A., and Fuller, C. C. (2002). *Handbook of groundwater remediation using permeable reactive barriers: Applications to radionuclides, trace metals, and nutrients.* San Diego, CA: Associated Press.

Natural Resources Canada (2015). Production of Canada's Leading Metals. Retrieved Dec 2015 from <http://sead.nrcan.gc.ca/prod-prod/mon-men-eng.aspx>.

Newville, M. (2004). Fundamentals of XAFS. *Consortium for Advanced Radiation Sciences,* 43.

Nordstrom, D. K. (1977). Thermochemical redox equilibria of ZoBell's solution. *Geochim. Cosmochim. Acta*, 41 (12), 1835−1841.

O'Day, P. A, Carroll, S. A, & Waychunas, G. A. (1998). Rock-water interactions controlling zinc, cadmium, and lead concentrations in surface waters and sediments, U.S. Tri-State Mining District. 1. Molecular identification using X-ray absorption spectroscopy. *Environ. Sci. Technol. 32*(7), 943–955.

Odziemkowski, M. S., Schuhmacher, T. T., Gillham, R. W., & Reardon, E. J. (1998). Mechanism of oxide film formation on iron in simulating groundwater solutions: Raman spectroscopic studies. *Corrosion Science, 40*(2-3), 371–389.

Oswald, H. R. & Asper, R. (1977). Physics and Chemistry of Materials with Layered Structures: *Preparation and Crystal Growth of Materials with Layered Structures* (Vol. 1, pp. 122-128). Dordrecht, NL: D. Reidel Publishing Co.

Parkhurst, D. L., Appelo, C. A. J. (1999). User's guide to PHREEQC (Version 2): A Computer Program for Speciation, Batch-Reaction, One-Dimensional Transport, and Inverse Geochemical Calculations. U.S. Geological Survey: Denver, Colorado.

Pasquarello, A., Petri, I., Salmon, P. S., Parisel, O., Car, R., Toth, E., Powell, D. H., Fischer, H. E., Helm, L., Merbach, A. E., 2001. First solvation shell of the Cu(II) aqua ion: Evidence for fivefold coordination. *Science*, *291*(5505), 856–859.

Pokrovsky, O. S., Viers, J., Emnova, E. E., Kompantseva, E. I., & Freydier, R. (2008). Copper isotope fractionation during its interaction with soil and aquatic microorganisms and metal oxy(hydr)oxides: Possible structural control. *Geochim. Cosmochim. Acta 72*, 1742–1757.

Powell, R. M., Blowes, D. W., Gillham, R. W., Schultz, D., Sivaves, T., Puls, R. W., Landis, R. (1998). Permeable Reactive Barrier Technologies for Contaminant Remediation. *U.S. EPA* 600/R-98/125.

Pugh, R. E., Dick, D. G., & Fredeen, A. L. (2002). Heavy metal (Pb, Zn, Cd, Fe, and Cu) contents of plant foliage near the Anvil Range lead/zinc mine, Faro, Yukon Territory. *Ecotox. Environ. Safety 52*, 273–279.

Puls, R. W., Blowes, D. W., & Gillham, R. W. (1999). Long-term performance monitoring for a permeable reactive barrier at the U.S. Coast Guard Support Center, Elizabeth City, North Carolina. *J. Hazard. Mater. 68*, 109–124.

Rangsivek, R. (2010). Removal of dissolved metals from storm water runoff by zero-valent iron. Diss. der Technischen Universität Berlin.

Rangsivek, R., & Jekel, M. R. (2005). Removal of dissolved metals by zero-valent iron (ZVI): Kinetics, equilibria, processes and implications for stormwater runoff treatment. *Water Res. 39*, 4153–4163.

Ravel, B., Newville, M. (2005). ATHENA, ARTEMIS, HEPHAESTUS: Data analysis for Xray absorption spectroscopy using IFEFFIT. *J. Synchrotron Radiat.* 12(4), 537-541.

Roberts, D. R., Ford, R. G., & Sparks, D. L. (2003). Kinetics and mechanisms of Zn complexation on metal oxides using EXAFS spectroscopy. *J. Colloid Interface Sci. 263*(2), 364–376.

Reardon, E. J. (2005). Zerovalent irons: Styles of corrosion and inorganic control on hydrogen pressure buildup. *Environ. Sci. Technol. 39*(18), 7311–7317.

Ritter, K., Odziemkowski, M. S., & Gillham, R. W. (2002). An *in situ* study of the role of surface films on granular iron in the permeable iron wall technology. *J. Contam. Hydrol. 55*(1-2), 87–111.

Schauble, E. (2004). Applying stable isotope fractionation theory to new systems. *Rev. Mineral. Geochem. 55*(1), 65.

Sherman, D. M. (2013). Equilibrium isotopic fractionation of copper during oxidation/reduction, aqueous complexation and ore-forming processes: Predictions from hybrid density functional theory. *Geochim. Cosmochim. Acta*, *118*, 85–97.

Shiel, A. E., Weiss, D., & Orians, K. J. (2010). Evaluation of zinc, cadmium and lead isotope fractionation during smelting and refining. *Sci. Tot. Environ. 408*(11), 2357–2368.

Shokes, T. E., & Möller, G. (1999). Removal of disslolved heavy metals from acid rock drainage using iron metal. *Environ. Sci. Technol. 33*(2), 282–287.

Sidenko, N. V., & Sherriff, B. L. (2005). The attenuation of Ni, Zn and Cu, by secondary Fe phases of different crystallinity from surface and ground water of two sulfide mine tailings in Manitoba, Canada. *Appl. Geochem*. *20*, 1180–1194.

Sigg, L. (2014). Metals as water quality parameters – Role of speciation and bioavailability. *Comp. Water Qual. Purif. 4*,315-328.

Straumanis, M. E., & Yu, L. S. (1969). Lattice parameters, densities, expansion coefficients and perfection of structure of Cu and of Cu–In α phase. *Acta Crystall. Sec. A 25*, 676–682.

Trivedi, P., Axe, L., & Tyson, T. (2001). An analysis of zinc sorption to amorphous versus crystalline iron oxides using XAS. *J. Colloid Interface Sci. 244*(2), 230–238.

Veeramani, H., Eagling, J., Jamieson-Hanes, J. H., Kong, L., Ptacek, C. J., & Blowes, D. W. (2015). Zinc isotope fractionation as an indicator of geochemical attenuation processes. *Environ. Sci. Technol. Lett. 2*(11), 314-319.

Waychunas, G. A., Fuller, C. C., Davis, J. A., & Rehr, J. J. (2002). Surface complexation and precipitate geometry for aqueous Zn(II) sorption on ferrihydrite: II. XANES analysis and simulation. *Geochim. Cosmochim. Acta*, *67*(5), 1031–1043.

Weiss, D. J., Rehkdmper, M., Schoenberg, R., McLaughlin, M., Kirby, J., Campbell, P. G., Arnold, T., Peel, K., & Gioia, A. S. (2008). Application of nontraditional stable-isotope systems to the study of sources and fate of metals in the environment. 665-664.

Wiederhold, J. G. (2015). Metal stable isotope signatures as tracers in environmental geochemistry. *Environ. Sci. Technol. 43,* 2606-2624

Wilkin, R. T., & McNeil, M. S. (2003). Laboratory evaluation of zero-valent iron to treat water impacted by acid mine drainage. *Chemosphere*, *53*, 715–725.

Zhu, X. K., Guo, Y., Williams, R. J. P., O'Nions, R. K., Matthews, A., Belshaw, N. S., Salvato, B. (2002). Mass fractionation processes of transition metal isotopes. *J. Earth Planet. Sci. Let.*, *200*, 47–62.

Appendix A

Chapter 2 Supplementary Information

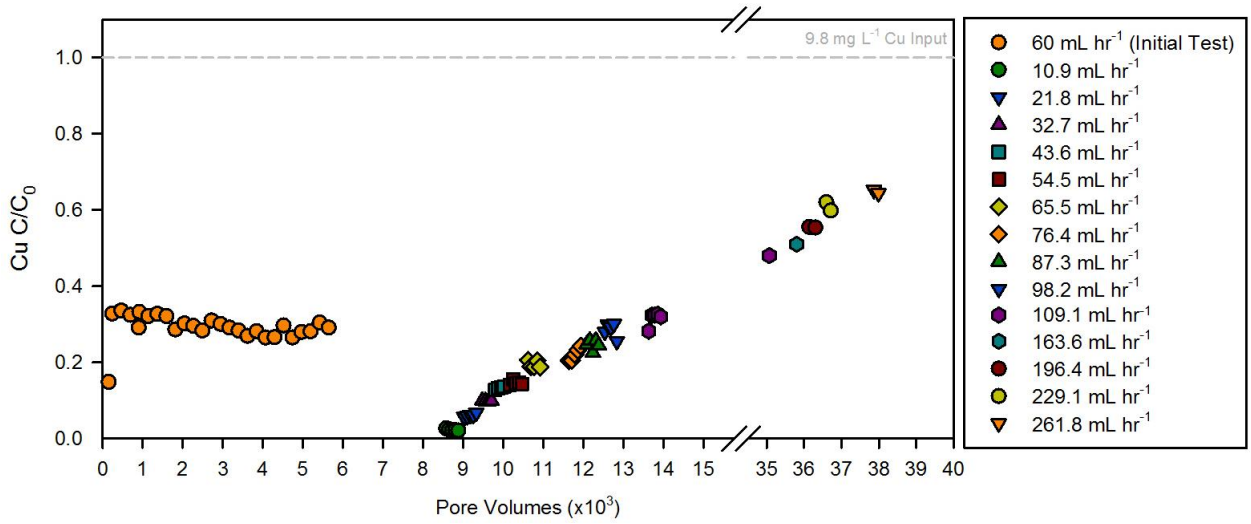

Figure S2.1 Cu FTC I breakthrough curve with flow rate transitions marked by changes in data point symbols. The maximum C/C_0 reached in this trial was 0.65.

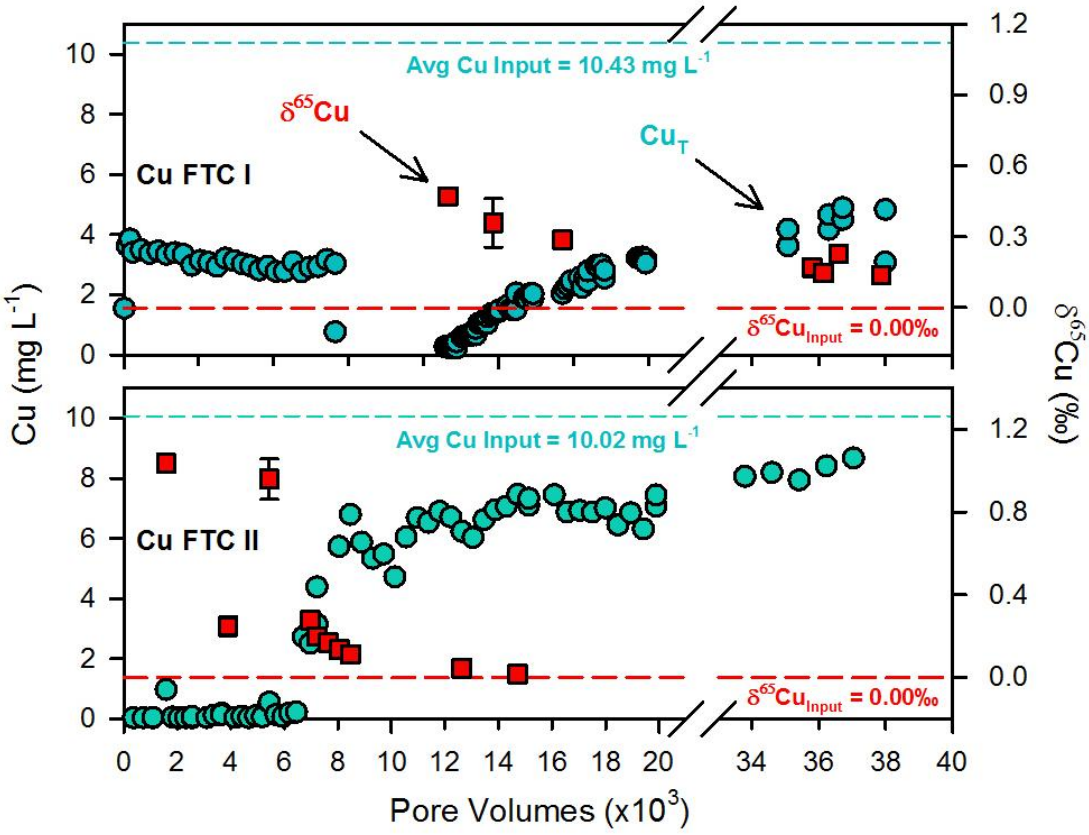

Figure S2.2 Cu concentrations (mg L^{-1}) and Cu isotope fractionation ($\delta^{65}Cu$ normalized to input values; $\delta^{65}Cu_{input}$ = 0.00 ‰) as they change with PVs in Cu FTC I and II stepped flow rate experiments for which isotope data was collected on FTC effluent samples. Horizontal dashed lines indicate the Cu concentration and $\delta^{65}Cu$ isotope values for input solutions.

Appendix B

Chapter 3 Supplementary Information

Table S3.1 Attenuation and breakthrough of Zn and Fe throughout the FTC II experiment

Flow Rate ($mL\ hr^{-1}$)	**Cumulative Pore Volumes**	**Zn in Influent** ($mg\ L^{-1}$)	**Zn Mass in Input** (mol)	**Zn in Effluent** (mol)	**Rate of Zn Removal** ($mol\ hr^{-1}$)	**Zn Retained in FTC*** (mol)	**Fe in Effluent** (mol)
21.8	63	5.223	7.19×10^{-6}	7.18×10^{-6}	1.74×10^{-6}	1.05×10^{-8}	7.17×10^{-6}
21.8	125	5.223	7.19×10^{-6}	6.84×10^{-6}	1.66×10^{-6}	$3.52E\times10^{-7}$	7.23×10^{-6}
21.8	188	5.223	7.19×10^{-6}	6.12×10^{-6}	1.48×10^{-6}	1.07×10^{-6}	6.58×10^{-6}
21.8	250	5.223	7.19×10^{-6}	5.45×10^{-6}	1.32×10^{-6}	1.74×10^{-6}	5.84×10^{-6}
21.8	281	5.223	3.60×10^{-6}	2.53×10^{-6}	1.23×10^{-6}	1.06×10^{-6}	2.69×10^{-6}
21.8	375	5.223	1.08×10^{-5}	6.45×10^{-6}	1.04×10^{-6}	4.33×10^{-6}	6.88×10^{-6}
21.8	406	5.223	3.60×10^{-6}	2.00×10^{-6}	9.70×10^{-7}	1.59×10^{-6}	2.15×10^{-6}
21.8	500	5.223	1.08×10^{-5}	5.26×10^{-6}	8.49×10^{-7}	5.53×10^{-6}	5.85×10^{-6}
21.8	531	5.223	3.60×10^{-6}	1.66×10^{-6}	8.02×10^{-7}	1.94×10^{-6}	1.82×10^{-6}
21.8	625	5.223	1.08×10^{-5}	4.53×10^{-6}	7.32×10^{-7}	6.26×10^{-6}	4.81×10^{-6}
21.8	750	5.223	1.44×10^{-5}	5.81×10^{-6}	7.04×10^{-7}	8.57×10^{-6}	6.35×10^{-6}
21.8	782	5.223	3.60×10^{-6}	1.36×10^{-6}	6.61×10^{-7}	2.23×10^{-6}	1.50×10^{-6}
21.8	875	5.223	1.08×10^{-5}	3.84×10^{-6}	6.20×10^{-7}	6.95×10^{-6}	4.11×10^{-6}
21.8	1000	5.223	1.44×10^{-5}	4.75×10^{-6}	5.75×10^{-7}	9.64×10^{-6}	4.93×10^{-6}
21.8	1125	5.223	1.44×10^{-5}	4.16×10^{-6}	5.04×10^{-7}	1.02×10^{-5}	4.54×10^{-6}
21.8	1250	5.223	1.44×10^{-5}	3.90×10^{-6}	4.72×10^{-7}	1.05×10^{-5}	4.11×10^{-6}
21.8	1375	5.223	1.44×10^{-5}	3.43×10^{-6}	4.15×10^{-7}	1.10×10^{-5}	3.81×10^{-6}
21.8	1438	5.223	7.19×10^{-6}	1.57×10^{-6}	3.80×10^{-7}	5.62×10^{-6}	1.95×10^{-6}
21.8	1500	5.223	7.19×10^{-6}	1.03×10^{-6}	2.49×10^{-7}	6.16×10^{-6}	2.00×10^{-6}
21.8	1626	5.223	1.44×10^{-5}	1.64×10^{-6}	1.99×10^{-7}	1.27×10^{-5}	3.84×10^{-6}
21.8	1751	5.223	1.44×10^{-5}	1.50×10^{-6}	1.82×10^{-7}	1.29×10^{-5}	3.74×10^{-6}
21.8	1876	4.926	1.36×10^{-5}	8.65×10^{-7}	1.05×10^{-7}	1.27×10^{-5}	3.68×10^{-6}
21.8	2126	4.926	2.71×10^{-5}	1.40×10^{-6}	8.51×10^{-8}	2.57×10^{-5}	7.45×10^{-6}
21.8	2376	4.926	2.71×10^{-5}	2.33×10^{-6}	1.41E-07	2.48×10^{-5}	6.69×10^{-6}
21.8	2626	4.926	2.71×10^{-5}	2.08×10^{-6}	1.26×10^{-7}	2.51×10^{-5}	7.00×10^{-6}
21.8	2876	4.926	2.71×10^{-5}	1.82×10^{-6}	1.10×10^{-7}	2.53×10^{-5}	6.08×10^{-6}
21.8	3126	4.926	2.71×10^{-5}	3.74×10^{-6}	2.26×10^{-7}	2.34×10^{-5}	5.83×10^{-6}
21.8	3376	4.926	2.71×10^{-5}	1.51×10^{-6}	9.14×10^{-8}	2.56×10^{-5}	6.72×10^{-6}
21.8	3626	4.926	2.71×10^{-5}	1.88×10^{-6}	1.14×10^{-7}	2.52×10^{-5}	6.64×10^{-6}
21.8	3876	4.926	2.71×10^{-5}	1.89×10^{-6}	1.14×10^{-7}	2.52×10^{-5}	6.56×10^{-6}
21.8	4126	4.926	2.71×10^{-5}	2.70×10^{-6}	1.64×10^{-7}	2.44×10^{-5}	6.31×10^{-6}
21.8	4376	4.926	2.71×10^{-5}	2.72×10^{-6}	1.64×10^{-7}	2.44×10^{-5}	6.28×10^{-6}
21.8	4542	4.926	2.71×10^{-5}	-	-	-	-
TOTAL	**4542**	**-**	**4.86×10^{-4}**	**1.04×10^{-4}**	**-**	**3.82×10^{-4}**	**1.61×10^{-4}**

* Zn retained in solid phase is calculated based on difference between masses of Zn in the influent and effluent

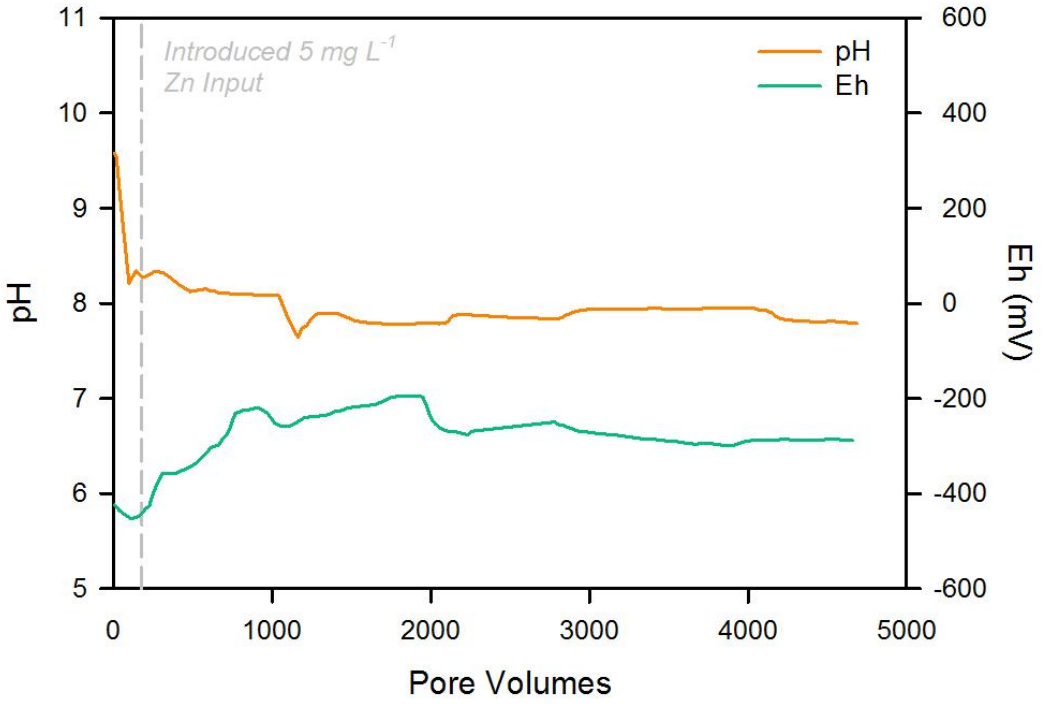

Fig. S3.1. Microelectrode pH and Eh data recorded for the end of the ZVI conditioning period (~300 PVs) and throughout the total Zn FTC II experiment. The FTC effluent pH drops about 1.5 pH units immediately prior to the addition of Zn, while the Eh steadily rises ~150 mV after introduction of the Zn input. After 1000 PVs following the addition of Zn to the system, pH and Eh are relatively stable.

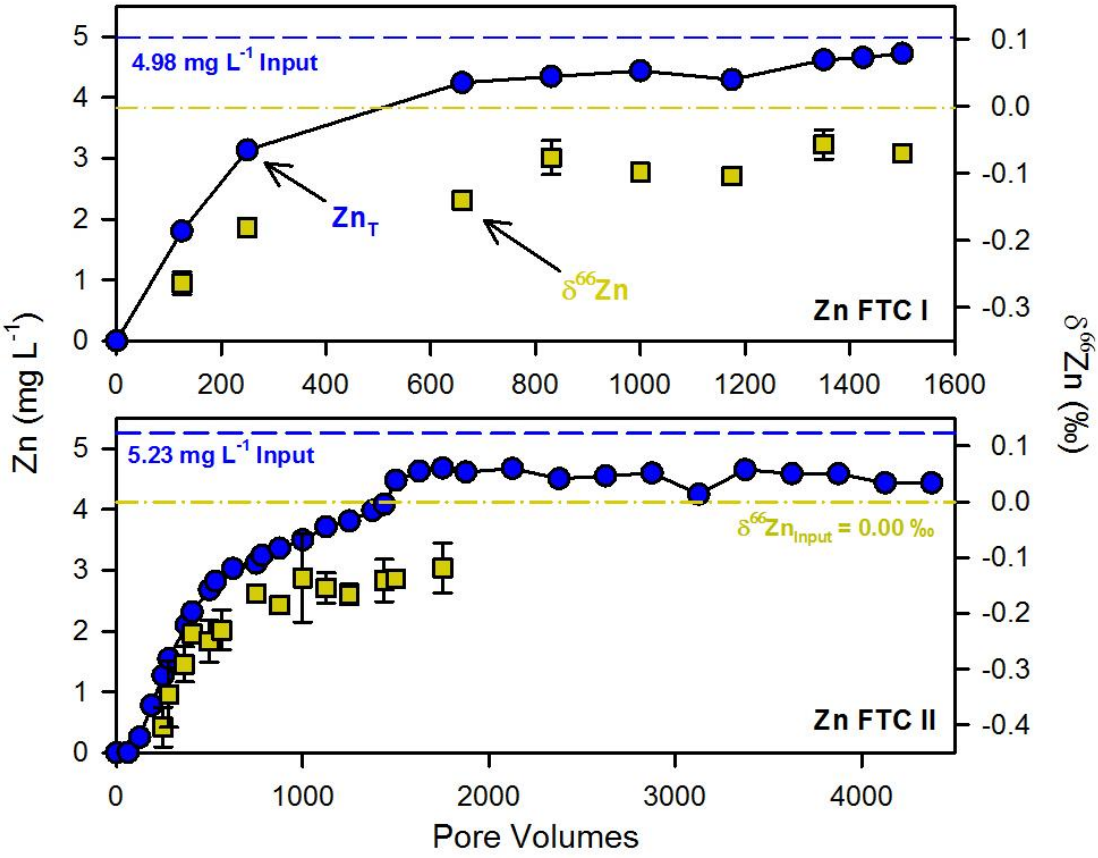

Figure S3.2 Zinc effluent concentrations (blue circles) and δ^{66}Zn values (gold squares) reported for Zn FTC experiments I and II. Average Zn influent concentrations are marked with medium dashed blue lines and average δ^{66}Zn influent values are indicated by gold dotted-dashed lines for each experiment.

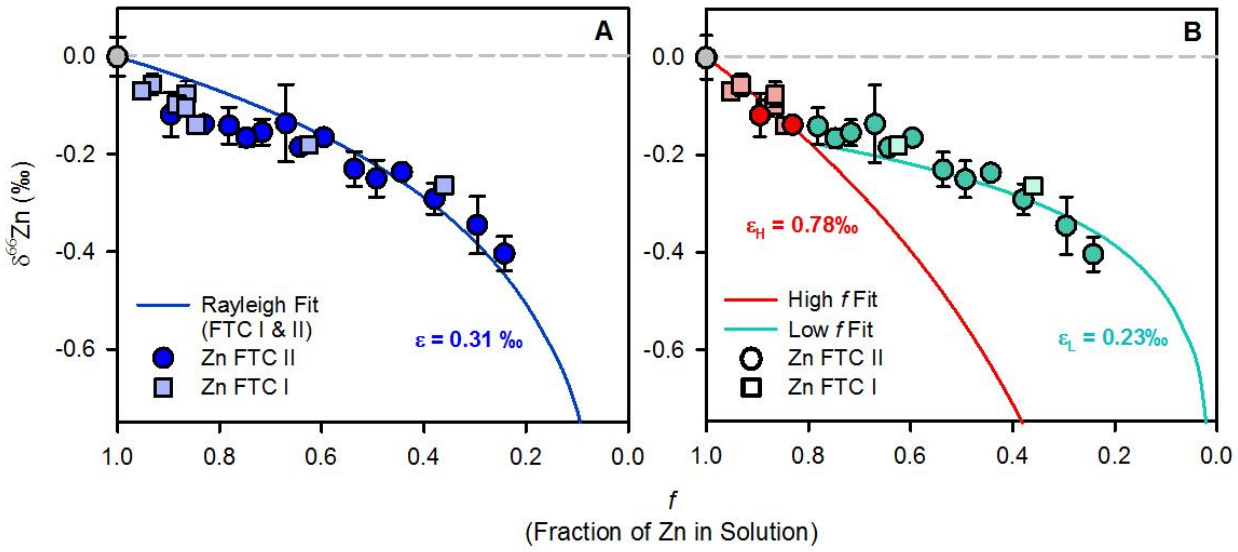

Figure S3.3 (A) Zinc isotope fractionation (δ^{66}Zn) as a function of aqueous Zn (f) in effluent samples, with a Rayleigh curve plotted for all data, and (**B**) for high *f* and low *f* data points normalized to the input δ^{66}Zn value. Square symbols in (**B**) indicate samples from Zn FTC I, and circles mark Zn FTC II samples. The low *f* region refers to samples of $f \leq 0.78$. Isotope data points are recorded with 2σ error bars based on three distinct analytical measurements. Fractionation values are reported in ε notation for each modelled Rayleigh curve.